AERO-STRUCTURAL DESIGN AND ANALYSIS OF AN UNMANNED AERIAL VEHICLE AND ITS MISSION ADAPTIVE WING

A THESIS SUBMITTED TO
THE GRADUATE SCHOOL OF NATURAL AND APPLIED SCIENCES
OF
MIDDLE EAST TECHNICAL UNIVERSITY

BY

ERDOĞAN TOLGA İNSUYU

IN PARTIAL FULFILLMENT OF THE REQUIREMENTS
FOR
THE DEGREE OF MASTER OF SCIENCE
IN
AEROSPACE ENGINEERING

FEBRUARY 2010

Approval of the thesis:

AERO-STRUCTURAL DESIGN AND ANALYSIS OF AN UNMANNED AERIAL VEHICLE AND ITS MISSION ADAPTIVE WING

submitted by **ERDOĞAN TOLGA İNSUYU** in partial fulfillment of the requirements for the degree of **Master of Science in Aerospace Engineering Department, Middle East Technical University** by,

Prof. Dr. Canan Özgen _____
Dean, Graduate School of **Natural and Applied Sciences**

Prof. Dr. Ozan Tekinalp _____
Head of Department, **Aerospace Engineering**

Assist. Prof. Dr. Melin Şahin _____
Supervisor, **Aerospace Engineering Dept., METU**

Examining Committee Members:

Prof. Dr. Yavuz Yaman _____
Aerospace Engineering Dept., METU

Assist Prof. Dr. Melin Şahin _____
Aerospace Engineering Dept., METU

Prof. Dr. Serkan Özgen _____
Aerospace Engineering Dept., METU

Assist. Prof. Dr. Ender Ciğeroğlu _____
Mechanical Engineering Dept., METU

Özcan Ertem, M.Sc. _____
Executive Vice President, TAI

Date:

I hereby declare that all information in this document has been obtained and presented in accordance with academic rules and ethical conduct. I also declare that, as required by these rules and conduct, I have fully cited and referenced all material and results that are not original to this work.

Name, Last Name :

Signature :

ABSTRACT

AERO-STRUCTURAL DESIGN AND ANALYSIS OF
AN UNMANNED AERIAL VEHICLE AND ITS MISSION ADAPTIVE WING

İnsuyu, Erdoğan Tolga
M.Sc., Department of Aerospace Engineering
Supervisor : Assist. Prof. Dr. Melin Şahin

February 2010, 108 pages

This thesis investigates the effects of camber change on the mission adaptive wing of a structurally designed unmanned aerial vehicle (UAV). The commercial computational fluid dynamics (CFD) software ANSYS/FLUENT is employed for the aerodynamic analyses. Several cambered airfoils are compared in terms of their aerodynamic coefficients and the effects of the camber change formed in specific sections of the wing on the spanwise pressure distribution are investigated. The mission adaptive wing is modeled structurally to observe the effect of spanwise pressure distribution on the wing structure. For the structural design and analysis of the UAV under this study, commercial software MSC/PATRAN and MSC/NASTRAN are used. The structural static and dynamic analyses of the unmanned aerial vehicle are also performed under specified flight conditions. The results of these analyses show that the designed structure is safe within the flight envelope. Having completed aero-structural design and analysis, the designed unmanned aerial vehicle is manufactured by TUSAŞ Aerospace Industries (TAI).

Keywords: Cambered Airfoil, Mission Adaptive Wing, Structural Design of a UAV

ÖZ

BİR İNSANSIZ HAVA ARACININ VE GÖREVE UYUMLU KANADININ AERODİNAMİK VE YAPISAL TASARIM VE ANALİZİ

İnsuyu, Erdoğan Tolga
Yüksek Lisans, Havacılık ve Uzay Mühendisliği Bölümü
Tez Yöneticisi : Yrd. Doç. Dr. Melin Şahin

Şubat 2010, 108 sayfa

Bu çalışmada kambur değişiminin yapısal olarak tasarlanmış bir insansız hava aracının (İHA) göreve uyumlu kanadı üzerindeki etkilerini incelenmiştir. Hesaplamalı akışkanlar dinamiği analizlerinde ANSYS/FLUENT ticari yazılımı kullanılmıştır. Farklı kamburlara sahip kanat profilleri aerodinamik katsayıları bakımından karşılaştırılmış ve kanat açıklığı boyunca belirli bölümlerde oluşturulan kambur değişikliğinin kanat basınç dağılımına etkisi de incelenmiştir. Kanadın yapısal modeli kanat açıklığınca değişen bir basınç dağılımının kanat üzerindeki etkisini incelemek için oluşturulmuştur. Söz konusu insansız hava aracının tasarım ve analizleri için MSC/PATRAN ve MSC/NASTRAN ticari yazılımları kullanılmıştır. Belirlenen uçuş durumlarında insansız hava aracının yapısal statik ve dinamik analizleri gerçekleştirilmiştir. Yapılan bu analizler insansız hava aracının uçuş zarfı içinde yapısal olarak güvenli olduğunu göstermiştir. Aerodinamik ve yapısal açıdan tasarımı tamamlanmış insansız hava aracı TUSAŞ Havacılık ve Uzay Sanayisi (TAI) tarafından üretilmiştir.

Anahtar Kelimeler: Kamburlu Kanat Kesiti, Göreve Uyumlu Kanat, İHA Yapısal Tasarımı

to my grandfather

ACKNOWLEDGMENTS

I would like to express my deepest gratitude to my supervisor Assist. Prof. Dr. Melin Şahin for his guidance, assistance, encouragements, insight and patience throughout this study.

I must thank Prof. Dr. Yavuz Yaman, Prof. Dr. Serkan Özgen and Assist. Prof. Dr. Güçlü Seber for their guidance, assistance and teachings.

I would like to express my appreciation to TAI prototype workshop personnel for their help during the manufacture.

I would like to deeply thank my colleagues Levent Ünlüsoy and Evren Sakarya for their help throughout this thesis study.

I would also gratefully appreciate the support and assistance of all my cherished friends but especially Mehmet Efruz Yalçın.

I would like to thank my parents for their guidance and insight and my brother for his care and support.

Finally, this work was supported by The Scientific and Technological Research Council of Turkey, through the project 'TUBITAK/107M103, Aeroservoelastic Analysis of the Effects of Camber and Twist on Tactical Unmanned Aerial Vehicle Mission-Adaptive Wings'. I gratefully acknowledge the support given.

TABLE OF CONTENTS

LIST OF TABLES

TABLES

LIST OF FIGURES

FIGURES

CHAPTER 1

INTRODUCTION

1.1 Scope and Objectives

Cruise efficiency is one of the most important concepts for the design of an air vehicle. Aerial vehicles must be designed for their own decided mission profiles. This phenomenon is a deficiency for most of costly aerial vehicles. Imagine an aerial vehicle which has a broad mission profile and capability of doing different kind of maneuvers. This kind of an aerial vehicle must have a morphing wing which can adapt the plan-form of the wing for a specific mission segment or maneuver. There are lots of researches about performing these kinds of wings called ‘morphing wing’. Increasing or decreasing plan-form area, introducing high lift devices and changing camber are most common ways to morph a wing.

In this study, morphing is introduced by sectional camber change which can also generate twist. This kind of wing enables an unmanned aerial vehicle have a mission adaptive property. The structural design and analysis of this unmanned aerial vehicle having mission adaptive wing is also performed in the scope of this study.

The study was conducted within the scope of a research and development project "Aeroservoelastic analysis of the effects of camber and twist on tactical unmanned aerial vehicle mission adaptive wings" which was supported by the Scientific and Technological Research Council of Turkey (TUBITAK) under the project code of 107M103.

1.2 Lay-Out of the Study

This thesis study is to be presented in four main parts. First part is the background which includes introduction and literature survey chapters. These two chapters introduce basic information about the concept used in the study. Second part is Aerodynamic modeling and analysis of a mission adaptive unmanned aerial vehicle wing. In this part, 2D and 3D aerodynamic modeling and analysis are presented as separate chapters. The third part consists of two chapters which are structural modeling and analysis of the mission adaptive wing and the unmanned aerial vehicle. The fourth and the last part of this thesis study includes discussion and conclusion chapters.

CHAPTER 2

LITERATURE SURVEY

2.1 Morphing Aircraft

Capability of changing the planform of the wing during flight can be referred to "Morphing". This capability may result in economical fuel consumption, increase in mission adaptability and performance. Fixed wing aircraft are designed for considering the flight envelope and the mission profiles. The efficiency of these aircraft can be observed only within their mission profiles. For instance, fixed wing aircraft which are designed for high altitude level flight is not suitable for a dog fight. The aim of a morphing wing is adaptation of the wing within of the entire mission profile. Understanding how birds fly is an inspiration for the researches that has been carried out [1]. Birds can morph their wing shape to enhance flight performance and maneuverability in different flight conditions.

Figure 2.1.1: Swift Wings during Fast Glides (left) and Turning (right) [2]

Swifts typically sweep their wings back during fast glides and extend them while turning. Concept of morphing aircraft can be developed by the enhancement of materials and actuation technology.

NASA references morphing as ‘efficient, multi-point adaptability’ in the future flight vehicles research [1]. The efficiency indicated here means mechanical simplicity and weight reduction of the system. The morphing aircraft is defined as a vehicle which can change its shape for several different mission roles resulting in the idea that it is a multi-role aircraft [3]. The aircraft can fulfill this concept by using “morphing technologies” (e.g. innovative actuators, effectors, mechanisms).

The leading and trailing edge control surfaces and high lift devices that are used by traditional aircraft have the disadvantages of being complex and having gaps and external devices which result in an increase of drag. These systems also come with the reliability problems. Whereas in the morphing aircraft concept usage of smooth and deformable leading and trailing edges or fully deformable airfoil sections become possible.

2.2 Morphing Research Programs

Mission Adaptive Wing (MAW) program

In the early 1980s, a “mission adaptive wing” (MAW) [4], which is shown in Figure 2.2.1 , was used on F-111 aircraft to replace its supercritical wing. This was a part of the Advanced Fighter Technology Integration (AFTI) program which was started by the NASA and the US Air Force.

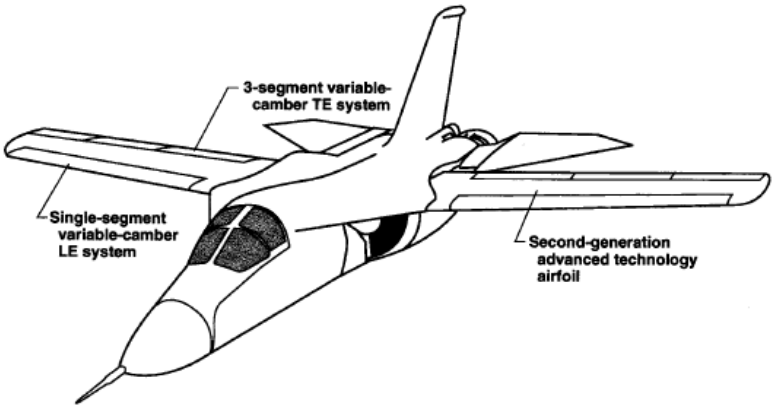

Figure 2.2.1: MAW Modifications to F-111 (From NASA TM-4606)

The mission adaptive wing concept composes of several hinge points and mechanical actuators which make it possible to change the camber of the wing during flight. The drag reduction capability of the camber change on a trimmed flight can be seen in Figure 2.2.2 which shows the test results for two different Mach numbers for both variable camber and baseline aircraft.

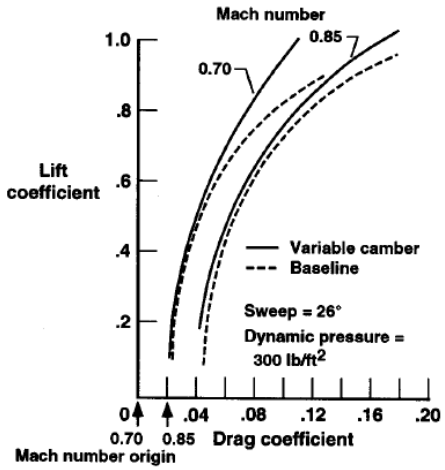

Figure 2.2.2: Flight-Determined Drag Polar Comparison (From NASA TM-4606)

As it can be seen in Figure 2.2.2 drag reduction is nearly 8 percent at the design cruise point, which is C_L=0.4 and M=0.70, and increases up to 20 percent at the off design condition, which is C_L=0.8 and M=0.70.

Although this test figured out that the variable camber was beneficial mostly in terms of drag, the wing was too heavy and complex for practical applications. Then the main problem became finding the easy way of bending the wing without losing the stiffness and strength for not to lose the capability of carrying high loads that an aircraft would be exposed during flight. In addition to this it was important to have small motors which would fit inside narrow space.

Smart Wing program

In 1995, DARPA (Defense Advanced Research Projects Agency) initiated the Smart Wing program [5] which had the scope of combining the benefits of variable camber of MAW and variable wing twist of Active Aeroelastic Wing (AAW). The main objective of this program was improving the aerodynamic and aeroelastic performance of military aircraft by developing smart technologies and showing the novel actuation systems which would yield the performance increasing shape control. The smart wing uses nickel-titanium (NiTi) shape-memory-alloy (SMA) for the actuation of the trailing edge control systems, a SMA internal torque tube, as shown in Figure 2.2.3, for the achievement of hinge-less, smoothly contoured shape control and variable spanwise twist. As these devices avoid the usage of flow disturbing hinge lines the smart wing comes with a great advantage when compared to the conventional wings.

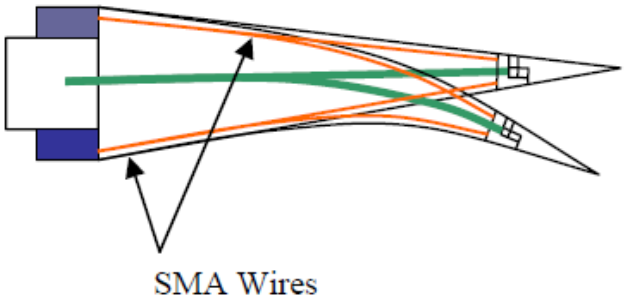

Figure 2.2.3: Smart Technologies [5]

NASA's Morphing Aircraft program

In 2002, NASA established a morphing aircraft program [1], to investigate adaptive materials and structures, micro active flow control and biologically inspired technologies. This project was to combine micro fluid dynamics to the small/large-scale structure shape change. In addition to this, one of the main objectives was to find improvements by intersecting the disciplines of intertwined functions of vehicle aerodynamics, structures and controls. For the development of future air and space vehicles it was important to use multi-disciplinary approaches of advanced adaptive technologies. An artistic concept of a morphing airplane developed in this program can be seen in Figure 2.2.4.

Figure 2.2.4: Morphing Airplane (NASA)

DARPA's Morphing Aircraft structures program

Continuing research, which was established by DARPA, aims to create shape-changing, multi-mission aircraft using smart materials. In this project, DARPA investigates aspects like 200% change in aspect ratio, 50% change in wing area, 50% change in wing twist, and a 20-degree change in wing sweep. "Sliding skins", shown in Figure 2.2.5, and "folding wings", shown in Figure 2.2.6, concepts may constitute examples of morphing of a plane from a fast, attack configuration to a slower long distance shape [6].

Figure 2.2.5: Sliding Skins Concept (Image: NexGen)

Figure 2.2.6: Folding Wing Concept (Image: Lockheed Martin)

One of the most important motivations, which increase the interest in the shape change of the wing during the flight, is not needing traditional flight-control surfaces which are large source of radar reflections. In addition to this, by using morphing wing concept it is possible to improve performance at two dissimilar flight conditions. DARPA focuses on the smart materials-based solutions as it seems changing wing shapes by using more conventional, actuator-based approaches is less efficient. The most important issue that would lead this project to success is the capability of sustaining the aerodynamic forces and aircraft loads during the flight conditions. As the weight of the morphing wings will be higher than the conventional ones it is important to overcome this disadvantage by obtaining high performance enhancements [7].

CHAPTER 3

2D AERODYNAMIC MODELING AND ANALYSIS OF MISSION ADAPTIVE WING

3.1 Introduction

Aerial vehicle wings require airfoil sections with different cambers during flight in order to sustain cruise efficiency. In this section, NACA4412 airfoil is selected as the main airfoil to be altered by using specified techniques in means of having different camber values. Then 2D aerodynamic analyses are performed with these varied cambered airfoils to examine the changes in aerodynamic coefficients.

3.2 Preliminary Design Phase

There is a basic inconsistency in the design of aerial vehicle wing considering aerodynamic aspects. For instance, wing requires high wing loading and less camber during level flight, on the contrary; higher camber values are required during takeoff and landing. This concept results in requirement of a larger wing area. Any kind of wing design with fixed geometry isn't sufficient for this kind of requirements. Considering this phenomenon, there are lots of researches in aviation history aiming to change the camber. Flap and aileron are the most commonly used structures enabling the increase in camber of airfoil. Traditional control surfaces; flaps and ailerons of an airliner can be seen in Figure 3.2.1 [8].

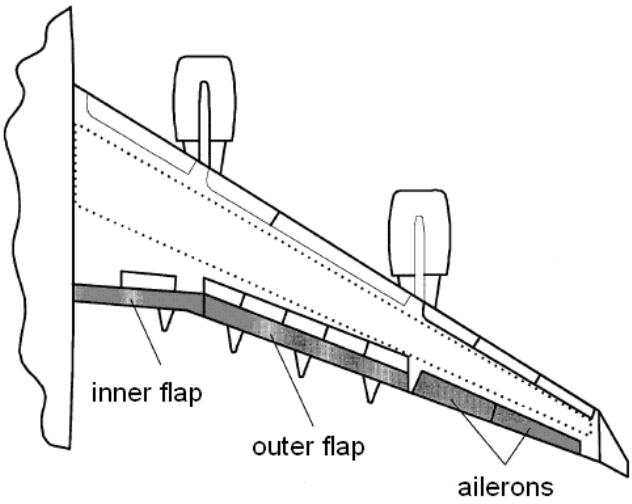

Figure 3.2.1: Control Surfaces as Flaps and Ailerons [8]

There are different types of flap structures which are used for acquiring high lift force. Not only most of these structures are in the trailing edge of the wing, but also there are special applications where these flaps take place in the leading edge of the wing [9].

The capability of increasing the camber of airfoil in this study involves two typical flaps called plain and slotted flaps. Plain flaps are connected to the trailing edge of the wing with hinges. Mainly these structures are located in the last 30% of chord length. Maximum lift is mainly performed with 40°-45° downward deflection of flaps. A downward deflected plain flap is shown in Figure 3.2.2 [10].

Figure 3.2.2: Plain Flap [10]

Slotted flap is basically a type of a plain flap where there is a space between wing and flap structure. This kind of design delays the separation of high pressured air flow coming from lower surface of the wing by guiding the flow passing to upper surface through the slot and leave the wing in the trailing edge. In this circumstance, flow performs a high lift and a low drag. A typical slotted flap is shown in Figure 3.2.3 [10].

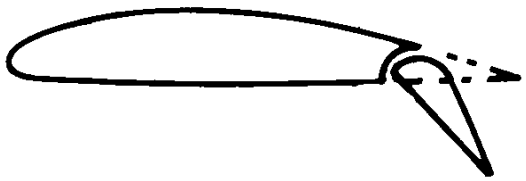

Figure 3.2.3: Slotted Flap [10]

Figure 3.2.4 shows the change of wing lift coefficients (C_L) of mentioned two types of flaps due to change in angle of attack (α) [10]. Flat and slotted flap enhance the lift curve slope by shifting the zero lift angle of attack (α_{0L}) value to left in horizontal axis. If this kind of modification with plain flaps compared with a wing without flap at a fixed angle of attack, a visible increase in lift occurs in a wing with flaps. Despite this increase, the reduction of the angle of attack where stall occurs is going to result in an earlier stall. On the contrary, this stall effect is mostly the same in slotted flapped wing compared with a wing without flap.

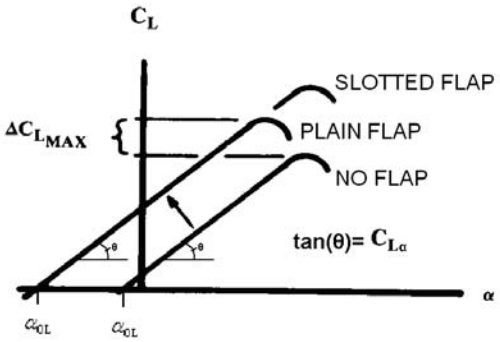

Figure 3.2.4: The Effect of Flap Usage on Lift Curve Slope ($C_{L\alpha}$) and Angle of Attack [10]

The relation between the stall speed and maximum lift coefficient ($C_{L,max}$) is shown in the equation below;

$$V_s = \sqrt{\frac{2W}{\rho S C_{L,max}}} \qquad \text{(Eqn. 3.1)}$$

In this equation W and S are the symbols for the total weight and the wing area of the aircraft respectively. The density of air is shown by "ρ". An efficient flap give a higher $C_{L,max}$ value resulting in a lower stall speed (V_s) so the aircraft avoids the problems that may occur during landing. For plain flap, the increase in lift can be calculated by the methodology described in reference [10]. Below one can find the main steps to follow in the calculation of increase in lift.

1. Lifting coefficient for an airfoil having a specified angle of attack can be calculated as;

$$C_L = C_{L\alpha}(\alpha - \alpha_{0L}) \qquad \text{(Eqn. 3.2)}$$

In this expression $C_{L\alpha}$ is the lift curve slope and α_{0L} is zero lift angle of attack. These parameters were shown in Figure 3.2.4.

2. In flap's downward condition, there is a decrease in zero lift angle of attack but in low angle of attack but there is no change in the lift curve slope. The decrease in zero lift angle of attack can be calculated as follows;

$$\Delta \alpha_{0L} = -(1/ C_{L\alpha})(\partial C_L/\partial \delta_f)\,\delta_f \qquad \text{(Eqn. 3.3)}$$

In the equation, 'δ_f' is the angular deflection value of the flap and '$\partial C_L/\partial \delta_f$' can be found by the help of Figure 3.2.5 [10]. In the figure 'c' is chord length and 'c_f' is the chord length of the plain flap.

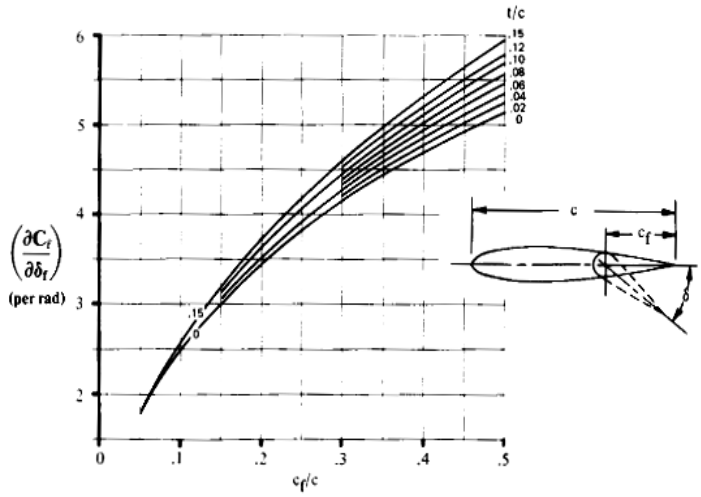

Figure 3.2.5: Theoretical Increase in Lift for Plain Flaps [10]

This approach gives the approximate lift which can be gained by the use of a flap. The values calculated with this approach will be compared with the values calculated by using Computational Fluid Dynamics (CFD) approach. Therefore; instead of a wing configuration with traditional flaps which is efficient only for a limited flight condition, the design of a wing with adaptive camber change enhancing aerodynamic efficiency with an instantaneous change in flight regime is the primary objective. This kind of a wing can increase important performance characteristics like endurance result in less fuel consumption by increasing lift to drag ratio during flight [11, 12]. Figure 3.2.6 and Figure 3.2.7 show the endurance increase with improved lift distribution over span.

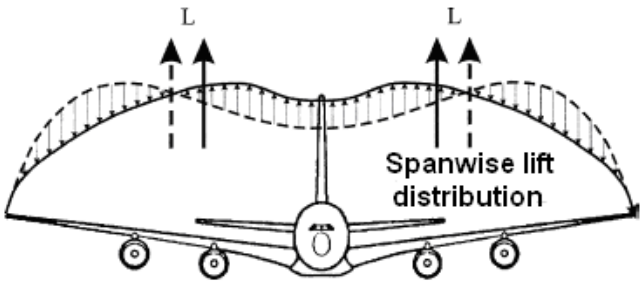

Figure 3.2.6: The Effect of Variable Camber to Spanwise Lift Distribution [8]

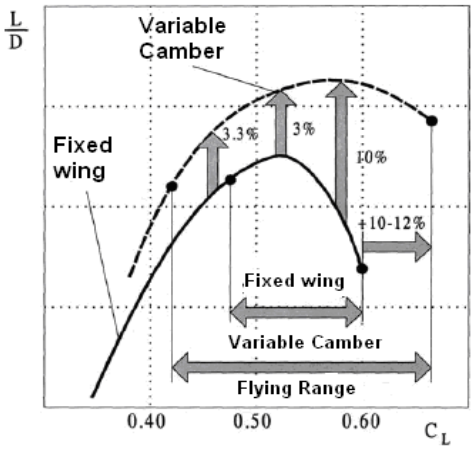

Figure 3.2.7: The Effect of Variable Camber to Lift to Drag Ratio [11, 12]

There are many new approaches about variable cambered wings. These are in the form of "chordwise camber change" and "spanwise camber change" as shown in Figure 3.2.8 (a) and Figure 3.2.8 (b) respectively. Not only an increase in camber but also a decrease in camber is possible. This enables having different or opposite directional lift in each wing so different control surfaces, like ailerons can be simulated by the help of this approach.

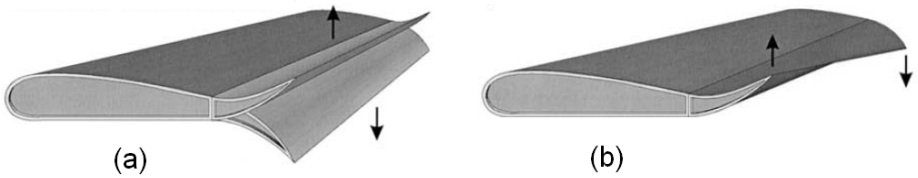

Figure 3.2.8**:** Chordwise (a) and Spanwise (b) Camber Change [8]

3.3 Modeling and Analysis

In this part of the study, 2D incompressible viscous flow is simulated by ANSYS®/FLUENT [13] program over differently cambered airfoils using NACA4412 airfoil as a basic airfoil to be altered. By the help of this simulation the effect of camber change was examined by means of aerodynamic coefficients. Following procedures are performed to establish this study.

- Creating initial mesh and boundary zones for the analysis,
- Changing camber parameters ,
- Adjusting mesh for cambered airfoils using spring analogy [14],
- Modeling of 2D viscous flow over NACA4412 airfoil and boundary conditions,
- Checking convergence criteria for CFD analysis.

In the CFD analysis, the airfoil has 1 m chord length (c=1 [m]), Mach number is 0.1 (M= 0.1) and the angle of attack is 0 (α=0) as shown in Figure 3.3.1.

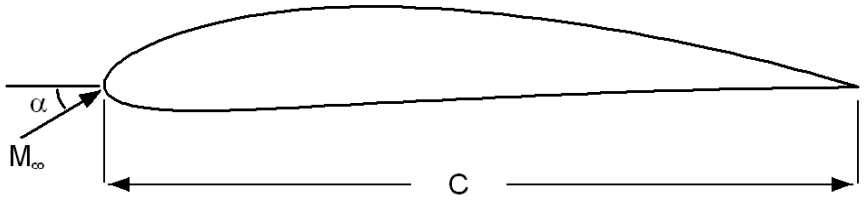

Figure 3.3.1**:** NACA4412 Airfoil and Analysis Parameters

In the CFD analysis Finite Volume Method is applied and Spalart-Allmaras [15] model was used for turbulence modeling. Calculated aerodynamic coefficients C_l and C_d are tabulated according to different type of cambered airfoils in the conclusion section.

3.4 Generating Initial Mesh and Boundary Zones

In the mesh generation process, the method outlined in [16] was applied. The mesh fields and the boundary condition zones for NACA4412 airfoil is presented in Figure 3.4.1.

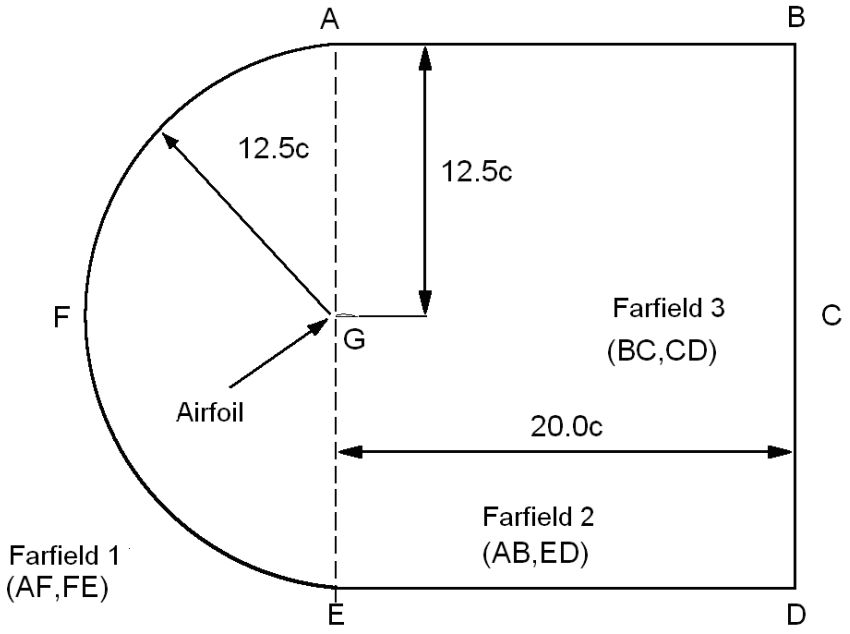

Figure 3.4.1**:** Boundary Condition Zones for the Analysis

Solution domain for the NACA4412 airfoil is generated by using ANSYS®/GAMBIT [17]. The solution domain consists of quad elements performing C-type mesh. The solution domain for the deflected profiles will be generated by using 'spring analogy' [14] from this solution domain. The solution domain on NACA4412 profile is presented in Figure 3.4.2.

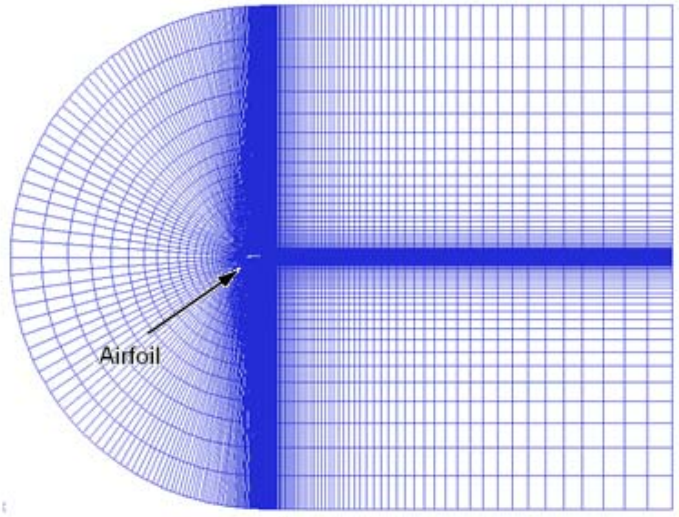

Figure 3.4.2: NACA 4412 Airfoil and the Solution Domain

3.5 Parameters for Camber Change

For 4-digit NACA series airfoils, mean camber line and the vertical distances from the line to the upper and lower surfaces are defined by means of dimensionless distance ‘x’ in the fallowing equations [18].

$$y_{camber} = \frac{m}{p^2}(2px - x^2) \qquad 0 \le x \le p \qquad \text{(Eqn. 3.4)}$$

$$y_{camber} = \frac{m}{(1-p)^2}\left[(1 - 2p) + 2px - x^2\right] \qquad p \le x \le 1 \qquad \text{(Eqn. 3.5)}$$

$$\pm y = \frac{t}{0.2}\left[0.2969\sqrt{x} - 0.126x - 0.3516x^2 + 0.2843x^3 - 0.1015x^4\right] \qquad \text{(Eqn. 3.6)}$$

In the above equations ‘m’ variable is for the maximum camber ratio and ‘p’ variable is for the chordwise position of maximum camber and ‘t’ is for the ratio of maximum thickness to chord. For NACA4412 profile m, p, and t are 0.04, 0.4 and 0.12 respectively.

Mean camber line coordinates of airfoil defined in Equations 3.4 and 3.5 in the sections where the camber change will be applied by using cubical and linear functions .The first derivatives and the functions are always polynomial according to the ‘*s*’ variable in the equations below. These functions enable camber change like a flap deflection in trailing edge.

$$\Delta y_{camber} = \lambda s^2(3L - s) \qquad 0 \le s \le L \qquad \text{(Eqn. 3.7)}$$

$$\Delta y_{camber} = \lambda L^2(3s - L) \qquad L \le s \le 1 \qquad \text{(Eqn. 3.8)}$$

Δy_{camber} expression defined in Equations 3.7 and 3.8 expresses the vertical displacement change of mean camber line. ‘s’ term here represents the dimensionless distance, which changes from zero to one and measured on the camber line, defined from the start of the camber change towards trailing edge. ‘λ’ is the constant that shows the direction and magnitude of the shape shift. ‘L’ is a number changing from zero to one representing region of the camber change functions defined in the Equations 3.7 and 3.8. The case where L is equal to zero indicates the shape change like a plain flap configuration.

For ‘s’ values which are higher than the L values, mean camber line shifts as a whole as like the plain flap configuration. For the lower values, coordinates of the mean camber line changes dependent on a cubical function of ‘s’. The idea behind using the camber change as piecewise functions is that the mean camber line formed in the airfoil section should be smooth and continuous when compared with a hinged plain flap mechanism. By this way, negative aerodynamic effects, like the local increment of the drag caused by the sharp changes in the flow direction, are reduced.

In this study, value of the L was chosen to be 0.333 to obtain a smooth and continuous camber line as well as a similar condition to plain flap.

3.6 Cambered Airfoils

In this part, the airfoil section models are generated by using the aforementioned method. The airfoils generated will be named according to deflection parameters. From now on ‘Δte’ represents the displacement of trailing edge point in terms of chord length like ‘Δte= -0.04c’ means downward deflection of the trailing edge point with an amount of 4% of chord length, and ‘dp’ shows where the deflection takes place on chord. ‘dp=0.60c’ means airfoil deflection starts at 60% of chord length measured from leading edge. In the analysis performed, 191 cambered airfoils are studied as a research domain. The cambered airfoils are presented as points regarding the deflection parameters in the research domain in Figure 3.6.1. Cambered airfoils

where dp=0.60c set as constant and changes in Δte is presented in Figure 3.6.2 and Δte= -0.06c set as constant where changes in dp is presented in Figure 3.6.3 as illustrations.

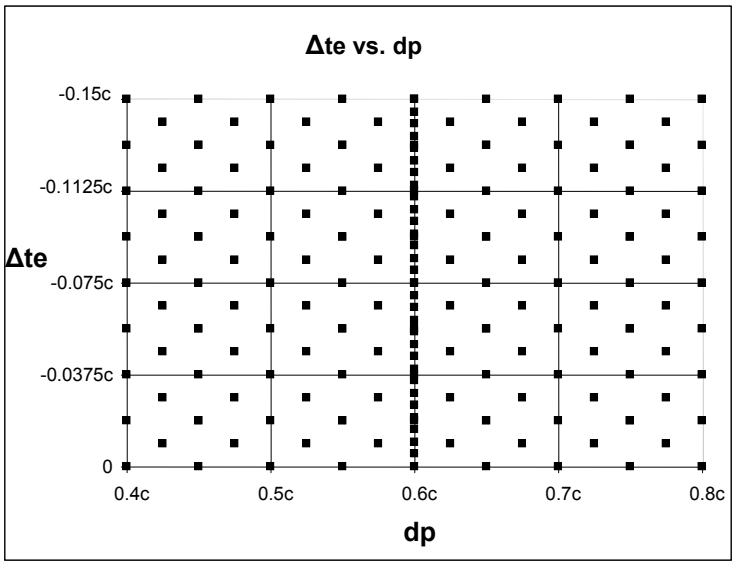

Figure 3.6.1: Cambered NACA4412 Airfoils Research Domain

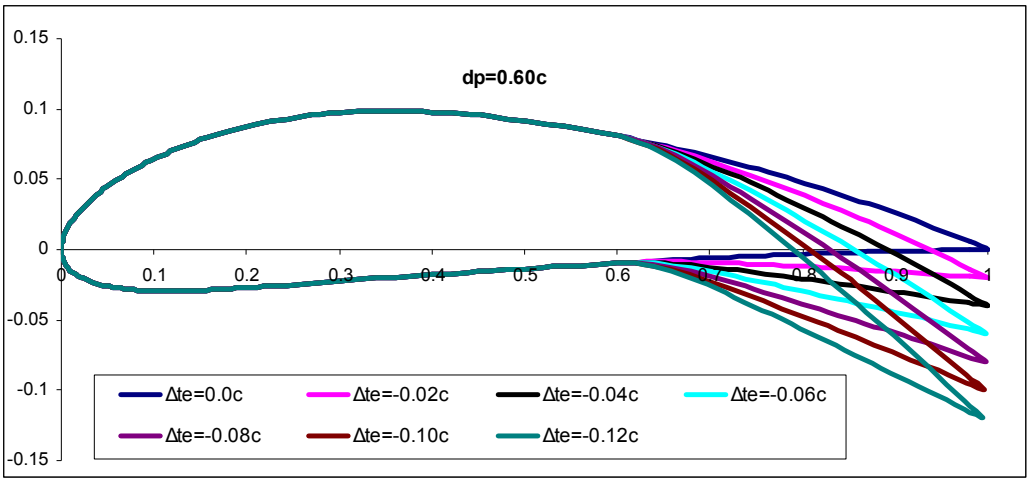

Figure 3.6.2**:** Cambered NACA4412 Airfoils Constant dp

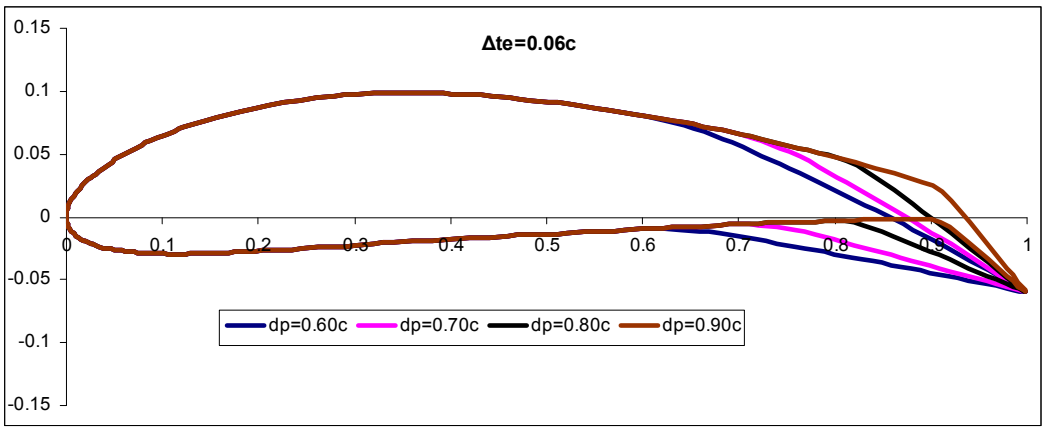

Figure 3.6.3: Cambered NACA4412 Airfoils Constant Δte

3.7 Adjusting Mesh for Cambered Airfoils Using Spring Analogy

Deflections enabling camber changes the trailing edge point with the coordinate (1.0) to a new point depending on the deflection parameter. Generating this camber change on the airfoil in the generated mesh by using spring analogy causes some problems in CFD mesh as shown in Figure 3.7.1.

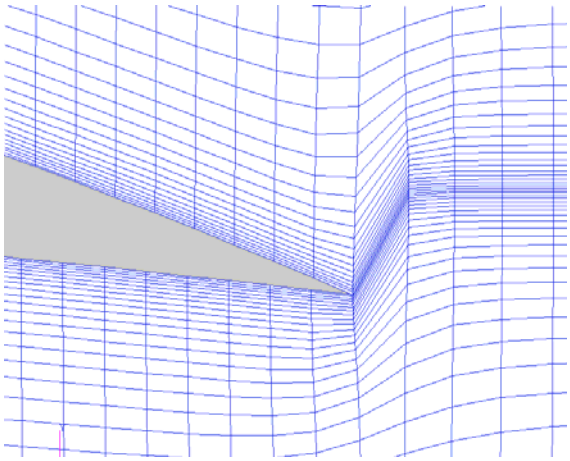

Figure 3.7.1: Mesh Problem around Cambered NACA4412 airfoil

The trailing edge meshes deflect with the airfoils' trailing edge since the mesh elements chase the airfoil grid point within the mesh. Fixing this problem is done by

moving the leading edge point as good as possible to its original value. This kind of approach can be done by rotating the airfoil around its leading edge point (0.0). For the morphed airfoil in the trailing edge point we have a different point than (1.0) so to fix the trailing edge point of the morphed airfoil to the original case the morphed airfoil should be rotated with a rotation angle θ=3.42 shown in Figure 3.7.2.

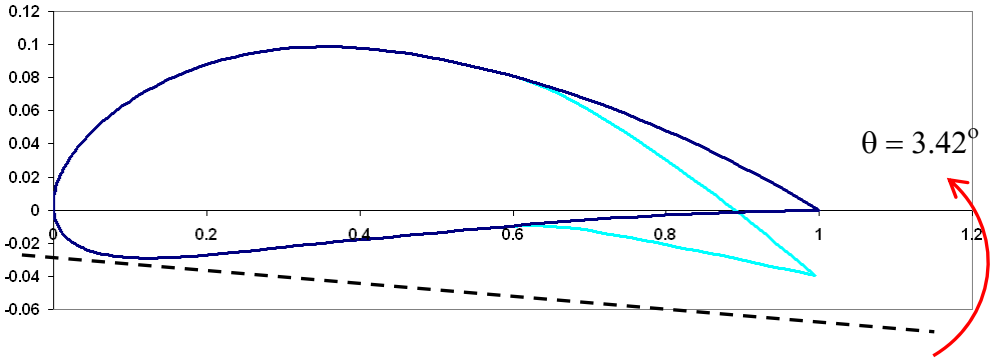

Figure 3.7.2: Rotation of Cambered NACA4412 Airfoil

As the rotation angle differs for each cambered airfoils, some cambered airfoils and required rotation angle for each one are shown in Figure 3.7.3.

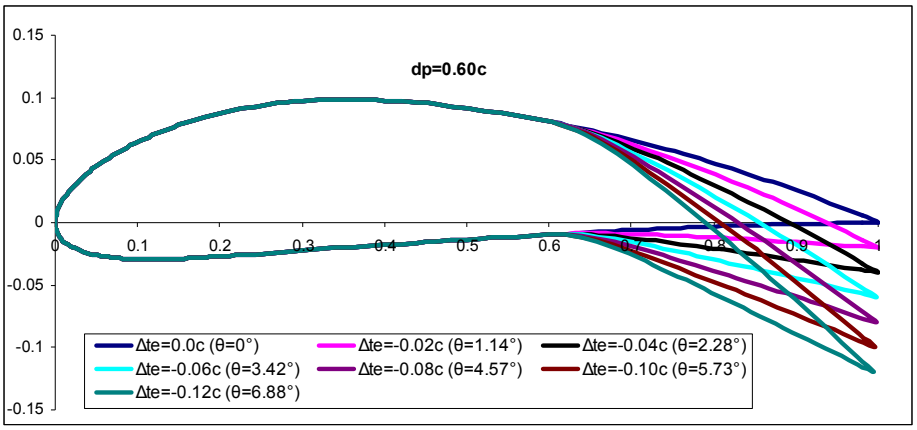

Figure 3.7.3**:** Cambered NACA4412 Airfoils with Rotation Angles

This enables to have fine mesh cells in the trailing edge before adapting the meshes by using spring analogy. The mesh structure of the rotated morphed airfoils at the trailing edge part can be seen in Figure 3.7.4.

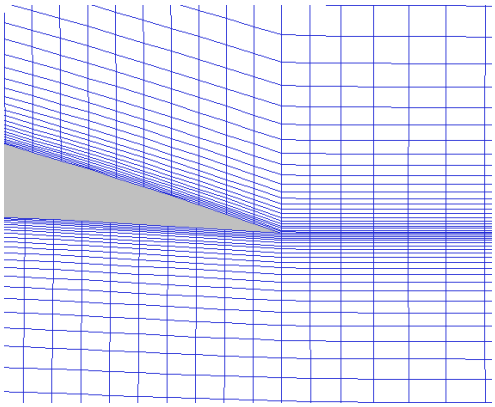

Figure 3.7.4: Rotated Cambered NACA4412 Airfoil

According to this rotation the airfoil is given an angle of attack $\alpha = \theta$ in the analysis so that the results at the angle of attack $\alpha=0$ can be obtained since there is no difference aerodynamically analyzing the cases shown in Figure 3.7.5 and Figure 3.7.6. Rotated airfoils are used in the analysis considering the proper mesh.

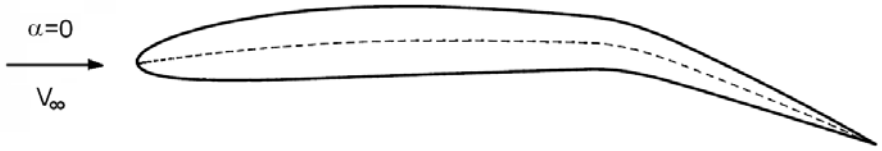

Figure 3.7.5: Position of Non-rotated Cambered NACA4412 Airfoil in the CFD Analysis with $\alpha=0$

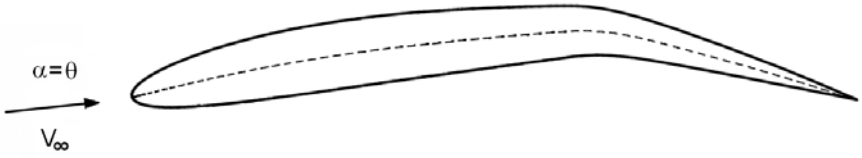

Figure 3.7.6**:** Position of Rotated Cambered NACA4412 Airfoil in the CFD Analysis with $\alpha= \theta$

3.8 Modeling 2D Incompressible Flow

While modeling the incompressible flow, the following circumstances are taken into account;

1. "ANSYS®/FLUENT 2ddp" (2D double precision) is selected as a solution type.
2. Pressure based solution is selected and node based gradient option is used.
3. Spalart-Allmaras [15] model is selected for viscous condition. Spalart-Allmaras model is a simple one-equation model that solves a modeled transport equation for the kinematic (turbulent) viscosity. Spalart-Allmaras model is designed for aerospace applications involving wall bounded flows and has shown to give good results for boundary layers subjected to adverse pressure gradients and this model is commonly used for airfoil analysis.
4. Air is selected as the fluid with the following specific properties. (Density=1.225 [kg/m^3], Viscosity= 1.7894E-05 [kg/m-s]).
5. For incompressible flow, the operating pressure is set to zero in order to minimize the errors due to pressure fluctuations.
6. For boundary conditions, all the far fields are set to pressure far field with the properties of Gauge Pressure = 101325 [Pa], M=0.1 (34 [m/s]), and X component of the flow field = cos(θ) and Y component of flow field = sin(θ) since an angle of attack is given due to rotation.
7. Velocity inlet boundary condition zone, Far field 1 is defined for the initialization.
8. Convergence criterion is selected as 1.E-06 to monitor the residuals.

3.9 Convergence Criteria Check for 2D CFD Analysis

The residuals should be monitored and during the iteration process those values should decrease to obtain an accurate result [19]. The monitoring graph showing the relation between the residuals and the iteration number is presented in Figure 3.9.1.

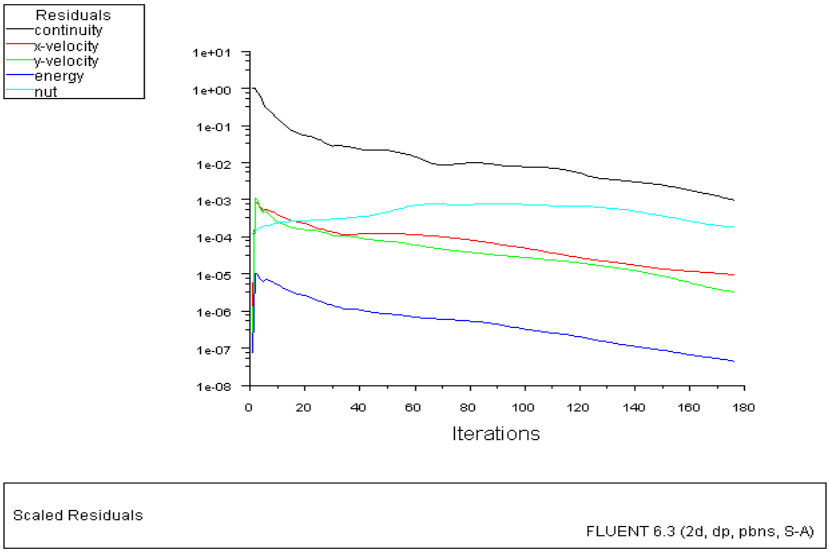

Figure 3.9.1**:** Change of Residuals during Iteration Process

There must be a convergence value for lift and drag coefficients (C_l, C_d). In Figure 3.9.2 and Figure 3.9.3 converged values of these aerodynamic coefficients for an arbitrary case as an example are presented. The accuracy of these values is tested by the next convergence criteria called 'Wall Y^+ curve' [20].

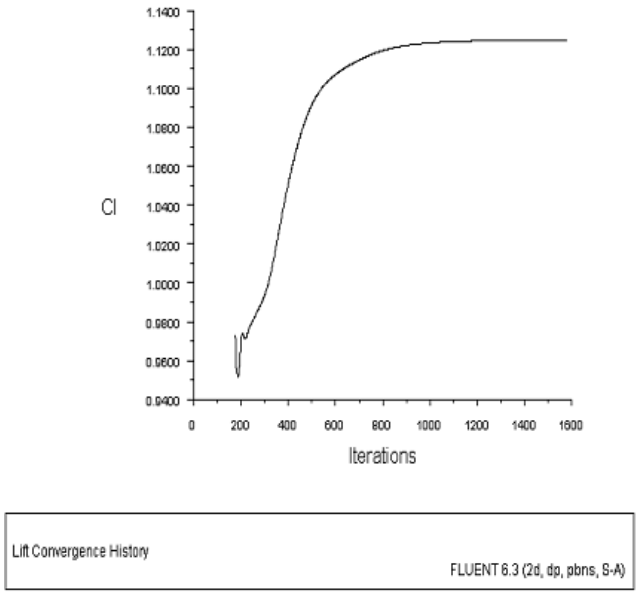

Figure 3.9.2**:** Lift Coefficient Convergence History

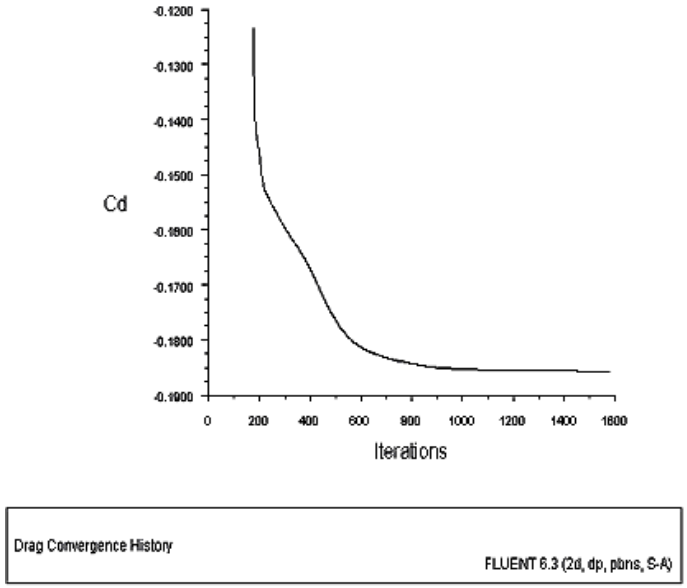

Figure 3.9.3**:** Drag Coefficient Convergence History

After convergence observed, Wall Y^+ curve must be examined. This value is calculated in terms of dimensionless wall distance for wall boundary flows where the airfoil surface has a boundary zone as wall. Y^+ is often referred to simply as

"Y plus" and is commonly used in boundary layer theory and in defining the law of the wall.

In the below equation 'u' is the friction velocity at the nearest wall, 'y' is the distance to the nearest wall and 'v' is the local kinematic viscosity of the fluid.

$$Y^{+} = \frac{u.y}{v} \qquad \text{(Eqn. 3.9)}$$

For Spalart-Allmaras model, this value must be either too small or larger than 30. For 2D airfoil lift coefficient value is better estimated where Y^{+} value is in the region of values 30 to 150. This region is specified for the Spalart-Allmaras model used in airfoil CFD analysis. Y^{+} curve for an arbitrary analysis is presented as an example in Figure 3.9.4 . This curve represents the Y^{+} values for upper and lower surfaces of the airfoil. Maximum value of this curve is the criteria to check for convergence accuracy.

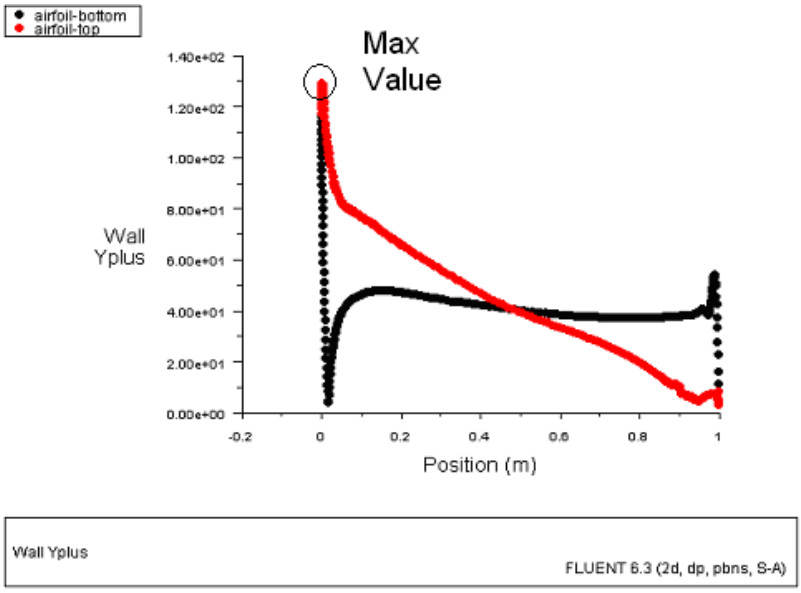

Figure 3.9.4: Y^{+} Curve

Maximum value of 130 shows that the convergence is achieved. If this value is not within the range, the solution domain cells must be adapted by dividing the cell

nearest to the airfoil wall into 4 pieces as presented in Figure 3.9.5. This approach halves the distance to the nearest wall which alters the Y^+ curves for a better convergence for aerodynamic coefficients.

Figure 3.9.5: Solution Domain Adaptation

3.10 Analysis Results

The analyses are performed for different cambered airfoils. The airfoils generated within the range where Δte varies between 0.0c and -0.15c and dp varies between 0.4c and 0.8c leading to 191 cambered airfoils within the analysis domain. The results are given as contour plots for C_l, C_d and L/D in Figure 3.10.1, Figure 3.10.2 and Figure 3.10.3 respectively.

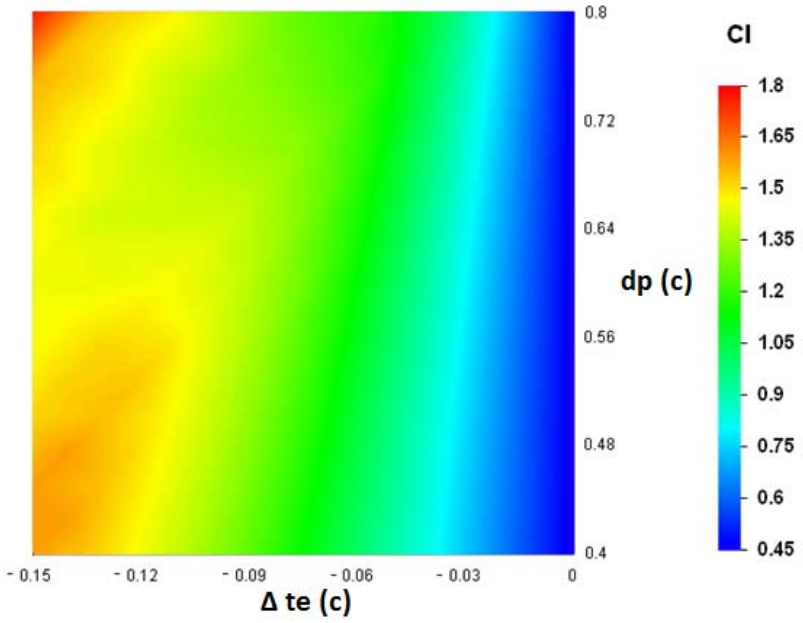

Figure 3.10.1: C_l Contour Plot for Analysis Domain

Minimum C_l value of 0.4502 is obtained where there is no camber on the NACA4412 airfoil and the maximum C_l value of 1.7668 is obtained for the airfoil where Δte=-0.15c and dp=0.8c for the cambered airfoil.

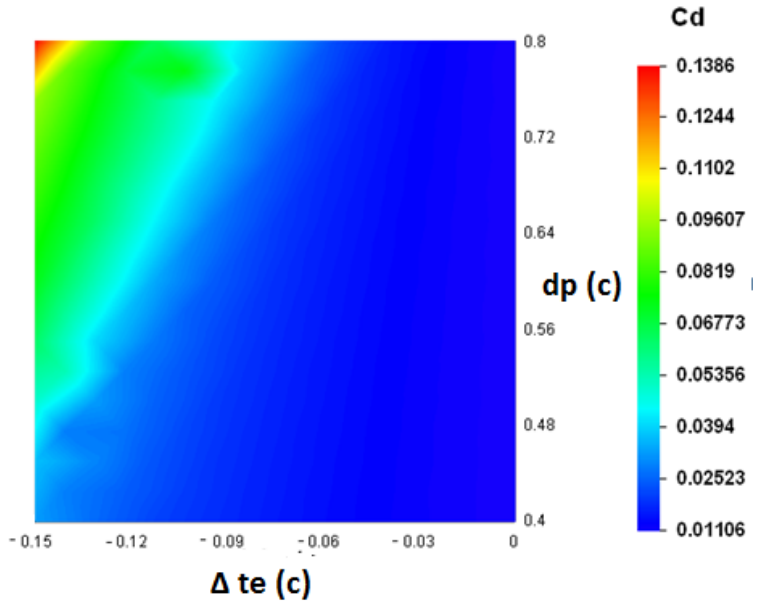

Figure 3.10.2: C_d Contour Plot for Analysis Domain

Minimum C_d value of 0.01106 is obtained where there is no morphing on the NACA4412 airfoil and the maximum C_d value of 0.1386 is obtained for the airfoil where Δte=-0.15c and dp=0.8c for the morphed airfoil.

Higher camber not only increases the lift but also increases the drag. For finding the optimum value of the deflection parameters for the best condition, L/D is considered to decide for the efficient cambered airfoil.

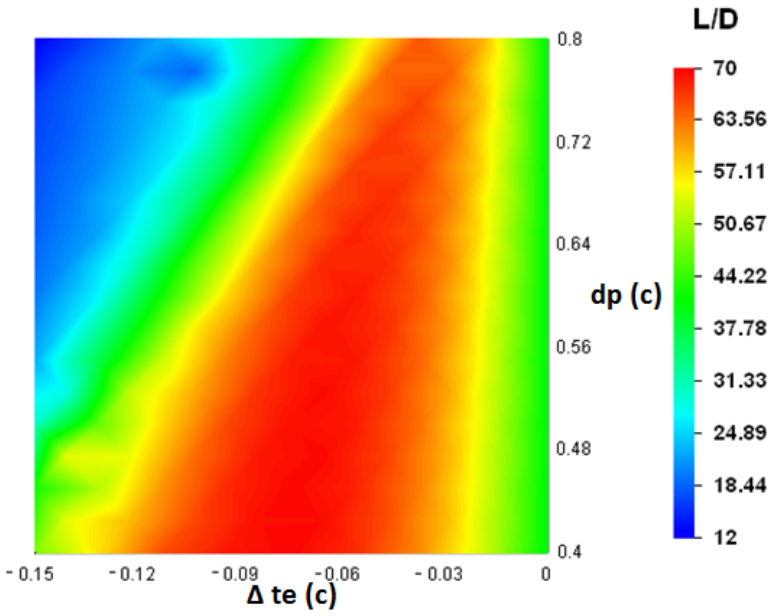

Figure 3.10.3**:** L/D Contour Plot for Analysis Domain

Minimum L/D value of 12.75 is obtained where Δte=-0.15c and dp=0.8c for the morphed airfoil and the maximum L/D value of 69.71 is obtained where Δte=-0.075c and dp=0.45c for the morphed airfoil. Figure 3.10.3 clearly shows that for some cases it is possible to have close L/D ratios for different cambered airfoils.

3.11 Conclusion

Considering the analysis performed on the research domain the best airfoil is the one where Δte=-0.075c and dp=0.45c. dp value restricts the design of a wing that deflects nearly from half of the chord regarding the structural parameters. Therefore, dp value of 0.6c is chosen and fixed for the wing which is used in 3D analysis [21]. Fixing dp value to 0.6c lowers the constraints of morphed airfoils and leaves Δte as the only parameter for the detailed analysis.

The results of the cambered airfoils where dp=0.6c and Δte changes for aerodynamic coefficients (C_l; lift coefficient, C_d; drag coefficient, C_m; moment coefficient) are tabulated in Table 3.11.1. The result shows the values of aerodynamic coefficients of the 2D morphed air foils at zero angle of attack and the improvement in C_l can be easily seen by comparing the values with that of the original NACA4412 from Table 3.11.1. The results also show comparison with the C_l values calculated for plain flap deflection [10].

Table 3.11.1**:** Aerodynamic Coefficients for Cambered Airfoils (dp=0.6)

Δte	**0.0c**	**-0.02c**	**-0.04c**	**-0.06c**	**-0.08c**	**-0.10c**	**-0.12c**
C_l	0.4502	0.6904	0.9193	1.1344	1.3050	1.5574	1.6922
C_l [10]	0.4000	0.6652	0.920	1.1696	1.4244	1.6688	1.9184
C_d	0.0111	0.0124	0.0142	0.0169	0.0210	0.0578	0.0714
C_m	0.2133	0.3039	0.3941	0.4813	0.5520	0.6798	0.7426
C_l /C_d	40.7201	55.6774	64.7394	67.1243	62.1429	26.9446	23.7009

It can be seen from the Table 3.11.1 that the best L/D is encountered where Δte=-0.06c with a value 67.1243.

The analysis results for related morphed airfoils are also plotted in terms of the aerodynamic coefficients and ratios (C_l , $10C_{d,}$ C_m) and L/D that can be seen in Figure 3.11.1 and Figure 3.11.2.

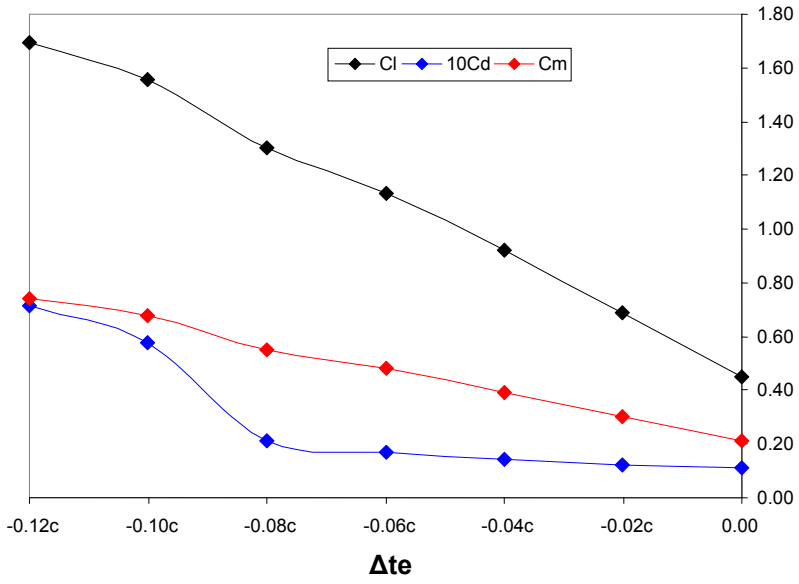

Figure 3.11.1: Aerodynamic Coefficients for Cambered Airfoils (C_l , $10C_{d,}$ C_m)

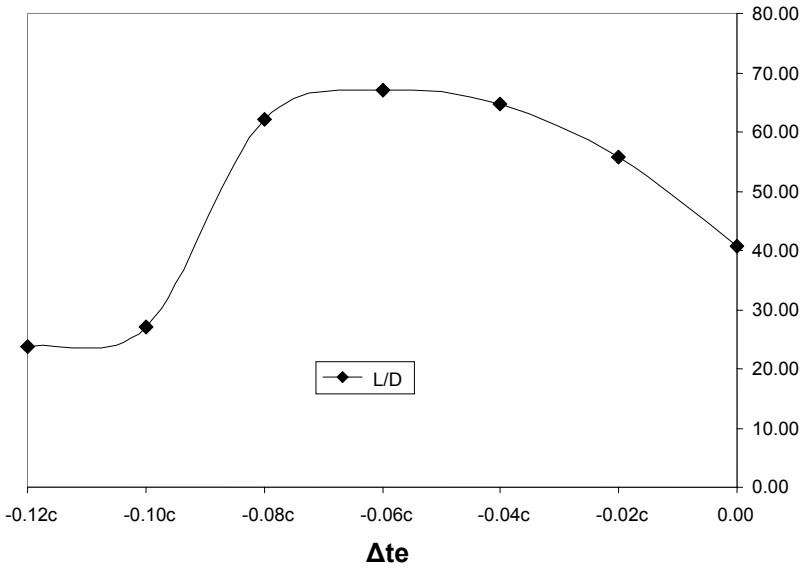

Figure 3.11.2: L/D for Cambered Airfoils

CHAPTER 4

3D AERODYNAMIC MODELING AND ANALYSIS OF MISSION ADAPTIVE WING

4.1 Introduction

In this chapter, 3D CFD analysis is performed considering the 2D CFD analysis results. The camber change position of the wing is fixed at dp=0.6c in the conclusion of the Chapter 3 taking account to manufacturing and structural constraints. The wing is manufactured in TAI and tested within the scope of the project explained in [21]. The geometric information for the wing to be analyzed in 3D CFD analysis is given in Figure 4.1.1.

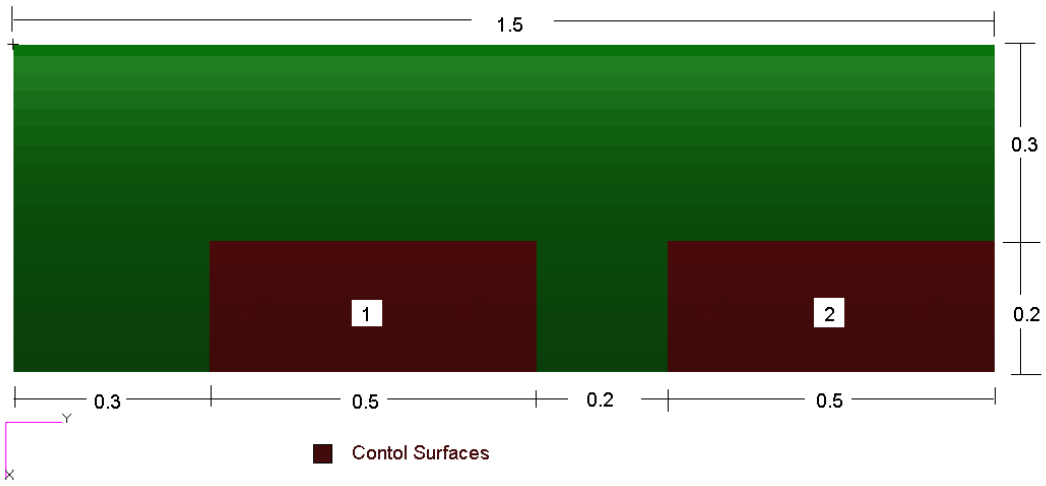

Figure 4.1.1: Geometric Parameters of the Wing [m]

The wing has a 1.5 [m] span and 0.5 [m] chord. Control surfaces placed in the wing are also shown in the same Figure. In this figure, the control surface labeled as 1 can be considered as a flap and the control surface labeled as 2 can be considered as an aileron.

4.2 Mesh Generation for 3D Analysis

In this section of the study, the methodology for the 3D mesh generation is presented [17]. Computer Aided Design (CAD) model for the wing to be analyzed is needed to be imported before the generation of the mesh. 3D CAD model of the wing is created by using MSC®/PATRAN [22] and imported to ANSYS®/GAMBIT in STEP format. The CAD model of the wing having NACA4412 profile (Δte=0.0c) is presented in Figure 4.2.1 . In this model, chord and span is 0.5 [m] and 1.5 [m] respectively.

Figure 4.2.1: CAD Model of the Wing

After importing the geometry in to ANSYS®/GAMBIT, the mesh is generated and 3D solution domain is set. Two different rectangular prisms (named as inner and outer domain) are generated for the solution.

The inner domain is much smaller than the outer domain but it comprises ten times more elements than that of the outer domain. The inner domain is nested in such a way that the pressure gradients are higher in the surface of the wing than the far zones.

Pave type Tri elements are used on wing surface. The inner rectangular prism has the dimensions as X=3 [m], Y=4 [m], Z=2 [m]. The inner volume between the wing and inner rectangular prism is meshed by using TGrid type Tet/Hybrid elements. The growth rate for the elements is 1.09 from the wing surfaces to the inner rectangular prism surfaces. The selection of this small growth size enables dense mesh density in the inner solution domain which is presented in Figure 4.2.2.

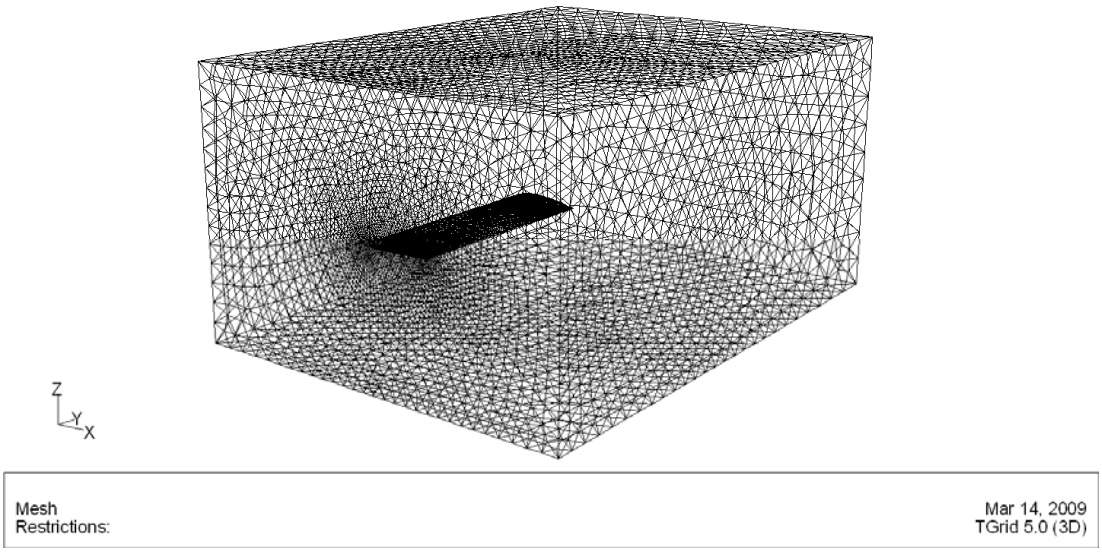

Figure 4.2.2: Inner Solution Domain (Isometric View)

The element concentration is denser over wing surfaces as shown in Figure 4.2.3. This enables a better solution for the pressure gradient on the wing surfaces. Leading and trailing edge of the wing is important from the pressure gradient point of view. Around the edges, the element size is smaller than the element size on the middle section of the wing surfaces.

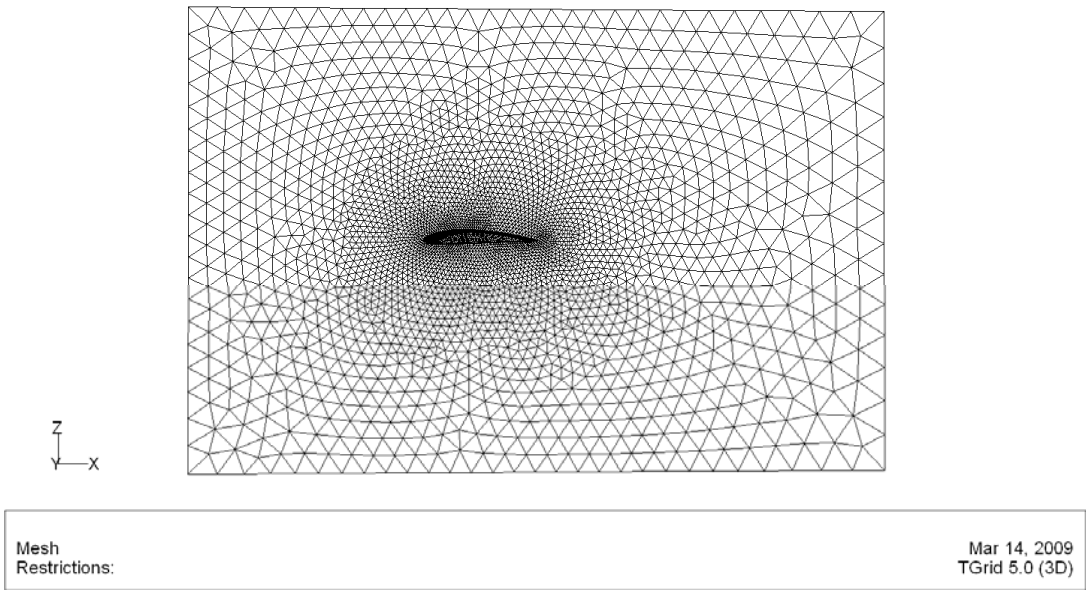

Figure 4.2.3: The Elements over Wing Surfaces in Inner Solution Domain (Side View)

The outer rectangular prism has the dimensions of X=40 [m], Y=15 [m], Z=16 [m]. The volume between the surfaces of inner and outer rectangular prism is outer solution domain where Tgrid type Tet/Hybrid elements are used with a growth rate of 1.2 for the elements from the surface of inner rectangular prism to the surfaces of outer rectangular prism. This growth rate enables a less dense element concentration then the element concentration in inner solution domain since the pressure gradients are lower than the ones in inner solution domain. The generated outer domain is presented in Figure 4.2.4.

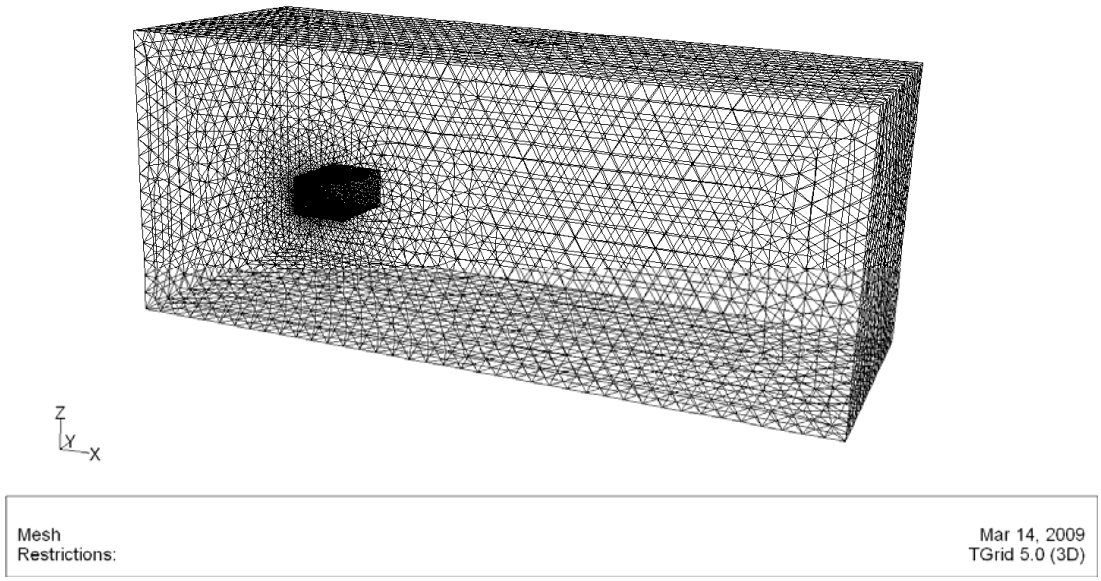

Figure 4.2.4: Outer Solution Domain (isometric view)

The last step of the mesh generation is to define the zones and boundary condition zones before using the generated solution domain in CFD analysis which is performed by using ANSYS®/FLUENT. The boundary condition zones are established by trying to simulate a wind tunnel. Velocity-inlet, pressure-outlet and four symmetry planes take place in boundary condition zones which are shown in Figure 4.2.5.

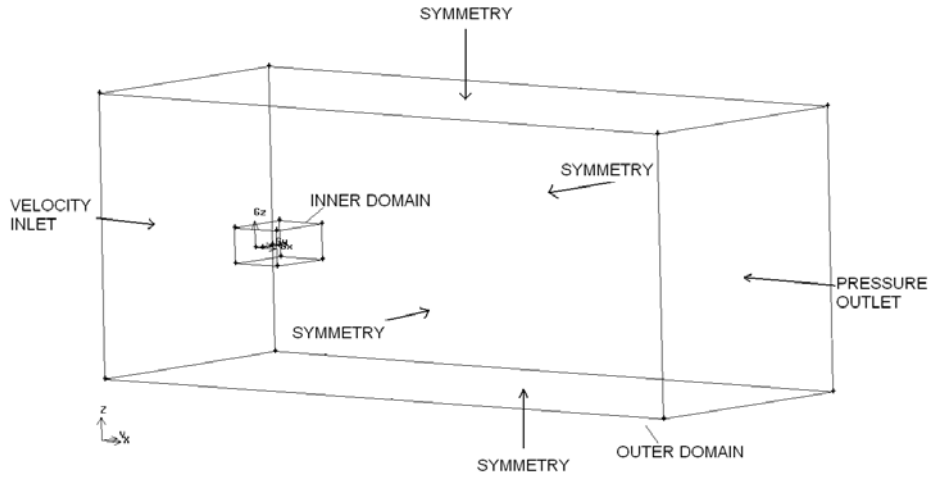

Figure 4.2.5: Solution Domain Boundary Condition Zones

4.3 3D CFD Analysis

ANSYS®/FLUENT is used to model the incompressible flow and some parameters are selected as follows;

1. ANSYS®/FLUENT 3d is selected as a solution type.
2. Pressure based solution is selected with node based gradient option.
3. Spalart-Allmaras model is chosen for viscous condition and air is selected as the fluid with the specific properties. (Density=1.225 [kg/m^3], Viscosity= 1.7894E-05 [kg/m-s]).
4. 101325 [Pa] is used as gauge pressure at pressure outlet zone.
5. Solution is established at M=0.1 (34 [m/s]) and the angle of attack (α) of 0.
6. Velocity inlet is defined for the initialization.
7. Convergence criterion is selected as 1.E-06 to monitor the residuals.

4.4 Models used in 3D CFD Analysis and Analysis Results

First, the analyses are performed with the wing without camber change having NACA4412 (Δte=0.0c) profile. The results are presented as static pressure [Pa] contour plots for the upper and lower surface in Figure 4.4.1 and Figure 4.4.2 respectively.

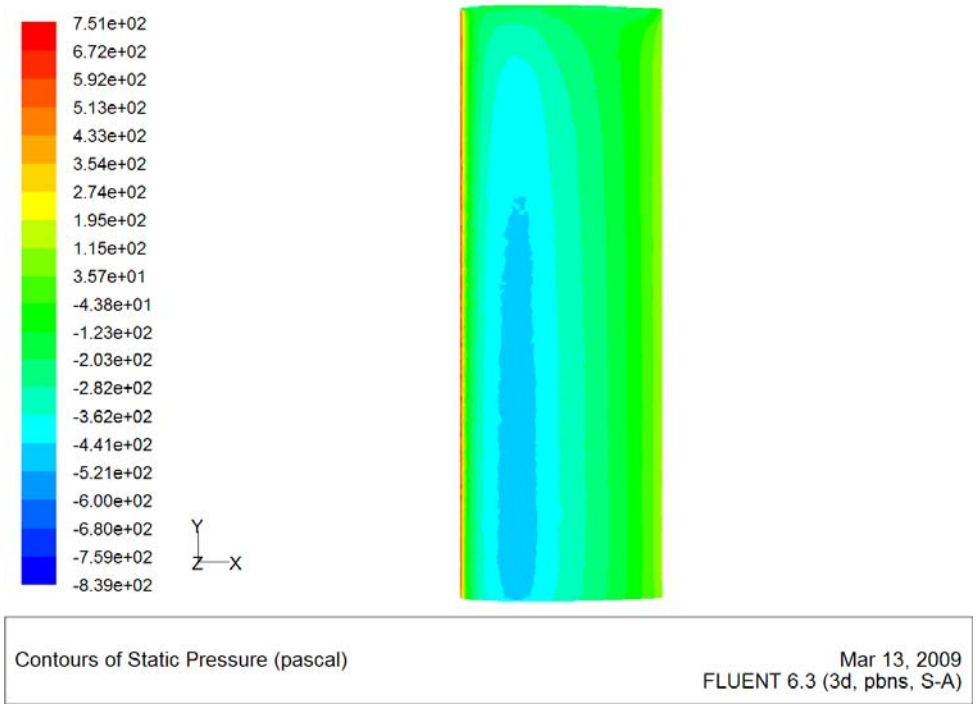

Figure 4.4.1: Upper Surface Static Pressure Contours [Pa] (Δte=0.0c)

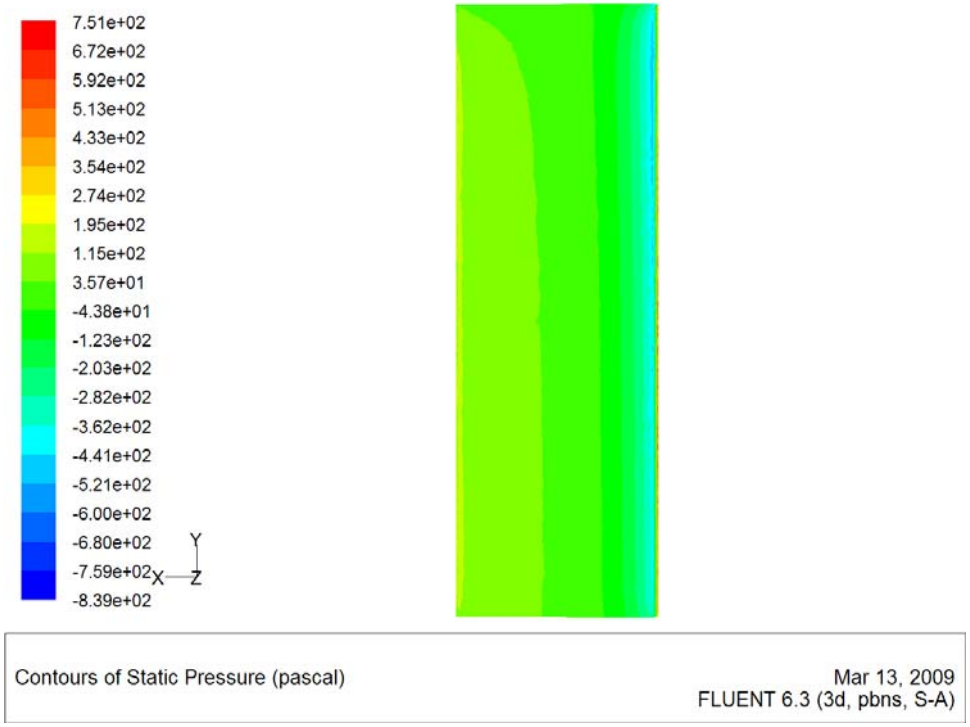

Figure 4.4.2: Lower Surface Static Pressure Contours [Pa] (Δte=0.0c)

The pressure distribution on the upper and the lower surfaces can be seen clearly in Figure 4.4.1 and Figure 4.4.2. The red contour in the leading edge is the highest pressure value in the wing. The chordwise and spanwise pressure distribution can also clearly be identified on the plot.

The second model is the wing profile with increased camber (Δte=-0.06c) where the wing camber changes in every section of the span. The results are presented as static pressure [Pa] contour plots for the upper and lower surface in Figure 4.4.3 and Figure 4.4.4 respectively.

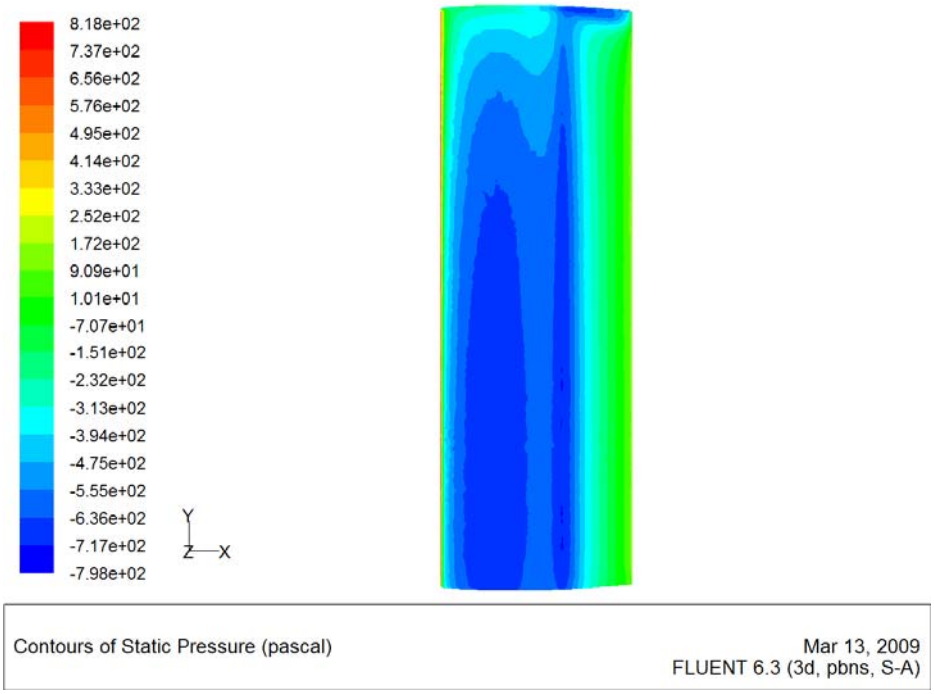

Figure 4.4.3: Upper Surface Static Pressure Contours [Pa] (Δte=-0.06c)

As it can be seen from the Figure 4.4.3, there is an increase in the pressure value on the leading edge comparing with the wing without camber change. The absolute pressure drop (suction) starts at the section where the camber increase takes place due to the changing the direction of flow. In the wing tip, the flow coming from the lower surface disturbs the flow on the upper surface.

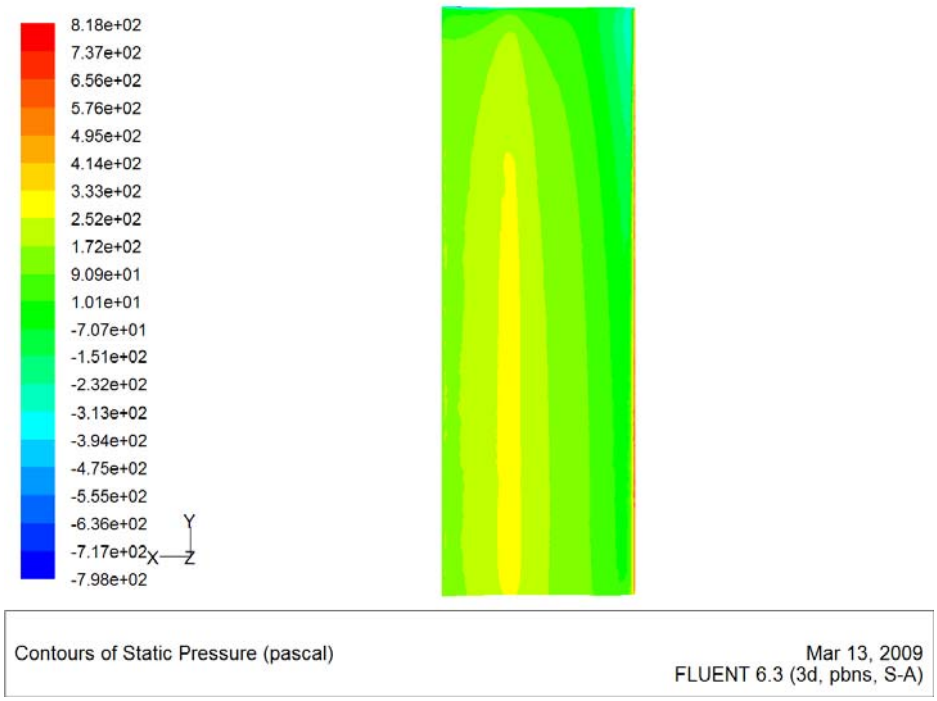

Figure 4.4.4: Lower Surface Static Pressure Contours [Pa] (Δte=-0.06c)

The chordwise and pressure change due to camber increase can clearly be seen in the contour plot of lower surface. The increase in absolute pressure value in the section where camber increase takes place is clear from the Figure 4.4.4. The flow slows down on that section resulting as a pressure increase in the section.

The third model is the wing having deflected sections through the span. The deflected sections which behave like control surfaces have increased camber (Δte=-0.06c). The outer part can be considered as aileron and the inner part behave like a flap. Detailed view of the wing is presented in Figure 4.4.5. The results for the wing having deflected control surfaces are presented as static pressure [Pa] contour plots for the upper and lower surface in Figure 4.4.6 and Figure 4.4.7 respectively.

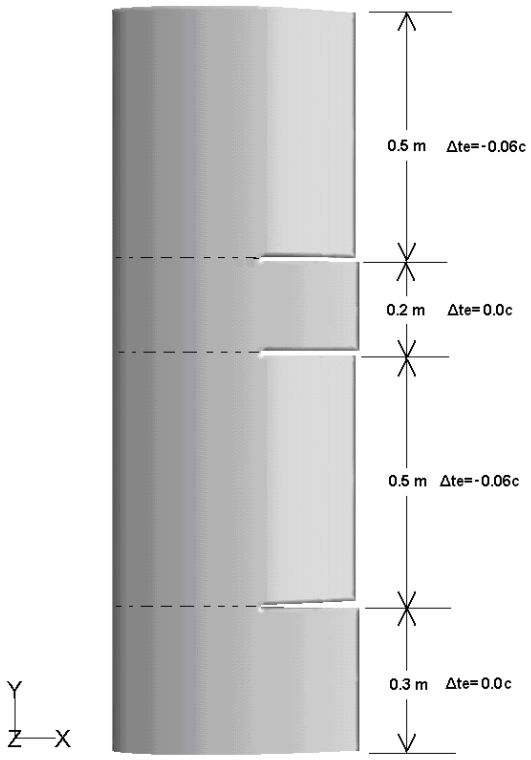

Figure 4.4.5: The Wing Model Having Deflected Control Surfaces (Δte=-0.06c)

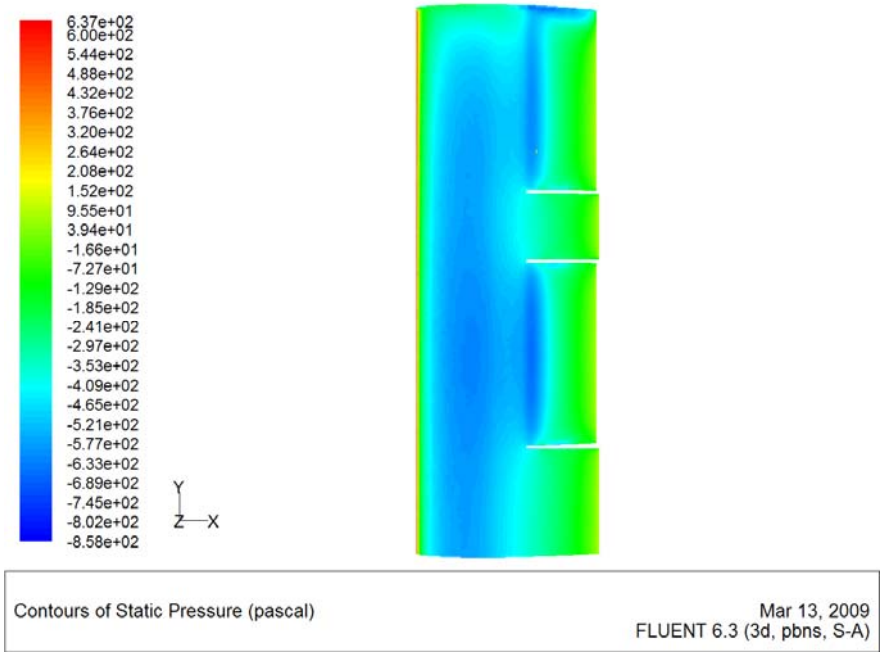

Figure 4.4.6: Upper Surface Static Pressure Contours [Pa] (with Control Surfaces)

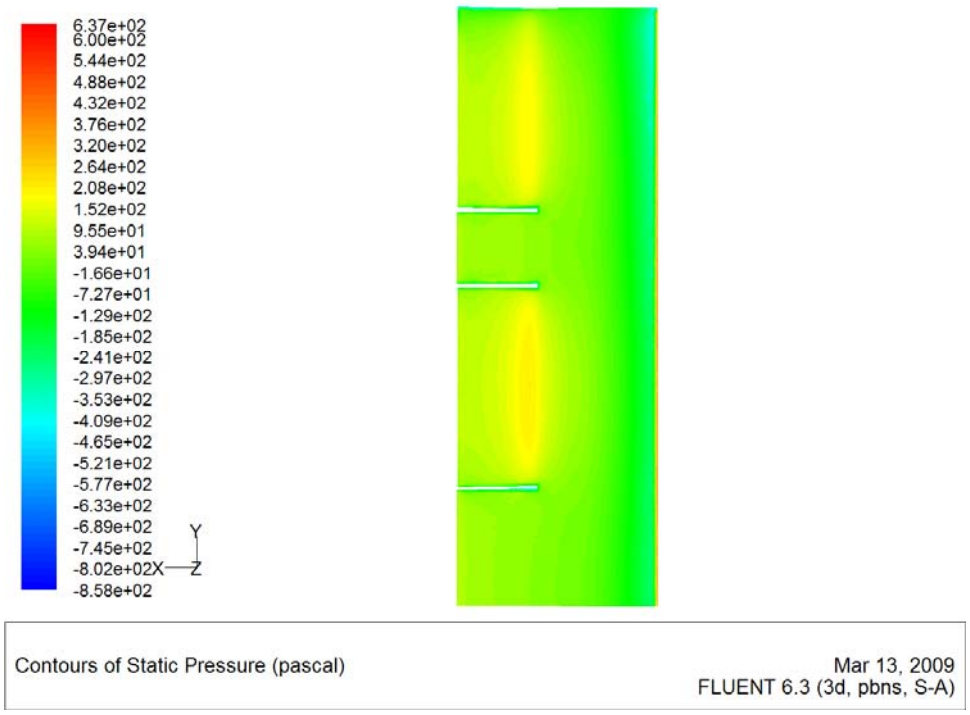

Figure 4.4.7: Lower Surface Static Pressure Contours [Pa] (with Control Surfaces)

The decrease in pressure value due to the increased flow velocity where the increased cambers take place can be seen clearly from the Figure 4.4.6. This changes the spanwise pressure distribution at the control surface sections. The increase or decrease in lift can be obtained in the specific sections so that the control of an UAV with this wing can be performed by using the control surfaces as flap or aileron. The increase in pressure value due to the decreased flow velocity where the camber increase takes place can be seen from Figure 4.4.7. The flow tends to stagnate at these sections.

As the behavior of the fluid particles passing through these sections is very important, the path lines on the section where the deflection starts at the inner control surface is presented in Figure 4.4.8. Vortex generation occurs in the region between the sections with and without camber change.

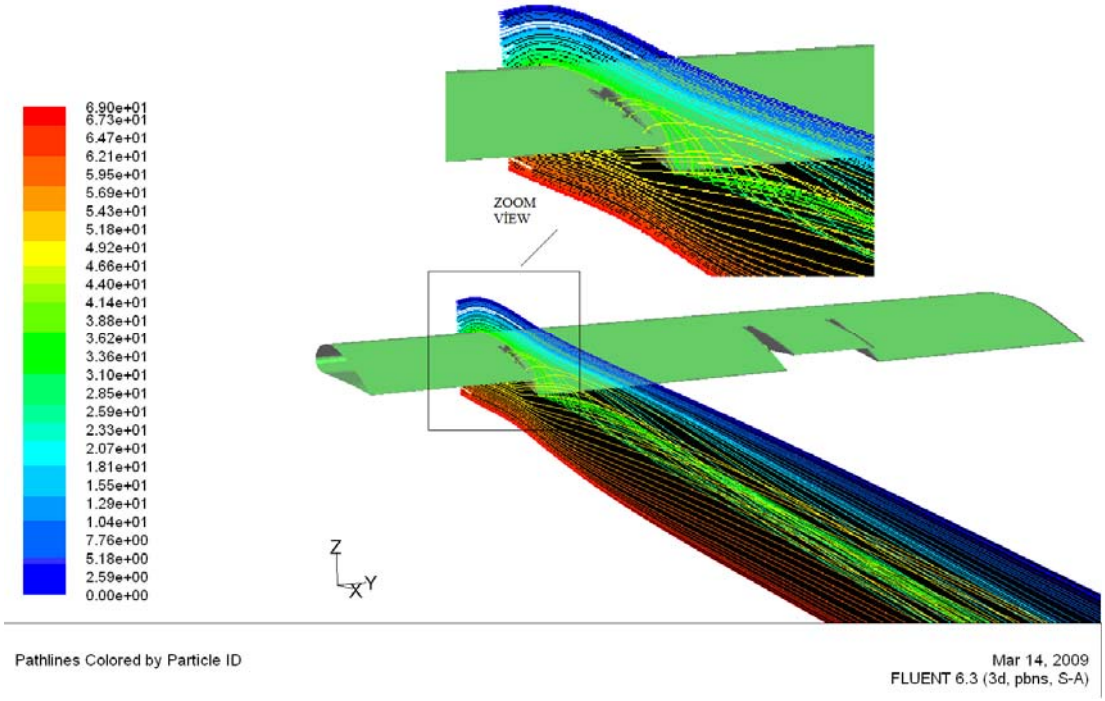

Figure 4.4.8: Control Surface Path Lines

The final model is the wing having one control surface deflected and the other twisted. The inner control surface which behaves like a flap is deflected Δte=-0.06c and outer control surface which behaves like aileron is twisted. The twist model is generated by using Δte=0.0c airfoil section for the inner edge and Δte=-0.06c for the outer edge of the aileron like control surface. Generation of surfaces enables a twisted control surface and the isometric view and the view from trailing edge of that model are presented in Figure 4.4.9 and Figure 4.4.10 respectively.

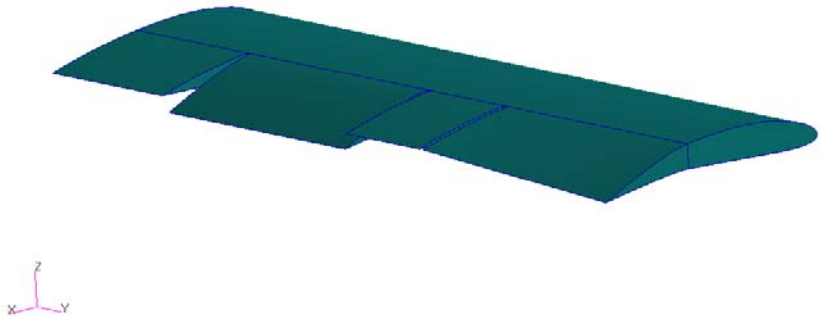

Figure 4.4.9: Isometric View of the Model of the Wing with Twisted Outer Control Surface

Figure 4.4.10: View from Trailing Edge of the Model of the Wing with Twisted Outer Control Surface

This model was generated to examine the twist effect on the static pressure values on the wing surfaces. Static pressure values are presented as a contour plot for the upper and lower surface of the wing in Figure 4.4.11 and Figure 4.4.12 respectively.

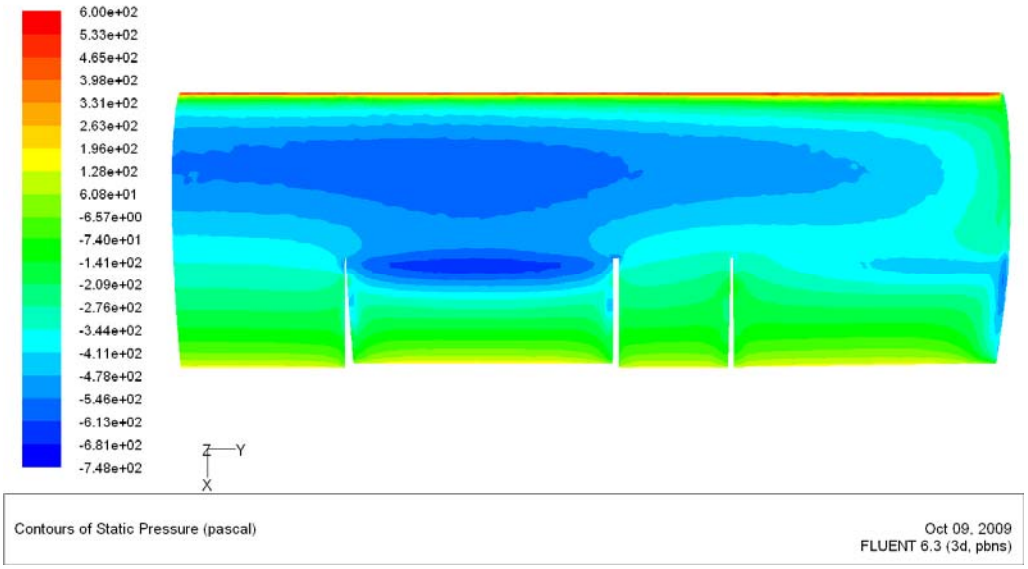

Figure 4.4.11: Pressure on the Upper Surface of the Wing with Twisted Outer Control Surface [Pa]

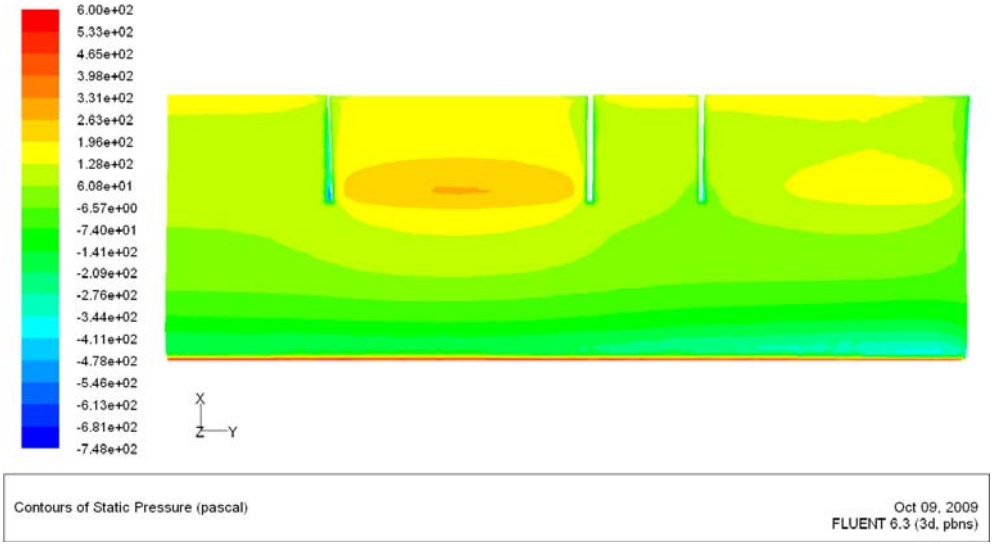

Figure 4.4.12: Pressure on the Lower Surface of the Wing with Twisted Outer Control Surface [Pa]

3D CFD analyses show that the decreasing pressure values are obtained at the tip of changing camber regions of the twisted control surface because of the increment in the flow velocity. It can be observed that the change in the camber is increasing towards the tip of the wing on the outer control surface because of the twist. Due to

increasing flow velocity, caused by the increasing camber, pressure is decreased on this surface. On the lower surface, pressure is increased at the tip of the camber change regions because of the decreasing flow velocity for the twisted control surface. At the outer control surface, where the twisting occurs, the camber is increasing towards the tip. As a result, flow velocity is decreasing towards the inner edges of the outer control surface.

4.5 Conclusion

3D CFD analysis concludes that the camber change is an effective method of changing the pressure distribution on plan-form of the wing. Due to the sectional camber change, the wing gains controllability. The study also validates the amount of trailing edge deflection is also important to have a desired lift distribution. It is possible to have twisted control surfaces if the structural restrictions can be overcome. The sectional camber change also enables the desired pressure distribution on the wing which can result in sectional lift increase or decrease. As a result, the adaptive wing concept is performed by the camber changes in the control surfaces.

CHAPTER 5

STRUCTURAL MODELING AND ANALYSIS OF MISSION ADAPTIVE WING

5.1 Introduction

In this part of the study a simplified version of the mission adaptive wing will be structurally modeled regarding the most complex model that is defined in the referred thesis [21]. The modeled wing will be used in the UAV modeling and analysis. Structural analysis of the wing is performed under aerodynamic forces and an aeroelastic analysis is presented in the means of determination of flutter speed after validation of simplified model by comparing the modal analysis result of the actual wing.

5.2 Structural Modeling of the Wing

The geometric parameters, ribs, servo ribs, spars and control surface alignments in the wing skin are presented in Figure 5.2.1. The given dimensions are in meters. Isometric view of the wing and the inner structure consisting of ribs and spars are presented in Figure 5.2.2 and Figure 5.2.3 respectively. As the leading edge of the control surfaces is open section, a structural part called ‘wedge’ is used to connect the upper and lower surface of the control surfaces. The wedge is connected to servos by a pin which controls the deflection mechanism. Detailed isometric view of the control surface [23] is presented in Figure 5.2.4.

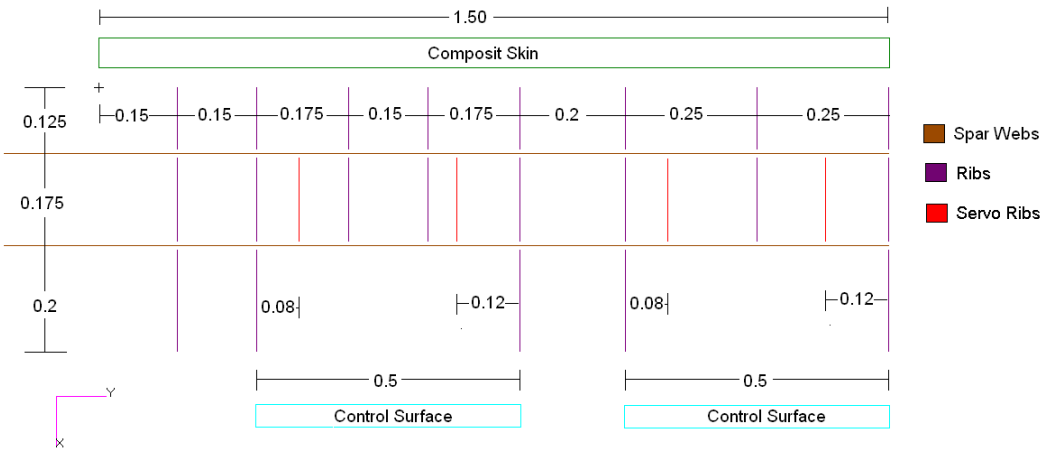

Figure 5.2.1: Geometric Presentation of the Wing [m]

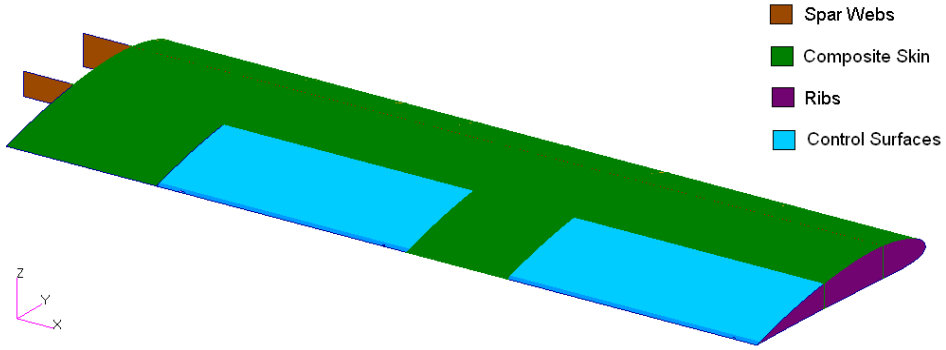

Figure 5.2.2: Isometric View of the Wing

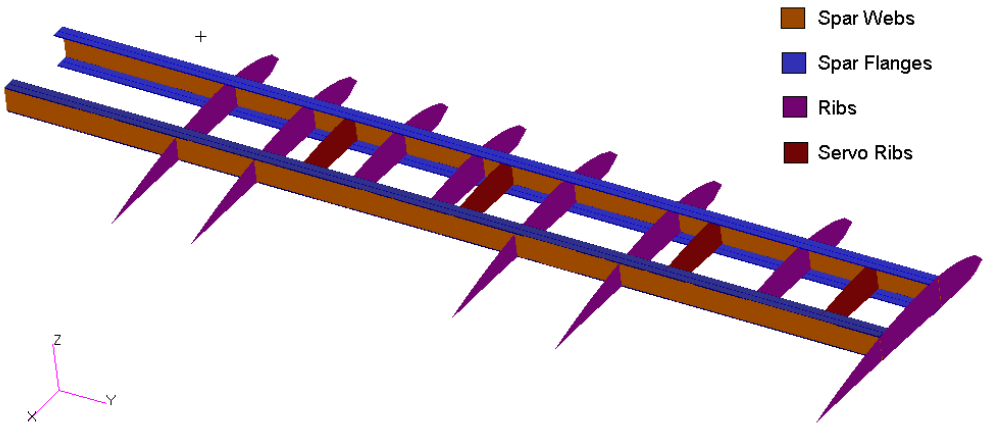

Figure 5.2.3: Isometric View of the Inner Structure

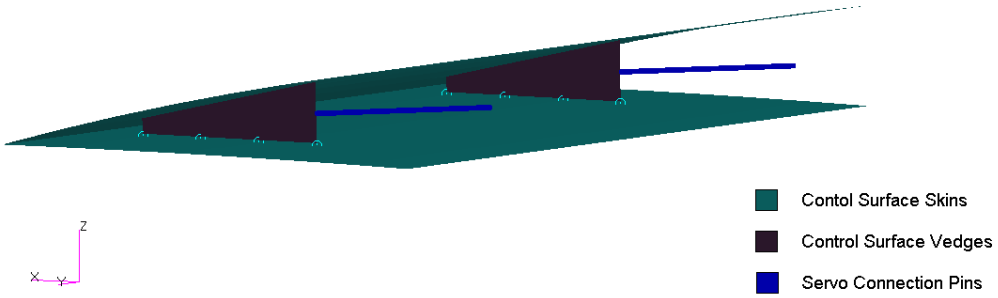

Figure 5.2.4: Isometric View of One of the Control Surfaces

Materials and their sectional properties of structural parts of the wing are presented in Table 5.2.1. Mechanical properties of isotropic materials, Aluminum 2024-T3 and Aluminum 7075-T652, used in the Finite element model is presented in Table 5.2.2 and Table 5.2.3 respectively. Finally, the corrected mechanical and physical properties [21] of composite material are presented in Table 5.2.4.

Table 5.2.1**:** Summary of the Property Sets Used in the Finite Element Model

Element Property	**Material**	**Thickness or Cross-sectional Area**
Spar Webs	Aluminum 7075-T652	2.54 [mm]
Spar Flanges	Aluminum 7075-T652	65 [mm^2]
Ribs	Aluminum 2024-T3	0.8 [mm]
Servo Ribs	4 Layer Laminated Composite	1.50 [mm]
Control Surfaces	Aluminum 2024-T3	0.635 [mm]
Control Surface Vedge	Aluminum 7075-T652	2 [mm]
Composite Skin	4 Layer Laminated Composite	1.50 [mm]
Servo Connection Pins	Aluminum 7075-T652	3.14 [mm^2]

Table 5.2.2: Physical and Mechanical Properties of Aluminum 2024-T3 Material Selected for the Ribs Control Surface [21]

Density	2780 [kg/m^3]
Young's Modulus, E	73.1 [GPa]
Shear Modulus, G	28.0 [GPa]
Poison's Raito, ν	0.33
Ultimate Strength	483 [MPa]
Yield Strength	385 [MPa]
Shear Strength	283 [MPa]

Table 5.2.3**:** Physical and Mechanical Properties of Aluminum 7075-T652 Material Selected for the Spar Webs and Flanges [21]

Density	2810 [kg/m^3]
Young's Modulus, E	71.7 [GPa]
Shear Modulus, G	26.9 [GPa]
Poison's Raito, ν	0.33
Ultimate Strength	572 [MPa]
Yield Strength	503 [MPa]
Shear Strength	331 [MPa]

Table 5.2.4: Corrected 2D Orthotropic Mechanical and Physical Properties of the 7781 E-Glass Fabric – Araldite LY5052 Resin / Aradur HY5052 Hardener Laminated Composite Material [21]

Density	11513 [kg/m^3]
E_{11}	21 [GPa]
E_{22}	21.3 [GPa]
G_{12}	3.6 [GPa]
G_{13}	2.81 [GPa]
G_{23}	2.81 [GPa]

The finite element model of the wing is conducted as two separate models. The first model is the wing without control surfaces called as Wing Model 1. This model is the load carrying part of the wing which can be considered and named as the torque box of the wing. This model is for validation of the finite element model with the test wing model [21]. The second model is the wing with control surfaces named as Wing Model 2. The number and the type of the elements of models are summarized in Table 5.2.5. The Wing Model 1 is composed of 1658 grid points while the Wing Model 2 has 2264 grid points.

Table 5.2.5**:** Summary of the Element Types and Numbers in Wing Models

Element type	**Wing Model 1**	**Wing Model2**
BAR2	228	268
QUAD4	1802	2302
TRIA3	8	8
RBE2	-	16

5.3 Modal Analysis of the Wing

The modal analysis of the Wing Model 1 of the wing is conducted to validate the consistency of model with the actual wing. The aim is to have resemblance in the natural frequency results between the experimental and finite element analyses of the wing. The wing in the experiment and the finite element model generated for the modal analysis do not have control surfaces. The isometric view of the finite element model of the Wing Model 1 is presented in Figure 5.3.1 while the boundary condition is given in Figure 5.3.2. The wing is fixed at the presented nodes in all 6 Degree of Freedom.

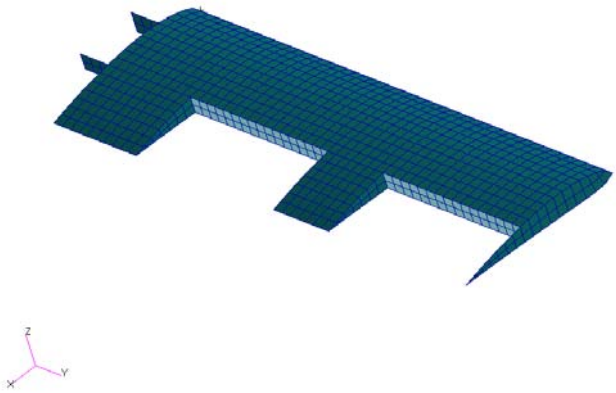

Figure 5.3.1**:** Isometric View of One of Finite Element Model of Wing Model 1

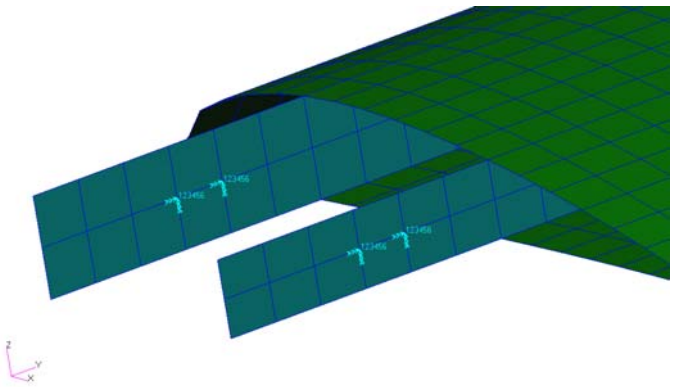

Figure 5.3.2**:** Fix Boundary Condition of the Wing Model 1

The natural frequency results of the related modes of the finite element model and that of experimental analysis are tabulated in Table 5.3.1. The results are within the expectable error with respect to the experimental data for the simplified model of the wing.

Table 5.3.1**:** The Natural and Resonance Frequency Results of the Finite Element Analysis of Wing Model 1 and Experimental Analysis of Wing 1 [21]

Mode Shape	**Wing Model 1 Natural Frequencies (FEM) [Hz.]**	**Wing 1 Resonance Frequencies (Experimental) [21] [Hz.]**
1. Out-of-plane Bending	14.109	14.750
1. In-plane Bending	51.498	43.500
1. Torsion	61.86	66.750
2. Out-of-plane Bending	98.883	93.000

5.4 Aeroelastic Analysis of the Wing

The structural models of the wing are then used for an aeroelastic analysis to calculate flutter speed. MSC®/FLDS [24] commercial program is used for the analysis and p-k method [25] is used as a solution method for the flutter analysis. For the analysis, an aerodynamic lifting surface must be created first. The generated aerodynamic lifting surface in the analysis is presented in Figure 5.4.1. The Wing Model 1 and the corresponding lifting surface are presented together as an illustration in Figure 5.4.2.

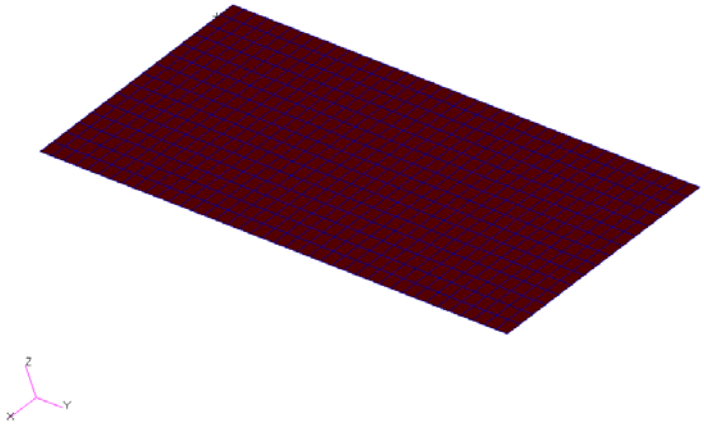

Figure 5.4.1: Isometric View of the Lifting Surface Used in the Analysis

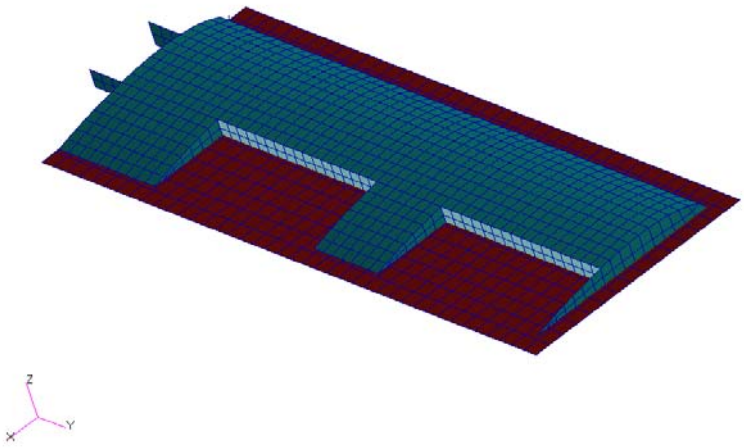

Figure 5.4.2**:** Isometric View of the Lifting Surface and Wing Model 1 used in the Analysis

The next step is to generate spline between the aerodynamic lifting surface elements and the structural model elements to generate the whole aero-structural model [24]. The grid points used for generating spline for Wing Model 1 and Wing Model 2 are presented in Figure 5.4.3 and Figure 5.4.4 respectively.

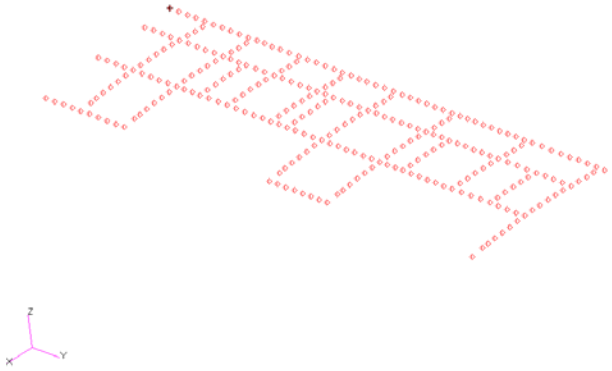

Figure 5.4.3: Grid Points Used to Generate Spline for Wing Model 1

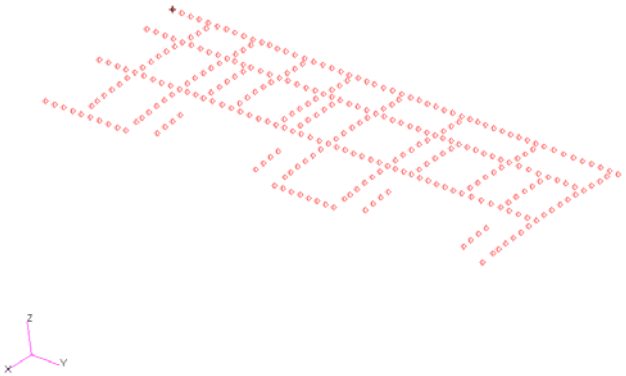

Figure 5.4.4**:** Grid Points Used to Generate Spline for Wing Model 2

The only difference between these two models is the added wedge nodes to create spline at the locations where the control surfaces are.

For the analysis, density ratio sets in Table 5.4.1 and the velocity sets in Table 5.4.2 are used to create subcases. Vel_1, Vel_2, and Vel_3 velocity sets are used to examine the results in specific domains corresponding to velocity intervals. Vel_f velocity set is used to finalize the analysis and to obtain the final result.

Table 5.4.1: Density Ratio Set

Set Name	Altitude [m]	Density ratio*
Dens	Sea level	1

*Density ratio is ratio of the density of air in the flight altitude to the density of air at sea level.

Table 5.4.2**:** Velocity Sets [m/s]

Vel_1	Vel_2	Vel_3	Vel_f
10	80	180	10
20	90	190	30
30	100	200	50
40	110	210	70
50	120	220	100
60	130	230	130
70	140	240	160
80	150	250	190
90	160	260	220
100	170	270	250
	180	280	
	200	300	

For the analysis, Mach-reduced frequency (M-k) sets are created. The Mach number, minimum frequency value which must be less than the first out-of-plane bending frequency, maximum frequency which is higher than the first torsional frequency and minimum and maximum velocities are the parameters used to generate reduced frequency values. The estimated cruise velocity of the UAV is 18-21 [m/s] and maximum velocity is 36-39 [m/s]. First M-k set is generated with the Mach number of 0.2 which is approximately twice as the maximum velocity of the UAV. The first analysis is performed with the M-k sets generated for Mach number of 0.2 to have an idea of the actual flutter speed and the corresponding Mach value at this speed of the wing. The first sets used in the analysis for Wing Model 1 and Wing Model 2 are tabulated in Table 5.4.3.

Table 5.4.3: M-k Set $_1$ Used in the Analysis of Wing Model 1 and Wing Model 2

	Wing Model 1	**Wing Model 2**
Mach Number	0.2	0.2
Fmin [Hz]	13	12
Fmax [Hz]	63	66
Vmin [m/s]	10	10
Vmax [m/s]	100	100
Reduced frequency, k	0.204;1.282;2.359;3.436; 4.513;5.591;6.668;7.745; 8.823; 9.900	0.189;1.320;2.451;3.583 4.714;5.846;6.977;8.109 9.240;10.371

The analysis results are presented with damping vs. velocity and frequency vs. velocity graphs. The result for the M-k set$_1$ which is the initial result to have an idea for the Mach number value where flutter is possible to occur. Then the second M-k set is created according to the Mach number value where the aeroelastic instability occurs found from the analysis using M-k set$_1$.

The velocity value where the damping vs. velocity curve is passing from negative value to a positive value is considered as the flutter speed and the velocity value where frequency drops to zero is considered as the divergence speed. The modes found are the related aeroelastic modes where these instabilities take place.

The result for the initial analysis for the Wing Model 1 is presented in Figure 5.4.5. From this figure, it can be seen that the flutter tends to happen at a velocity corresponding a Mach number value of 0.6. This result leads us to perform the analysis again at the mode accurate Mach number value which gives a better convergence and the mode shapes for these instabilities.

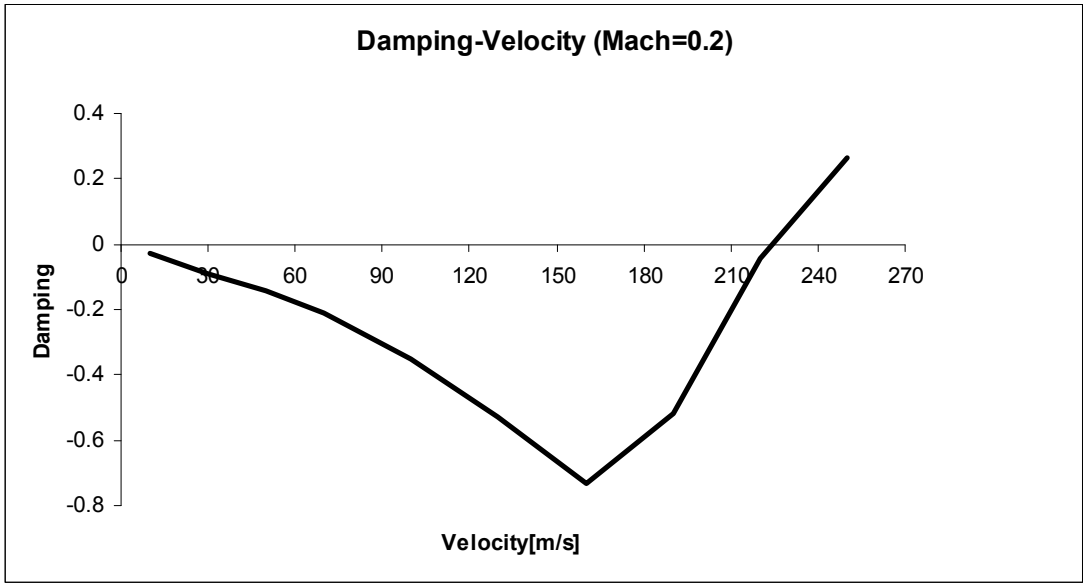

Figure 5.4.5**:** Damping vs. Velocity Graph (M=0.2) for Wing Model 1

The next analysis is performed with Wing Model 2 where the control surfaces are also modeled together with the wing torque box. The initial analysis results are presented as damping vs. velocity curve in Figure 5.4.6 and it indicates that the instability takes place at a velocity value corresponding to a Mach number of 0.5.

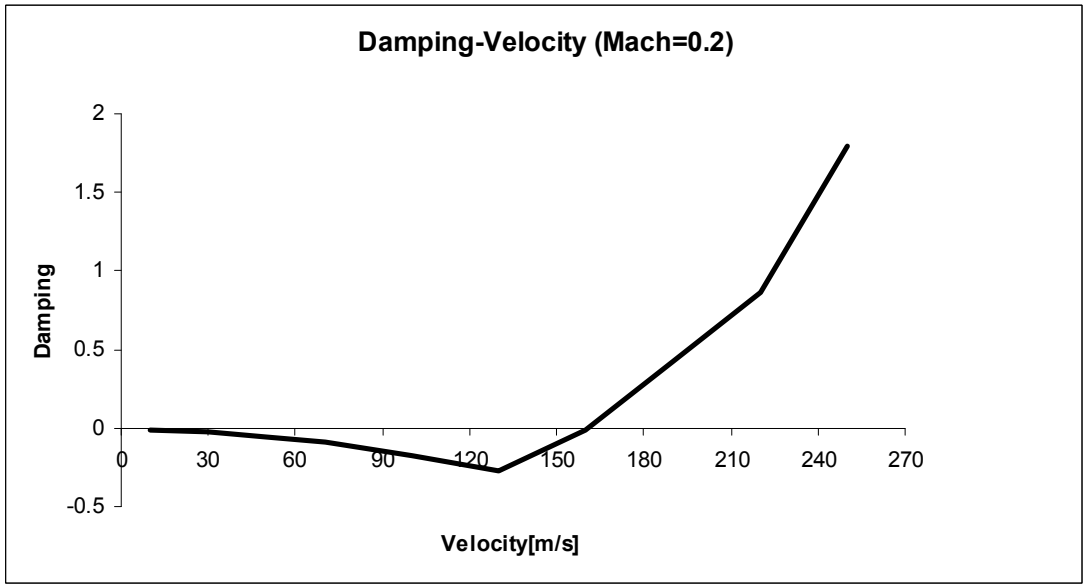

Figure 5.4.6: Damping vs. Velocity Graph (M=0.2) for Wing Model 2

The second M-k sets are created with the Mach value found in the first analysis to have a better convergence at the actual flutter or divergence speed. The analysis is performed again with the new M-k set. The second sets used in the analysis for Wing Model 1 and Wing Model 2 are tabulated in Table 5.4.4.

Table 5.4.4**:** M-k Set $_2$ Used in the Analysis of Wing Model 1 and Wing Model 2

	Wing Model 1	**Wing Model 2**
Mach Number	0.6	0.5
Fmin [Hz]	13	12
Fmax [Hz]	63	66
Vmin [m/s]	10	10
Vmax [m/s]	100	100
Reduced frequency, k	0.204;1.282;2.359;3.436; 4.513;5.591;6.668;7.745; 8.823; 9.900	0.189;1.320;2.451;3.583 4.714;5.846;6.977;8.109 9.240;10.371

The next and the final M-k Set is created for the Wing Model 1 at the Mach number of 0.6. Figure 5.4.7 presents the damping vs. velocity graph at M=0.6. The flutter speed is determined about 200 [m/s].

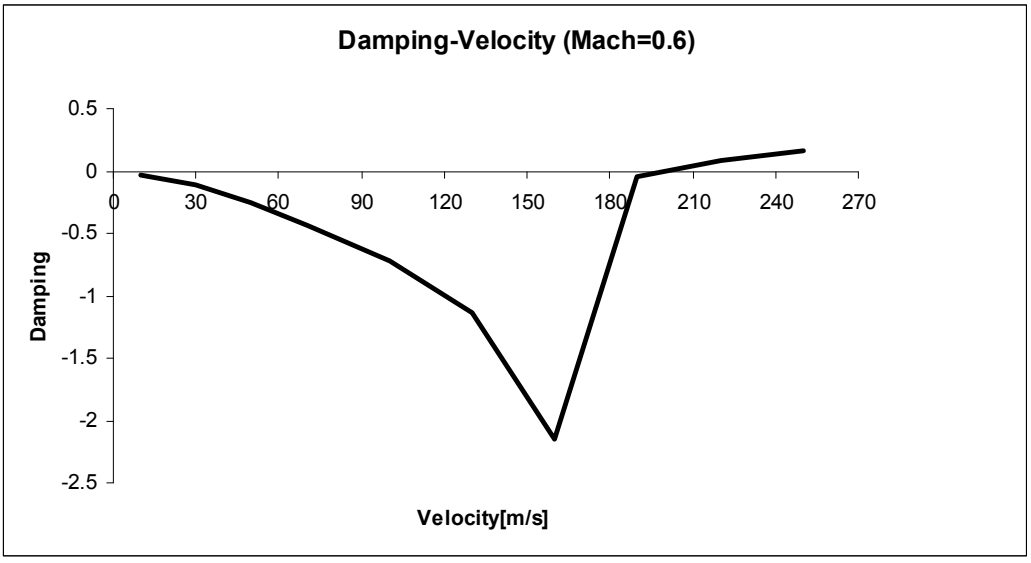

Figure 5.4.7**:** Damping vs. Velocity Graph (M=0.6) for Wing Model 1

The frequency vs. velocity curve is presented in Figure 5.4.8 and it shows that the divergence occurs just below the value of flutter speed. As a result, the instability for Wing Model 1 is due to divergence at a speed of about 195 [m/s].

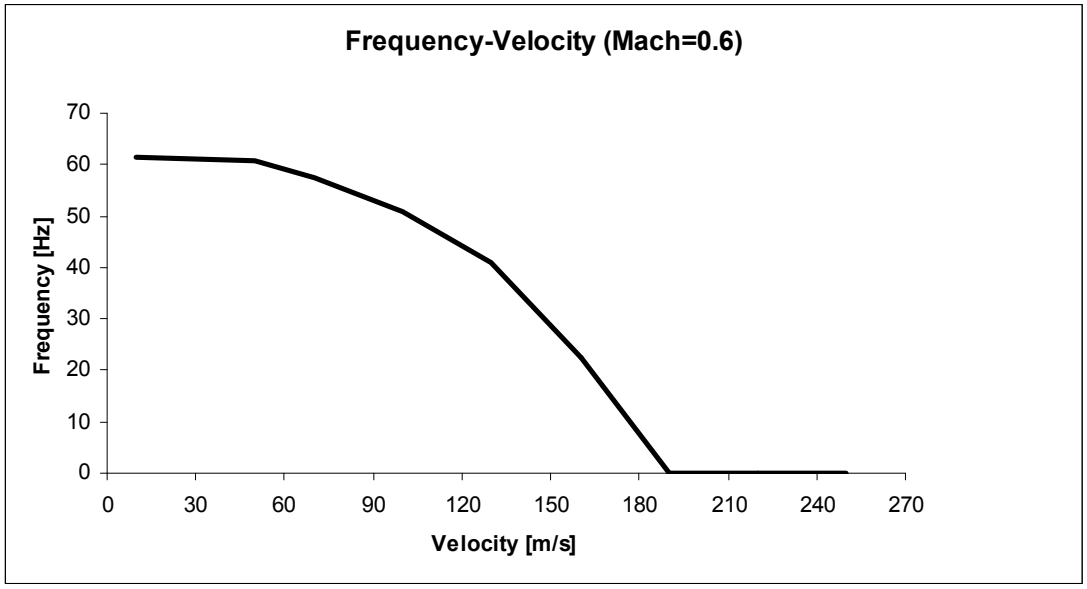

Figure 5.4.8**:** Frequency vs. Velocity Graph (M=0.6) for Wing Model 1

The next and the final M-k Set is created for Wing Model 2 at the Mach number of 0.5. Figure 5.4.9 presents the damping vs. velocity graph at M=0.5. The flutter speed is about 160 [m/s].

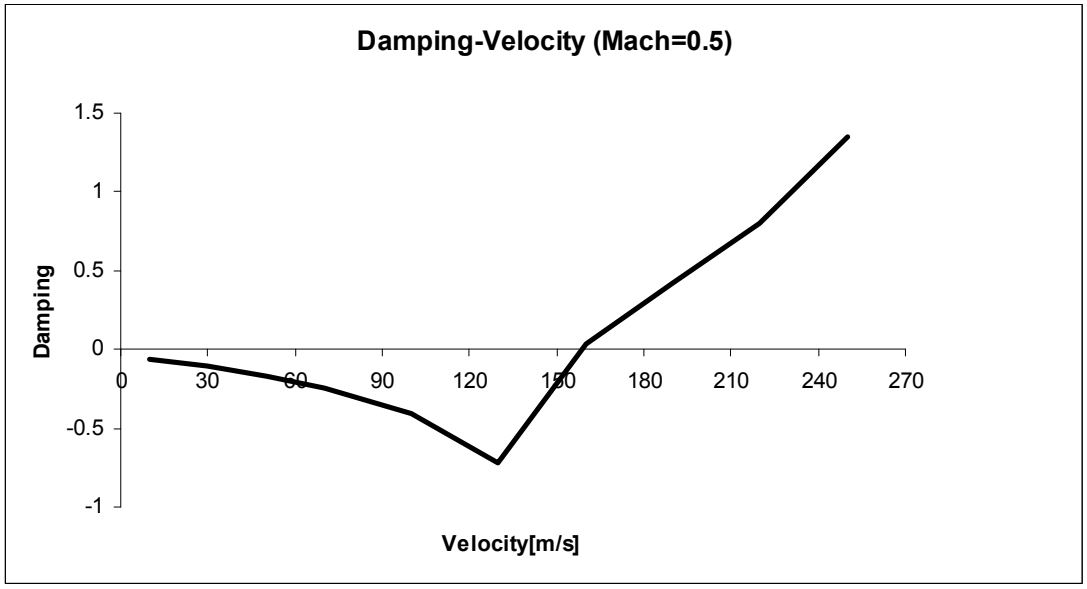

Figure 5.4.9**:** Damping vs. Velocity Graph (M=0.5) for Wing Model 2

The frequency vs. velocity graph presented in Figure 5.4.10 shows that divergence occurs above the value of flutter speed at about 190 [m/s]. As a result, the instability for model 2 is due to the flutter at a speed of about 160 [m/s].

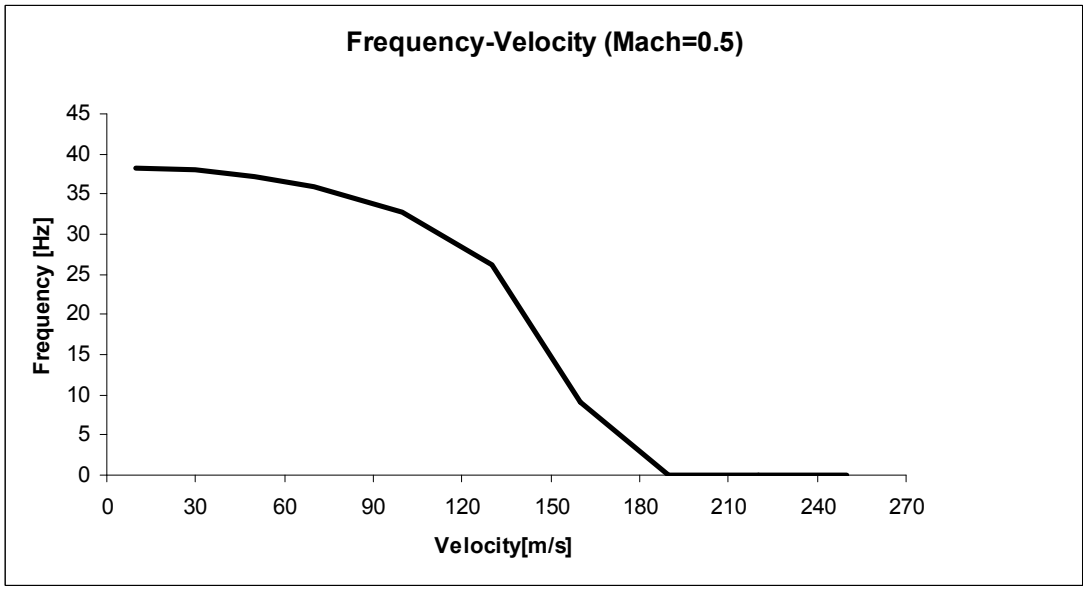

Figure 5.4.10: Frequency vs. Velocity Graph (M=0.5) for Wing Model 2

The instability speed is lower in Wing Model 2 than the one in Wing Model 1. This phenomenon occurs because of the control surfaces which have less stiffness with respect to the other structural parts of the wing. The local modes on the control surfaces result in a lower instability speed. Increasing the stiffness of the control surfaces will result in a higher instability speed [26] with a price of a decrease in maximum deflection capability of control surfaces.

5.5 Static Analysis of the Wing

For the static analysis, the wing with control surfaces (Wing Model 2) will be analyzed under the pressure field generated in the 3D Aerodynamic Analysis chapter. The model is performed by using MSC®/PATRAN. First, the pressure boundary condition is generated. Then, the mesh on the surface of the wing where the analysis results is interpolated using ANSYS®/FLUENT is created before importing the pressure loads to the model. The mesh on the wing is presented Figure 5.5.1.

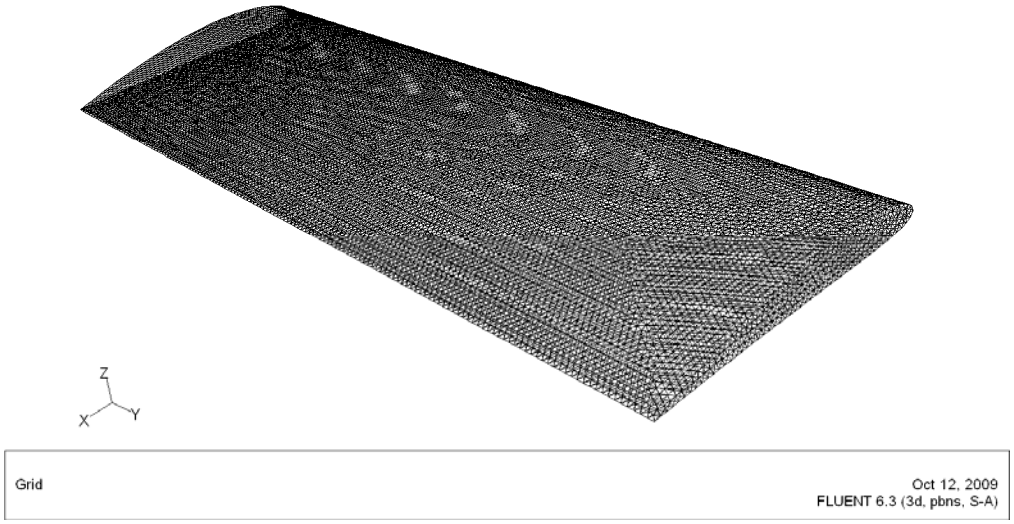

Figure 5.5.1: CFD Mesh on the Wing Surfaces

The static pressure values are imported to MSC®/PATRAN as an input via this CFD mesh. The static pressure values on the CFD mesh is used to generate the pressure field on the skin of the structural model of the wing which is shown in Figure 5.5.2.

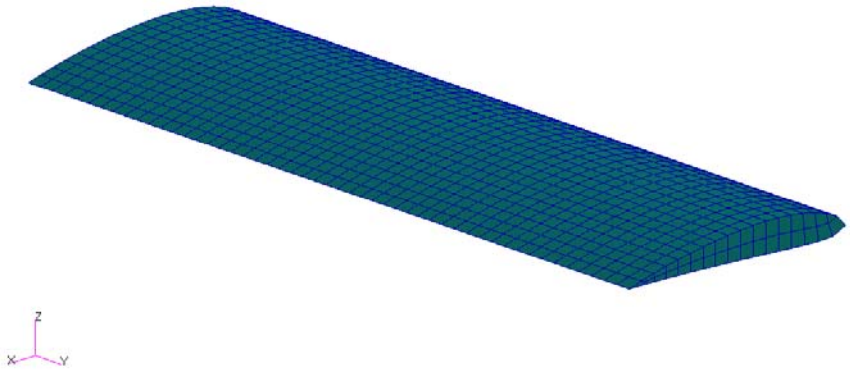

Figure 5.5.2: Structural Model Mesh on the Wing Surfaces

The CFD analysis result for Δte=-0.06c deflection of both control surfaces is used as the static pressure value input. The pressure distribution is presented on the CFD mesh in MSC®/PATRAN as the static pressure contours for the upper and lower surface in Figure 5.5.3 and Figure 5.5.4 respectively.

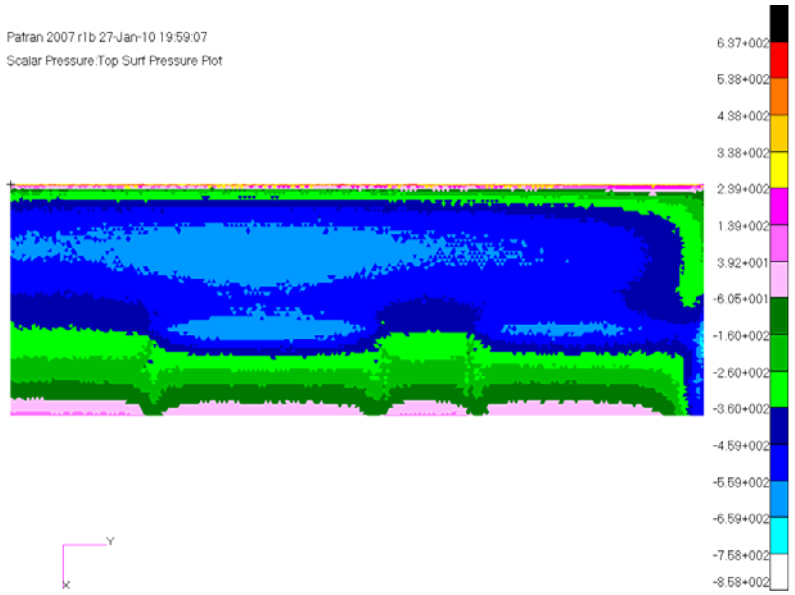

Figure 5.5.3: Imported Upper Skin Static Pressure Contour on CFD Mesh [Pa]

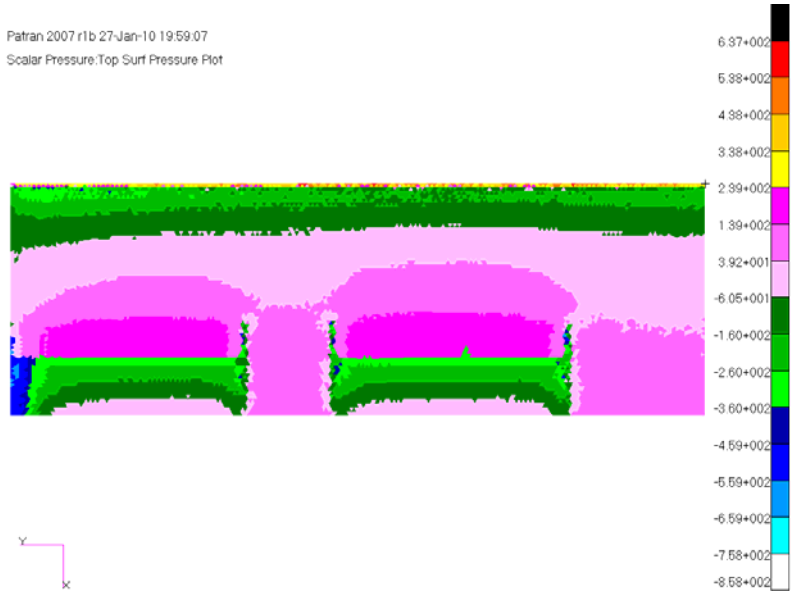

Figure 5.5.4**:** Imported Lower Skin Static Pressure Contour on CFD Mesh [Pa]

As the mesh on the wing surfaces of structural Model is different than the CFD mesh, the static pressure values must be integrated into the structural mesh. A pressure field is generated using the CFD mesh and interpolated on the surfaces of the wing in the structural model mesh by assigning the values to the closest nodes. This process finalizes the generation of pressure boundary condition for the static

analysis. The interpolated pressure values on the structural model mesh is presented as static pressure contours for the upper and lower skin in Figure 5.5.5 and Figure 5.5.6 respectively.

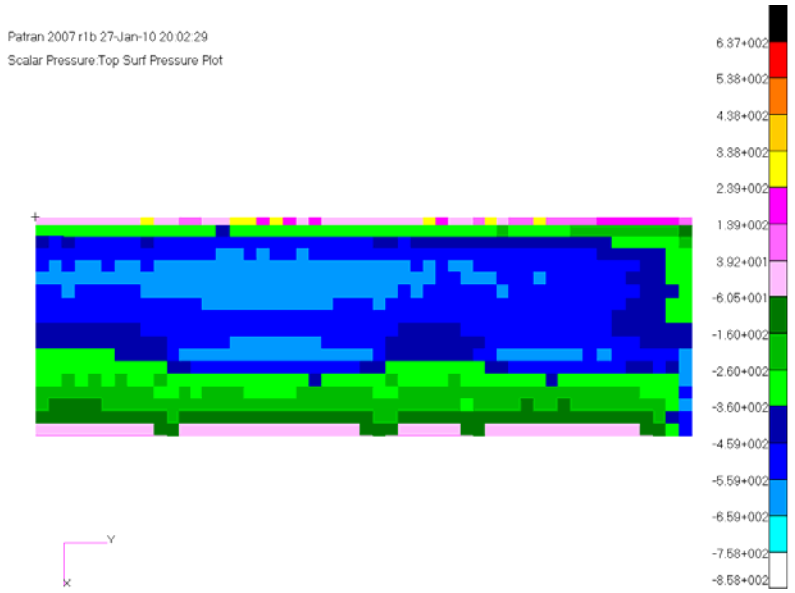

Figure 5.5.5: Interpolated Upper Skin Static Pressure Contour on Structural Model Mesh [Pa]

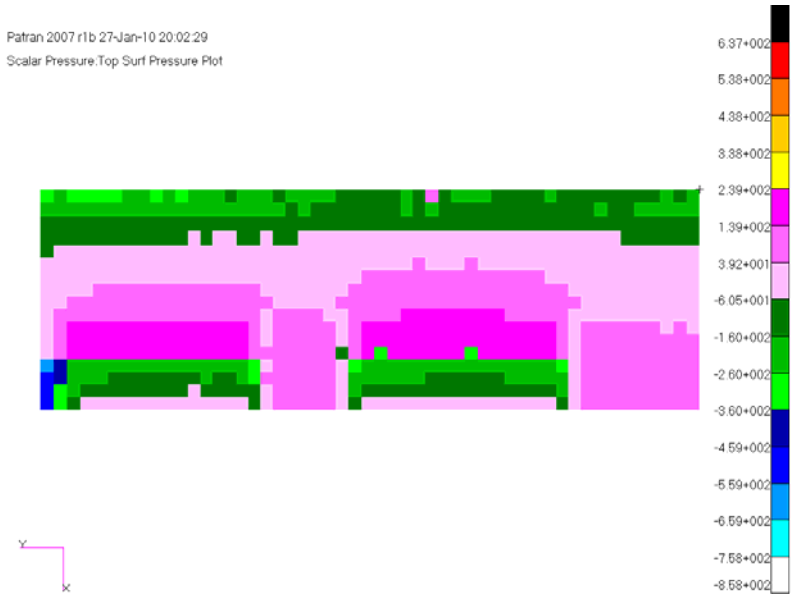

Figure 5.5.6**:** Interpolated Lower Skin Static Pressure Contour on Structural Model Mesh [Pa]

After the generation of pressure boundary condition the wing is fixed from its spar webs as using the same boundary conditions used in the modal analysis and then the static analysis is performed. The result is given as displacements of the wing in model scale to have a better visualization on the displacement of control surfaces and in true scale to observe the actual deformation in Figure 5.5.7 and Figure 5.5.8 respectively.

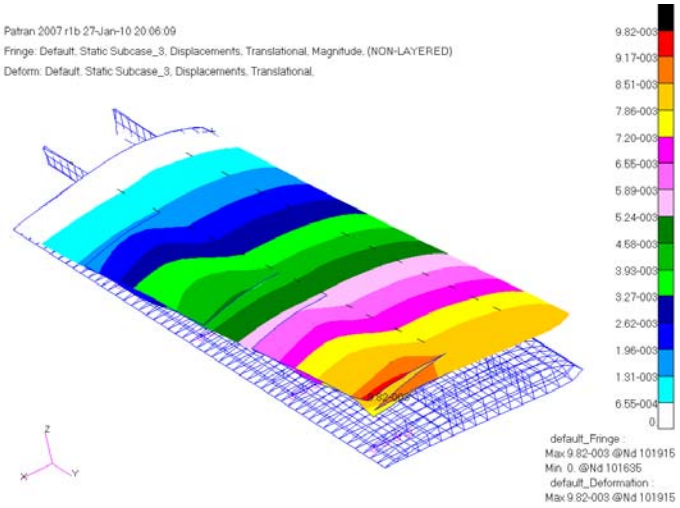

Figure 5.5.7: Displacement of the Wing in Model Scale [m]

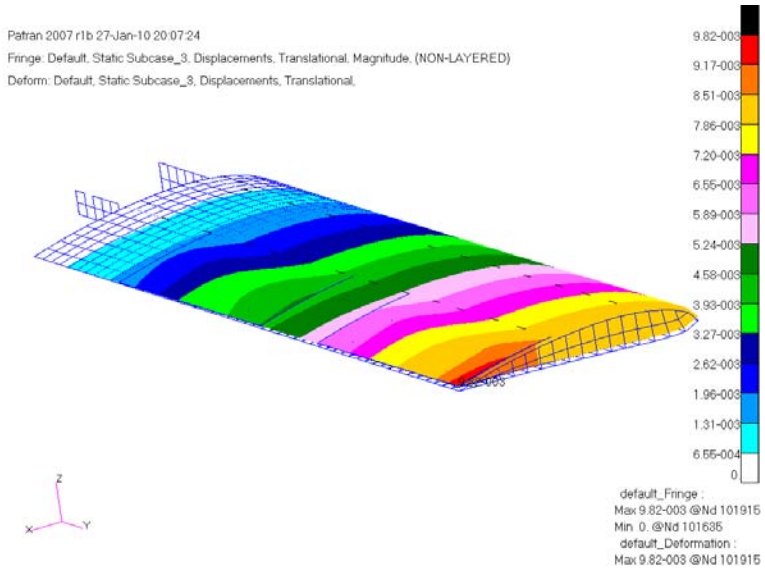

Figure 5.5.8: Displacement of the Wing in True Scale [m]

5.6 Conclusion

Considering the estimated approximate cruise velocity of the UAV as 18-21 [m/s] and maximum velocity as 36-39 [m/s], the wing of the aerial vehicle is safe from the aeroelastic instability point of view. The static analysis also concludes that the maximum deflection of the wing is about 1 [cm] on the outer control surface under the pressure load at 34 [m/s]. The displacements of control surfaces are quite important as unwanted/uncontrolled displacements may result in having different cambered shapes than the desired one.

CHAPTER 6

STRUCTURAL MODELING AND ANALYSIS OF UNMANNED AERIAL VEHICLE

6.1 Introduction

This chapter is about the structural design and modeling of the UAV comprising two main parts, namely the fuselage and the empennage. It also involves assembly of the mission adaptive wings to obtain a complete structural model of the UAV in MSC®/PATRAN by using FEM technique. Additionally, the developed model will be subjected to static and dynamic loads and the related analyses will be performed in this chapter. Finally, the manufacture of the fuselage and the empennage is detailed by explaining the assembly procedure.

6.2 Design of the UAV

The fuselage and the empennage dimensions are decided by using flight mechanics concepts and by also considering the engine and the payload dimensions. The most important design criterion of the fuselage is building it structurally strong enough to carry the payloads and having enough room considering the geometric dimensions of the payloads. The empennage dimensions, chord lengths and tapers forming plan-form areas of vertical and horizontal tail including rudder, elevator and the moment arm of the tail is also decided using flight mechanics concepts considering the mission profile of the UAV. The isometric view of the designed unmanned aerial vehicle having mission adaptive wings is given in Figure 6.2.1. The top and the side

views are also shown with their dimensions in Figure 6.2.2 and Figure 6.2.3 respectively.

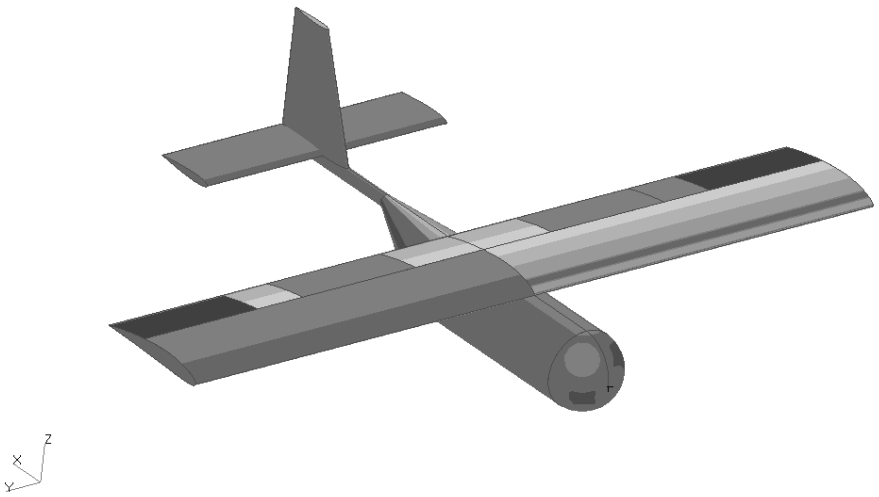

Figure 6.2.1: Isometric View of the UAV with Mission Adaptive Wings

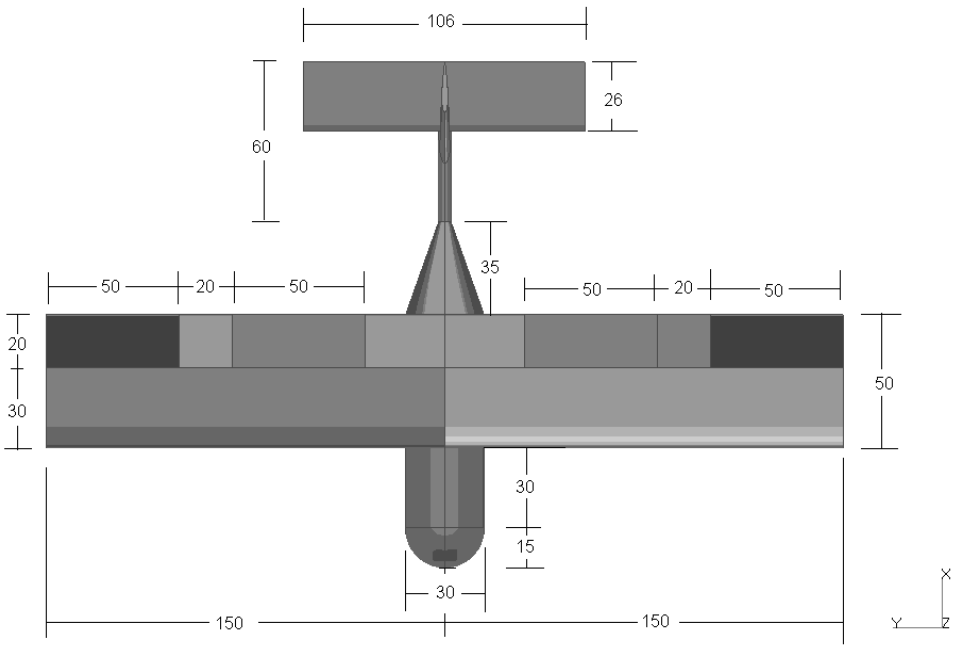

Figure 6.2.2: Top View of the UAV with Mission Adaptive Wings [cm]

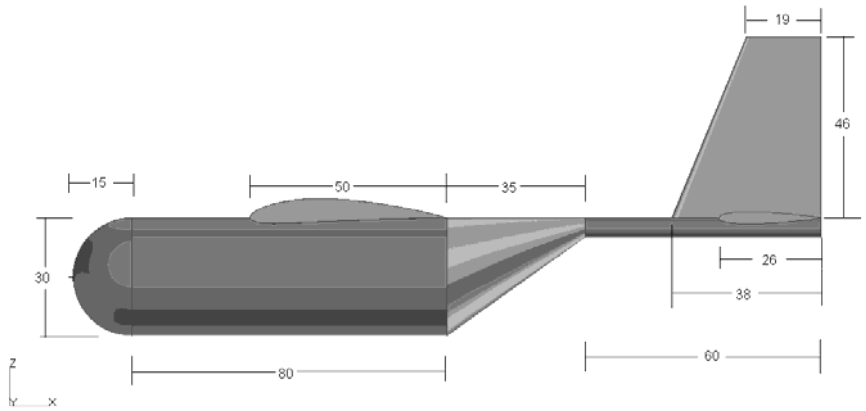

Figure 6.2.3: Side View of the UAV with Mission Adaptive Wings [cm]

The fuselage of the UAV is composed of nose, longerons, frames, equipment raft and composite skin while the empennage consists of tail boom, conical segment, horizontal and vertical tail. The wing model is the one modeled as mission adaptive wing with control surfaces (Wing Model 2) in chapter 5. The material selection for the UAV is performed considering the availability of the materials for the manufacturing process. Materials and their sectional properties of the structural parts of the fuselage and the empennage are presented in Table 6.2.1. Physical and mechanical properties of isotropic materials, Aluminum 6061-T4, Aluminum 6061-T6 and Aluminum 7075-T652 are tabulated in Table 6.2.2 where Table 6.2.3 presents that of the other materials such as Steel AISI 1005, Balsa Wood and Foam. The laminated composite is the same material used in the modeling of the mission adaptive wing.

Table 6.2.1: Summary of the Property Sets

Element Property	Material	Thickness/Cross Sectional Area
Longerons	Aluminum 7075-T652	1.65 [mm]
Frames	Aluminum 6061-T4	2.032 [mm]
Equipment Raft	6 Layer Laminated Composite	2.25 [mm]
Nose	4 Layer Laminated Composite	1.50 [mm]
Tail Boom	Aluminum 6061-T6	0.8 [mm]
Tail Conical Segment	6 Layer Laminated Composite	2.25 [mm]
Horizontal Tail Skin	6 Layer Laminated Composite	2.25 [mm]
Horizontal Tail Spar	Balsa Wood	5.00 [mm]
Horizontal Tail Inner Volume	Foam	as filling material
Vertical Tail Skin	4 Layer Laminated Composite	1.50 [mm]
Vertical Tail Spar	Balsa Wood	5.00 [mm]
Vertical Tail Inner Volume	Foam	as filling material
Composite Skin	4 Layer Laminated Composite	1.50 [mm]
Connection Pins	Steel AISI 1005	28.26 [mm^2]

Table 6.2.2 Physical and Mechanical Properties of Aluminum Materials

Properties	6061-T4	6061-T6	7075-T652
Density	2700 [kg/m^3]	2700 [kg/m^3]	2810 [kg/m^3]
Young's Modulus, E	68.9 [GPa]	68.9 [GPa]	71.7 [GPa]
Shear Modulus, G	26.0 [GPa]	26.0 [GPa]	26.9 [GPa]
Poison's Raito, ν	0.33	0.33	0.33
Ultimate Strength	241 [MPa]	310 [MPa]	572 [MPa]
Yield Strength	145 [MPa]	276 [MPa]	503 [MPa]
Shear Strength	165 [MPa]	207 [MPa]	331 [MPa]

Table 6.2.3**:** Physical and Mechanical Properties of Various Materials

Properties	Steel AISI 1005	Balsa Wood	Foam
Density	7872 [kg/m^3]	120 [kg/m^3]	100 [kg/m^3]
Young's Modulus, E	200 [GPa]	2 [GPa]	1 [GPa]
Shear Modulus, G	80 [GPa]	0.2 [GPa]	-
Poison's Raito, ν	0.29	-	0.2

6.3 Modeling of the Fuselage of the UAV

The fuselage consists of longerons, frames, nose, equipment raft and a composite skin. Those components are structurally designed and their finite element models are given in this section.

The four longerons used in the fuselage have L-Section profiles and manufactured from Aluminum 7075-T652 material with the thickness of 1.65 [mm]. The cross-sectional properties of the longerons are given in Figure 6.3.1.

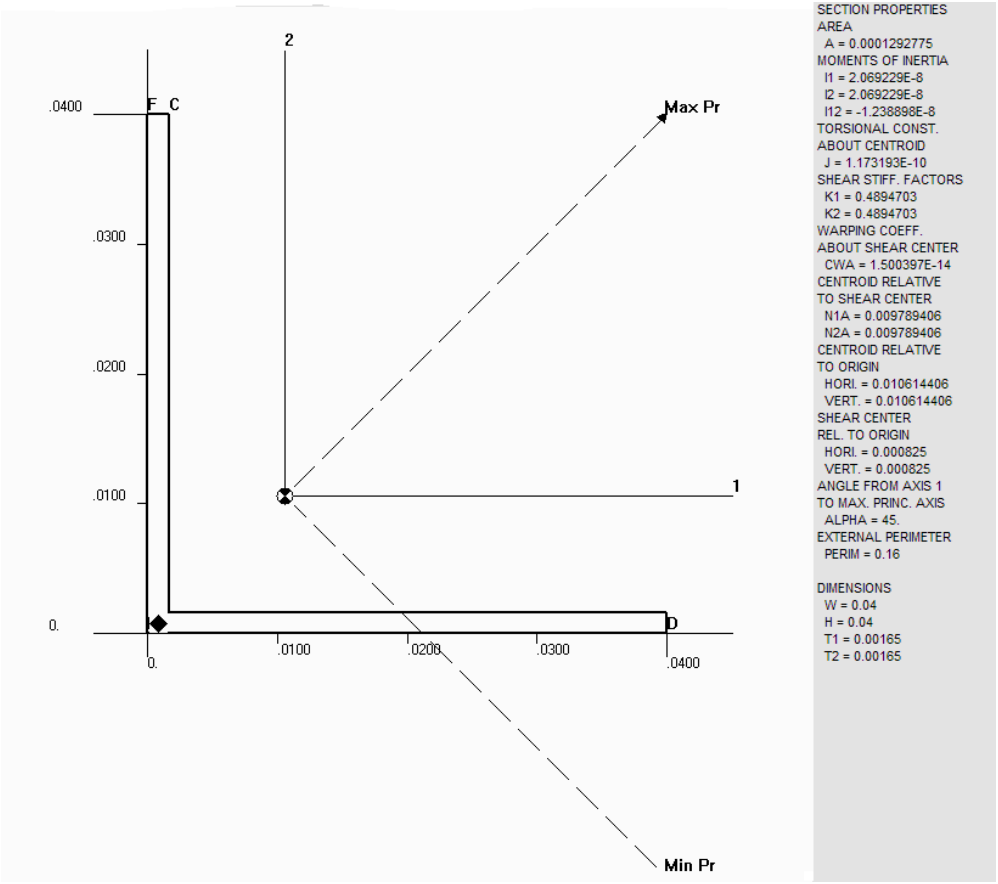

Figure 6.3.1: Sectional Properties of the Longerons

The locations of the longerons are selected in order to have easy assembly. Due to the cylindrical form of the fuselage, the longerons are placed to have a symmetric form. The locations of the longerons in the fuselage are given in Figure 6.3.2.

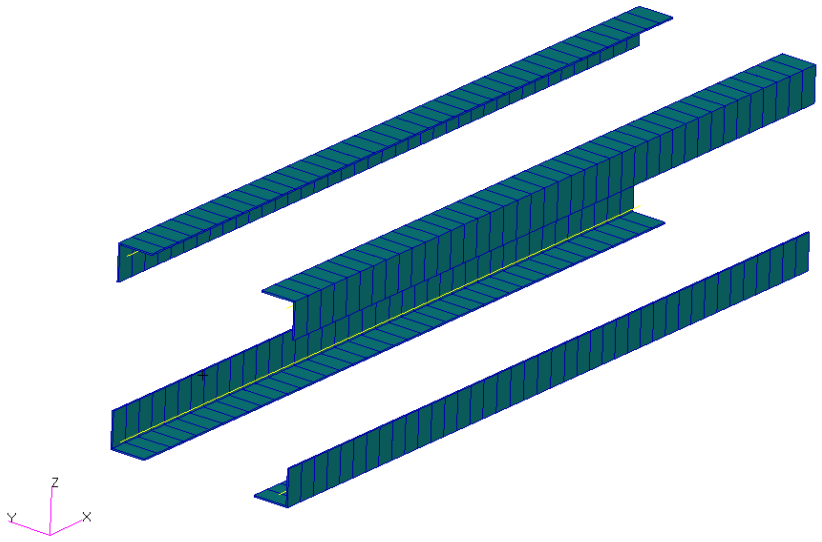

Figure 6.3.2: Placement of Longerons in the Structural Model

There are five frames used for the 80 [cm] long cylindrical fuselage segment. Figure 6.3.2 gives the frame numbers and the corresponding locations at the segment of the fuselage. The Aluminum 6061-T4 type material used for each frame has the same thickness of 2.032 [mm]. The placement of the frames is done considering the location of the wing and the fuselage to wing connection.

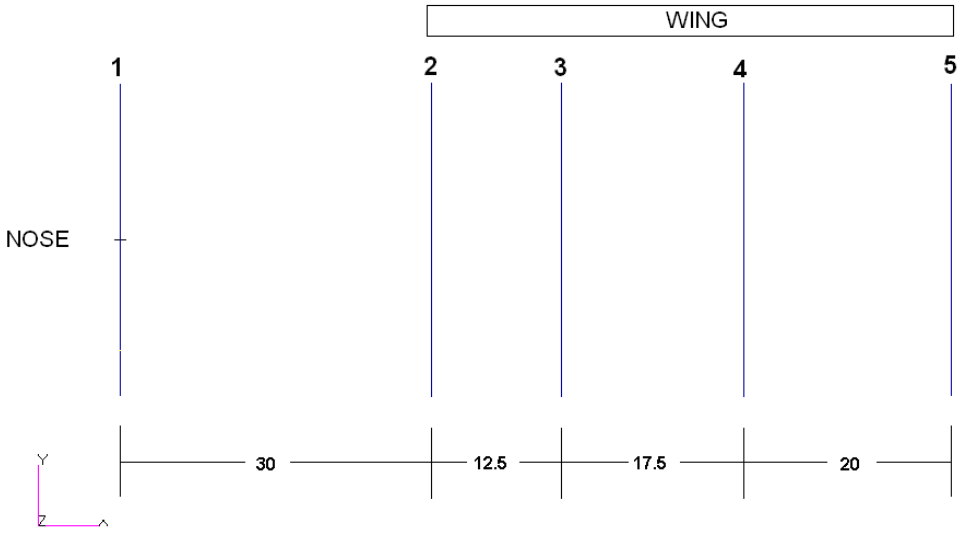

Figure 6.3.3: Alignment of the Frames in the Fuselage of the UAV [cm] (side view)

Figure 6.3.4 to Figure 6.3.8 give the CAD and the structural model of the all frames used in the fuselage of the UAV. The third and the forth frames are used for wing-fuselage assembly. The circular cut out opened at the fifth frame is for the connection of the tail boom to the fuselage internal structure.

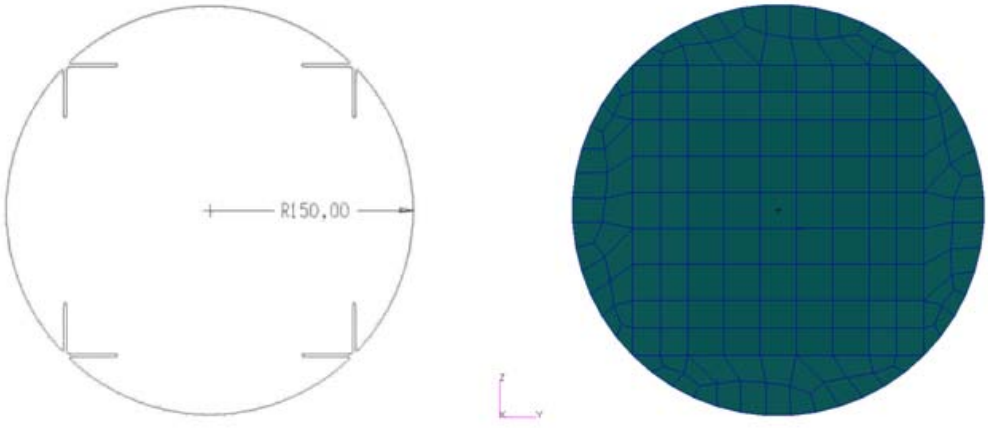

Figure 6.3.4: CAD Model and Structural Model of First Frame [mm]

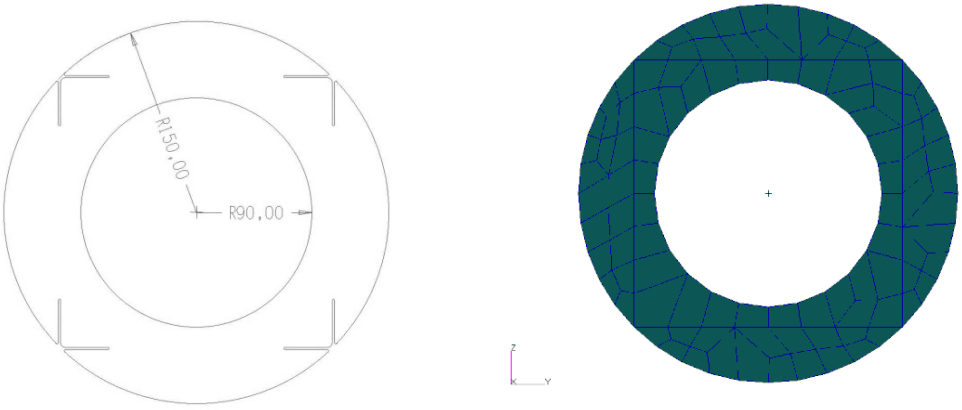

Figure 6.3.5: CAD Model and Structural Model of Second Frame [mm]

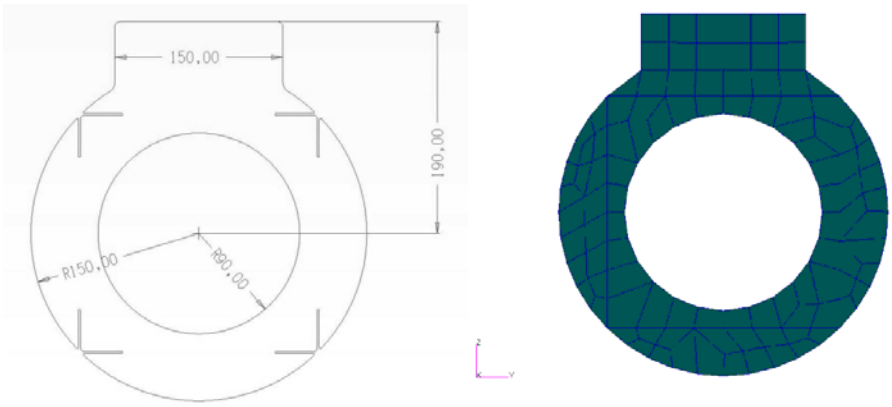

Figure 6.3.6: CAD Model and Structural Model of Third Frame [mm]

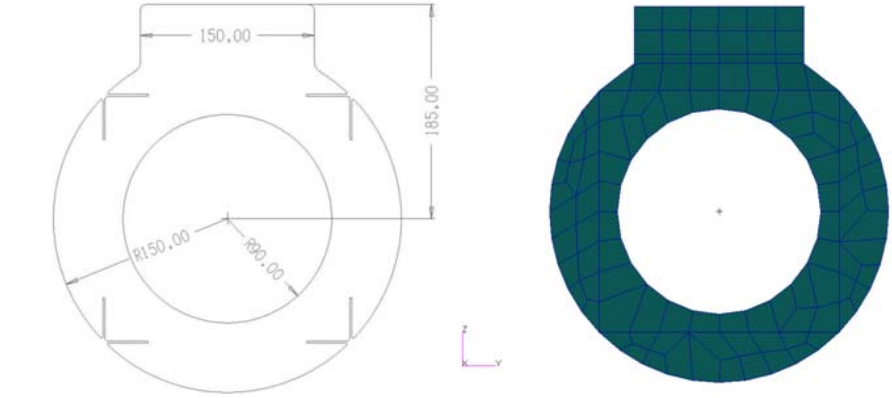

Figure 6.3.7: CAD Model and Structural Model of Fourth Frame [mm]

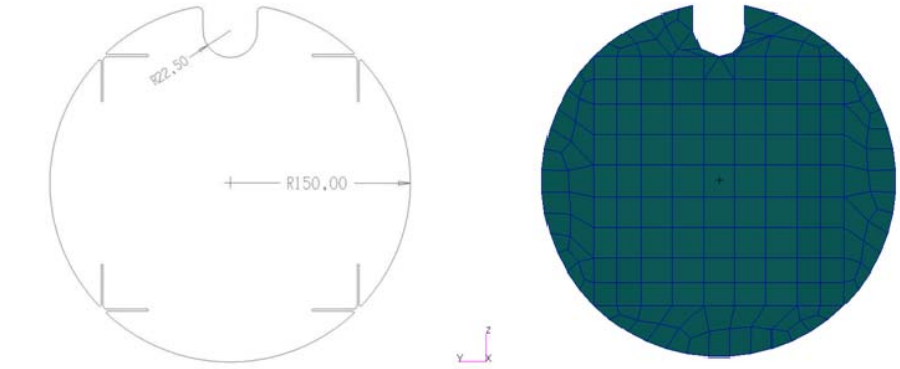

Figure 6.3.8: CAD Model and Structural Model of Fifth Frame [mm]

The frames are also designed considering the frame to longeron connections with their cutouts for the manufacturing purposes but those cut outs are not modeled in the structural models. The longeron connection cutout on the frames is presented on an arbitrary fuselage frame in Figure 6.3.9.

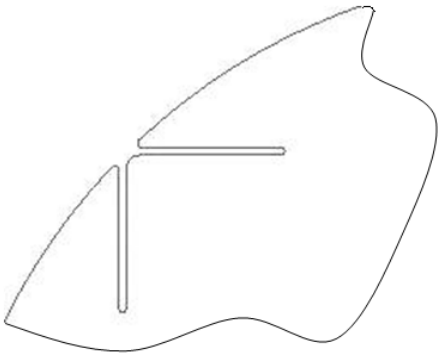

Figure 6.3.9: Longeron Connection Cutout on an arbitrary Fuselage Frame

The structural model of the equipment raft which will be assembled on the longerons is shown in Figure 6.3.10. The raft is made up of six layers of composite material with a staking sequence of $[0/90]_6$ [21].

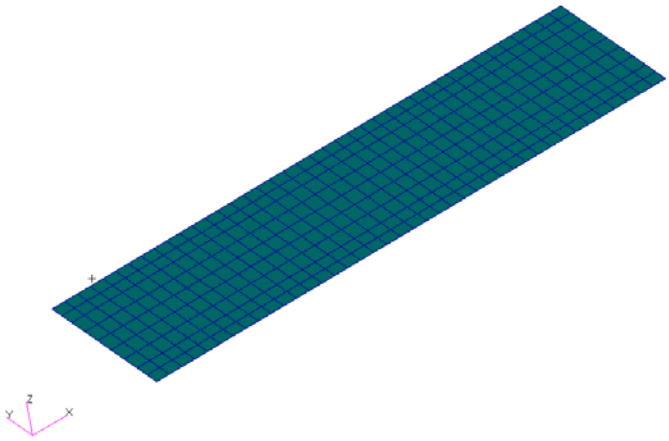

Figure 6.3.10: Structural Model of the Equipment Raft

The fuselage nose is formed of four layers of the composite material with the staking sequence of $[0/90]_4$. The structural model of the fuselage nose is shown in Figure 6.3.11.

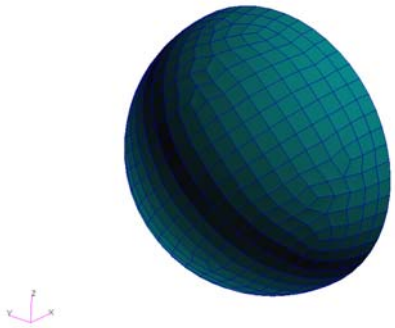

Figure 6.3.11: Structural Model of the Fuselage Nose

The skin of the cylindrical segment of the fuselage is modeled from four layers of the composite material with the staking sequence of $[0/90]_4$. The structural model is developed by eliminating the interface skin area between the fuselage and the skin of the wing. Figure 6.3.12 illustrates the structural model of the composite skin of the cylindrical segment of the fuselage.

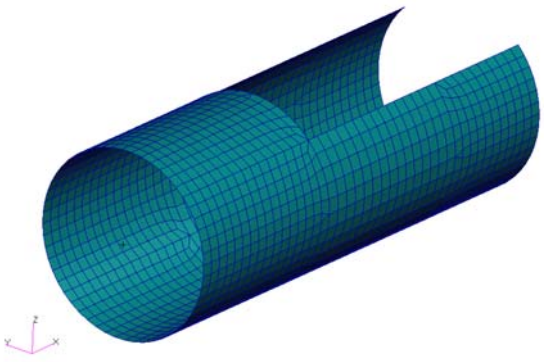

Figure 6.3.12: Structural Model of the Composite Skin

The internal structure is assembled by equivalence of nodes at the connection sections. As the longerons of the internal structure are the load carrying parts of the overall structure, they are assembled as whole and modeled with BEAM elements by assigning their cross-sectional properties. Figure 6.3.13 shows the assembled structural model of the internal structure of the fuselage. In order to locate and mount necessary peripheral equipment, a raft is designed and integrated into the internal structure of the fuselage shown in Figure 6.3.14. During the assembly the equipment raft edge nodes are equivalenced to the nodes on the longerons and the connections of the frames.

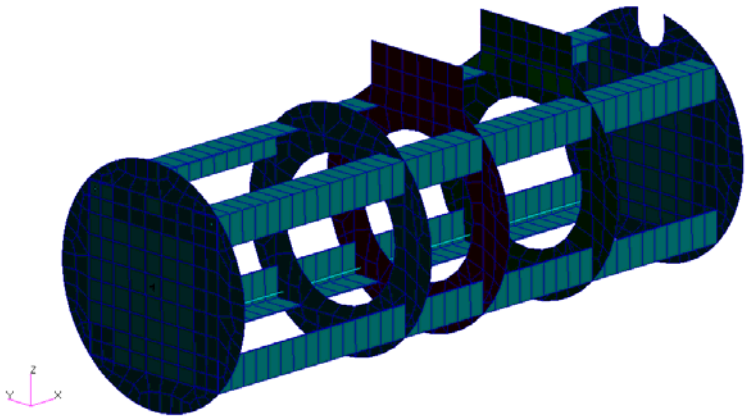

Figure 6.3.13: Structural Model of the Internal Structure

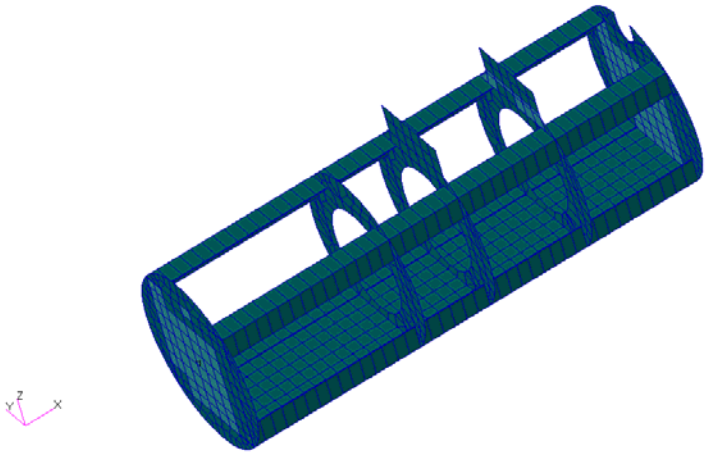

Figure 6.3.14: Structural Model of the Equipment Raft and Internal Structure Assembly

The composite skin is then assembled to the internal structure with the nose with equivalenced nodes on the connection edges. The isometric view of the final form of the fuselage is given in Figure 6.3.15.

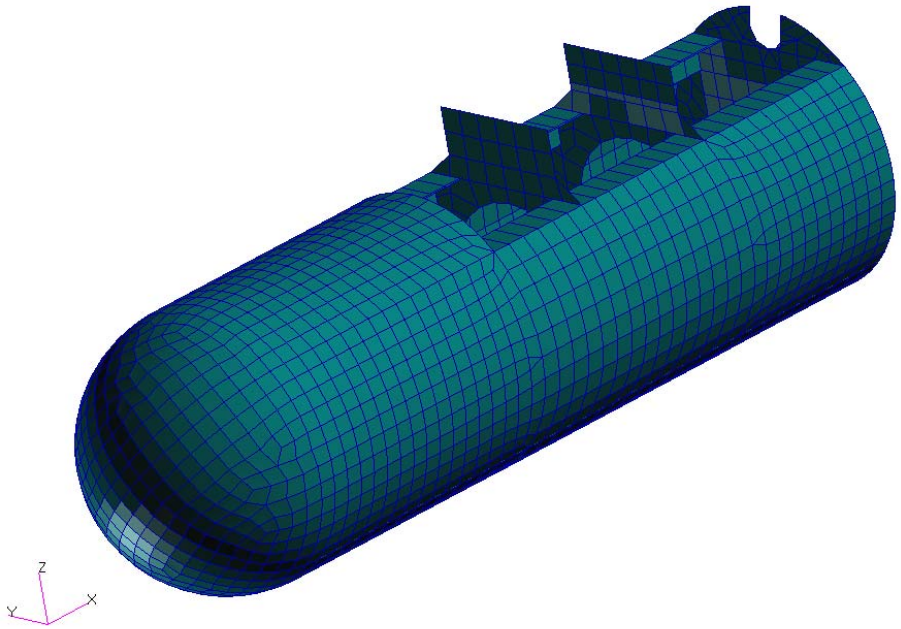

Figure 6.3.15: Structural Model of the Fuselage

6.4 Modeling of the Empennage of the UAV

The empennage of the UAV consists of tail boom, conical segment, horizontal and vertical tails.

The tail boom has the cross-sectional diameter of 45 [mm] and thickness of 0.8 [mm]. The material used for the tail boom is Aluminum 6061-T6. Figure 6.4.1 gives the FEM of the tail boom.

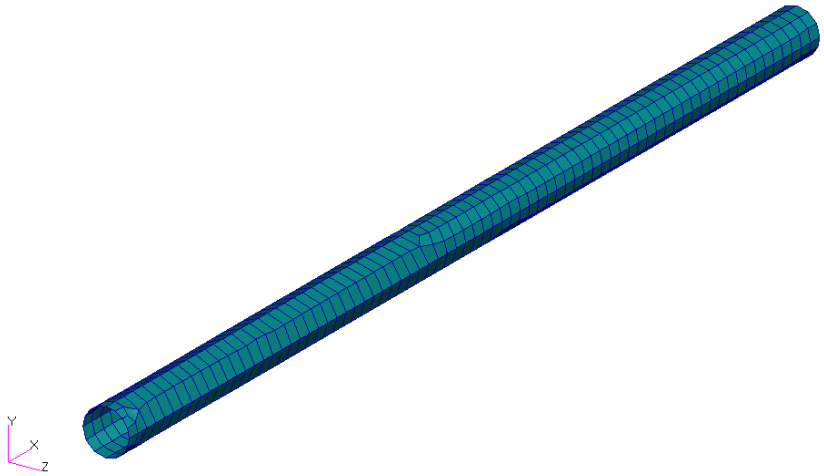

Figure 6.4.1: Structural Model of the Tail Boom

The connection of the cylindrical segment of the fuselage and the tail boom is supported by using a conical segment manufactured from six layers of the composite material with a staking sequence of $[0/90]_6$. This conical segment also creates a smooth aerodynamic surface for the fuselage. The structural model of the conical fuselage segment is presented in Figure 6.4.2.

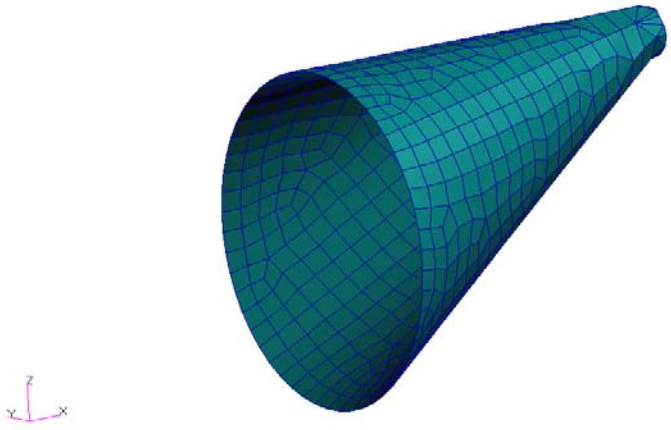

Figure 6.4.2: Structural Model of the Conical Segment

The outer skin of the horizontal stabilizer of the UAV is modeled from six layers of composite material with a staking sequence of $[0/90]_6$. The internal structure of it, on

the other hand, is formed from foam and balsa wood for the modeling of inner volume and the spars respectively. The top view of the horizontal stabilizer is given with its dimensions in Figure 6.4.3 and the structural model where the elevator is not modeled is shown in Figure 6.4.4.

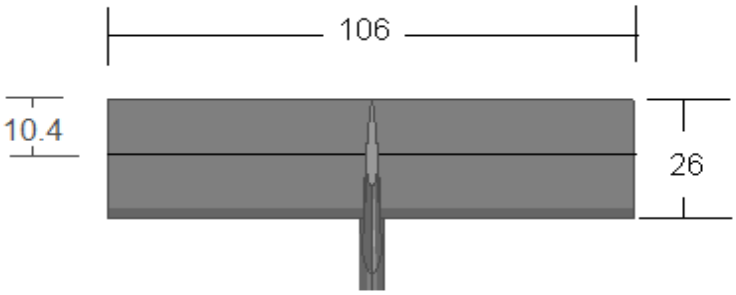

Figure 6.4.3: Dimensions of the Horizontal Stabilizer [cm]

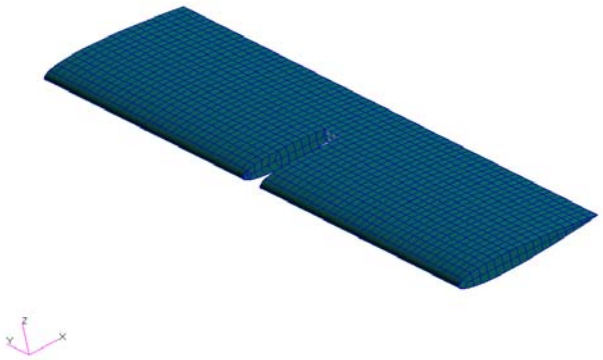

Figure 6.4.4: Structural Model of the Horizontal Stabilizer

The vertical stabilizer of the UAV is modeled by using the same materials used in the horizontal tail for the inner structure but the skin is this time composed of 4 layers composite material having $[0/90]_4$ stacking sequence. Figure 6.4.5 and Figure 6.4.6 show the side view of the vertical stabilizer with its dimensions and the corresponding isometric view of the FEM respectively.

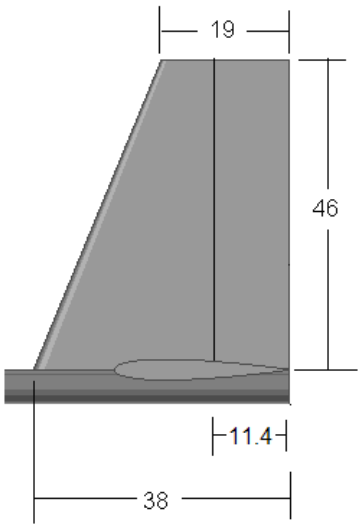

Figure 6.4.5: Dimensions of the Vertical Stabilizer [cm]

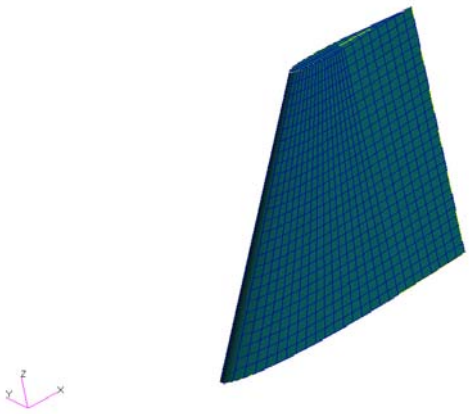

Figure 6.4.6: Structural Model of the Vertical Stabilizer

The assembly of the structural parts is done by making the nodes equivalence at the intersection points of the each component. The structural model of the final assembly of the empennage is presented in Figure 6.4.7.

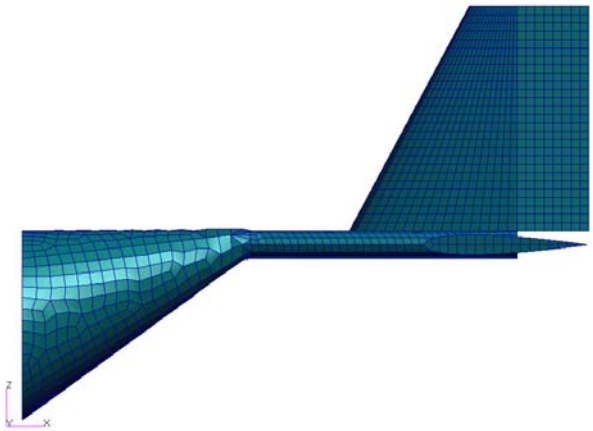

Figure 6.4.7: Structural Model of the Final Assembly of the Empennage

6.5 Modeling of the UAV

After modeling each structural part and the connections, the final structural model of the UAV is formed by connecting the fuselage and empennage to each other which is given in Figure 6.5.1.

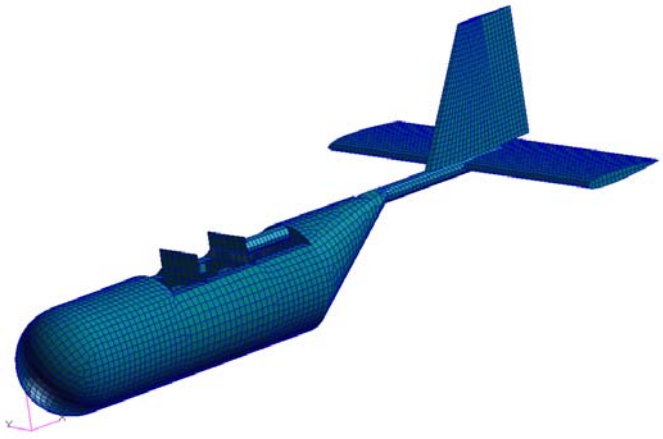

Figure 6.5.1: Structural Model of Connected Fuselage and Empennage

The wing is assembled by using group mirroring option of MSC®/PATRAN. The right wing is mirrored about x-z plane with element properties and boundary conditions to generate the whole wing (i.e. the right and the left wing together). In the FEM, the flanges of the spars are modeled by using beam elements and fasteners are created using the nodes of these elements. The connections are modeled by using Fastener Builder tool of MSC®/PATRAN having diameters of 6 [mm] and made up of Steel AISI 1005. At the spar web and the frame web connections RBE2 elements are used and the wing to fuselage connection is detailed in Figure 6.5.2. The isometric view of the developed structural model of the UAV with its mission adaptive wing is given in Figure 6.5.3 and the mesh properties of the model having 13098 grid points are also provided in Table 6.5.1.

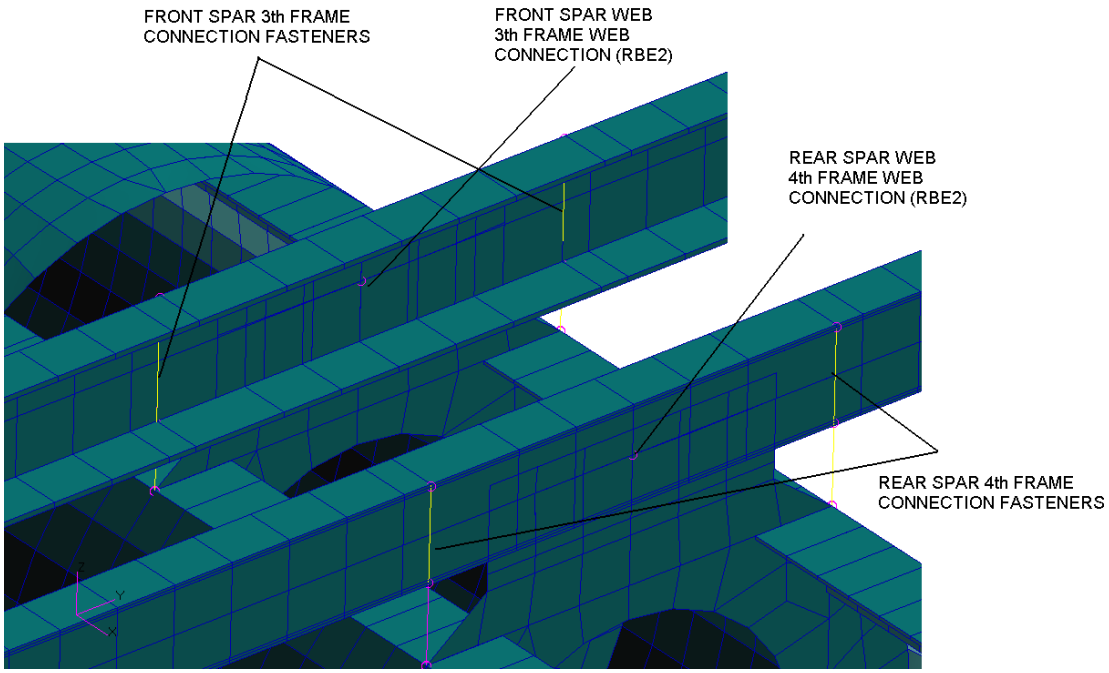

Figure 6.5.2: Structural Model of Wing to Fuselage Connection

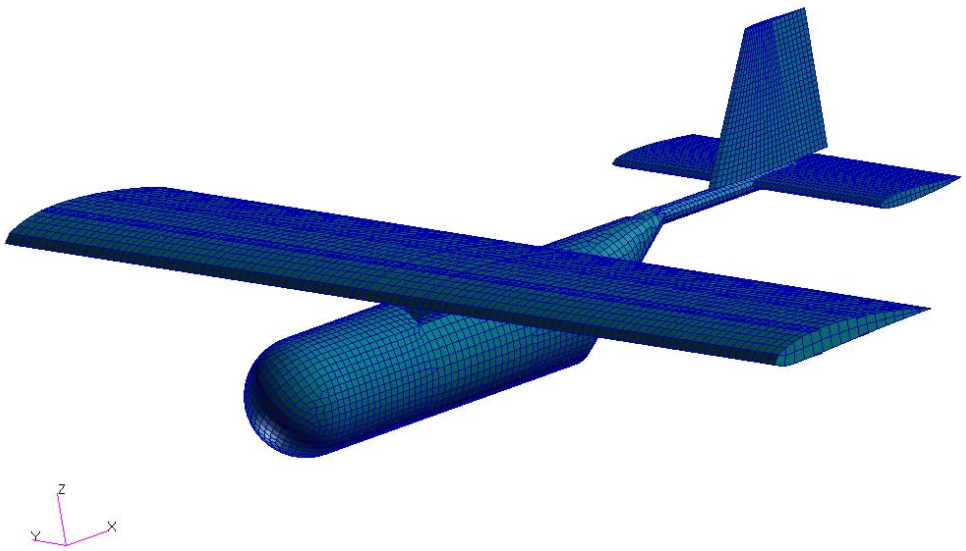

Figure 6.5.3: Structural Model of the UAV with Mission Adaptive Wing

Table 6.5.1: Summary of the Type and the Numbers of Element Used in the FEM of the UAV

Element Type	Element in the Model
BAR Elements	504
BEAM Elements	160
BUSH Elements	12
Shell (QUAD4) Elements	13429
Shell (TRIA3) Elements	127
RBE2 Elements	39
RBE3 Elements	8

6.6 Static Analysis of the UAV

The static analysis of the UAV is performed by simulating as if a vertical 9 [m/s] gust hits on the UAV cruising at sea level at 34 [m/s]. The analysis is performed using "inertia relief constraint" to overcome any inconsistency in the balance of the loads applied to the model. Inertia relief property equally spreads the inertia by a selected node. This node is created in the centre of gravity point of the UAV model

and is connected to the UAV by using RBE2 element between the centre node and selected nodes on the longerons.

The boundary conditions to simulate the analysis condition are developed by creating pressure field on the upper and lower surfaces of wing which is used in the static analysis of the mission adaptive wing since the free stream velocity is taken as the same. In addition to this, dynamic pressure of the air at sea level at 9 [m/s] is applied to the bottom of the UAV including its mission adaptive wing. According to the Equation 6.1 pressure value is calculated as 50 [Pa].

$$P = \frac{1}{2}\rho V^2 \qquad \text{(Eqn. 6.1)}$$

Finally, the total pressure boundary condition on the UAV is generated. There is no pressure field generated on the top of the fuselage of the UAV since it is assumed that 34 [m/s] cruise speed has no significant aerodynamic effect on the fuselage. The pressure boundary condition on the bottom surfaces of the UAV including its mission adaptive wing is presented in Figure 6.6.1 as a contour plot.

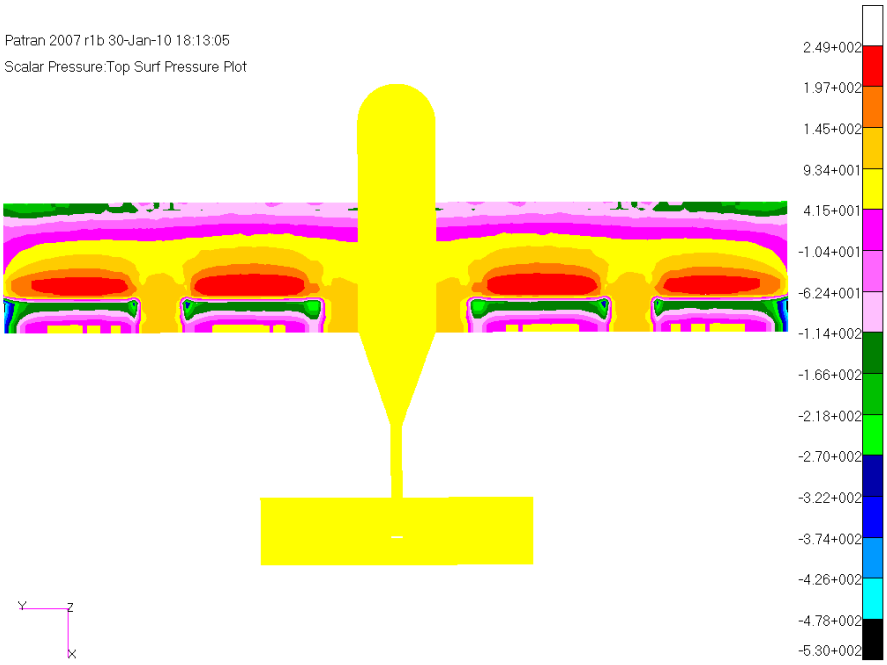

Figure 6.6.1: Pressure Boundary Condition (Bottom View)

Since the analysis is performed using Inertia Relief, the mass properties is encountered to the model in terms of nodal forces calculated as mass times the gravity located at the centre of gravity of the sections of interest.

The engine is fixed on the first frame of the fuselage internal structure using RBE3 type element. The mass of the engine is simulated by applying 1.8g [N] nodal force where the gravitational acceleration (g) is 9.81 [m/s^2]. The payloads on the UAV such as batteries and avionic equipments are also included in the model. The nodal forces of 2g [N] simulates the individual payloads (payload 1, 2, and 3) connected to the equipment raft via RBE3 type elements. The mass of the fuel tank is added to the model as 2.5g [N] nodal force. The total payload including the engine and the fuel and the fuel tank is assumed to be 10.3g [N]. Figure 6.6.2 shows the payloads distribution in the fuselage.

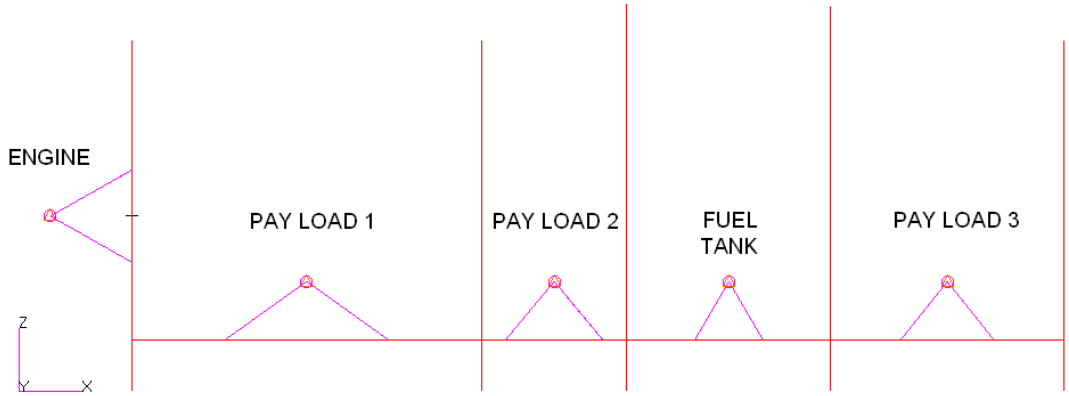

Figure 6.6.2: Payloads Alignment in the Fuselage

The wing weight and the empty fuselage weight are modeled respectively by applying 7g [N] nodal force at the centre of gravity of each wing connected with RBE3 elements to wing spars and 8g [N] nodal force to the centre of gravity of empty fuselage connected with also RBE3 elements to the selected longeron nodes. The total weight of the UAV is found as 32.3g [N].

The gust pressure value is previously calculated as approximately 50 [Pa] acting on 2 [m^2] planform area of the UAV which leads a total force of 100 [N] on the UAV. This sudden force gives the UAV an upward acceleration of approximately 3g according to the Equation 6.2.

$$F = ma \qquad \text{(Eqn. 6.2)}$$

The inertia forces of the given masses become mass times 4g including the gravitational acceleration. For instance 7g [N] weighted wing will result in about 28g which is effectively 280 [N] downward nodal force for each wing in the model.

The first thing before examining the results the constraint forces on the node which is selected for the Inertia relief must be checked. These forces must be very small to rely on the analysis results. The results for the constraint forces on a selected node are very small in both translation (T1, T2, T3) and rotational (R1, R2, R3) directions which are presented in Table 6.6.1.

Table 6.6.1**:** Constraint Forces on Inertia Relief Node [N]

Node ID	**T1**	**T2**	**T3**	**R1**	**R2**	**R2**
20000	-5.96E-15	-2.17E-18	8.07E-14	-2.87E-18	1.92E-14	1.73E-18

The first result is given as the total displacement of the UAV under the pressure loads in Figure 6.6.3. Maximum deflection of 4.52 [mm] occurs on one of the control surfaces. This is expected since the stiffness of the control surfaces is far less than the other structural parts.

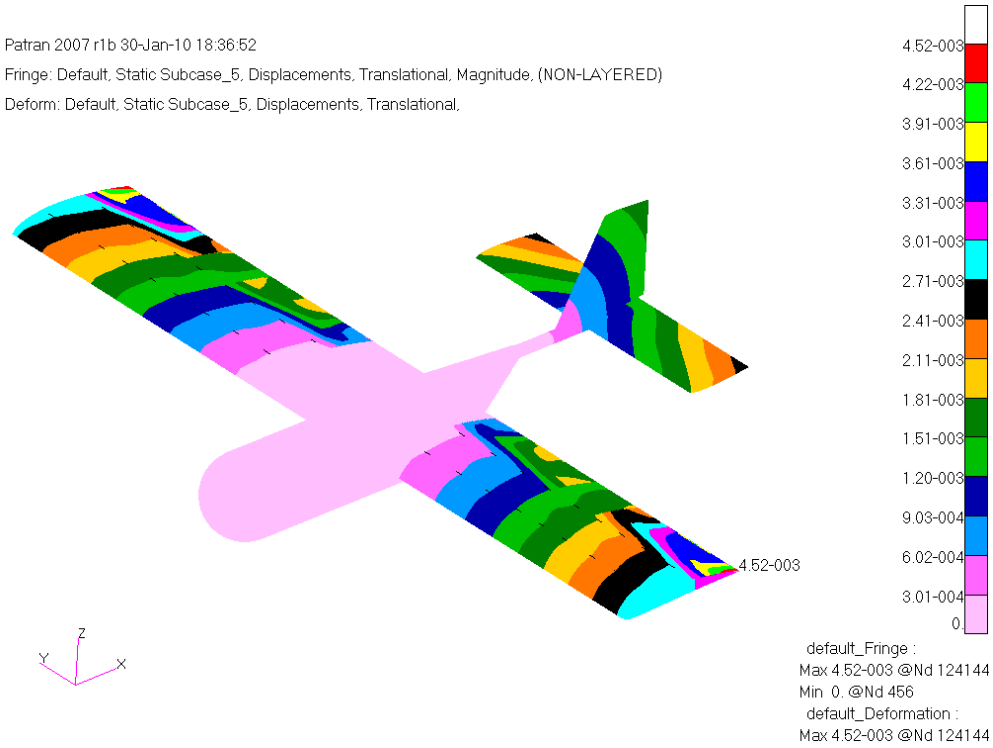

Figure 6.6.3: Displacement Result of the UAV [m]

The deflections of the frames are very small with a maximum deflection of 0.3 [mm] observed on the frame where the engine connected. The equipment raft has a maximum deflection value of 2.2 [mm] under the payload 1. The total displacement result of all frames and equipment raft is presented in Figure 6.6.4.

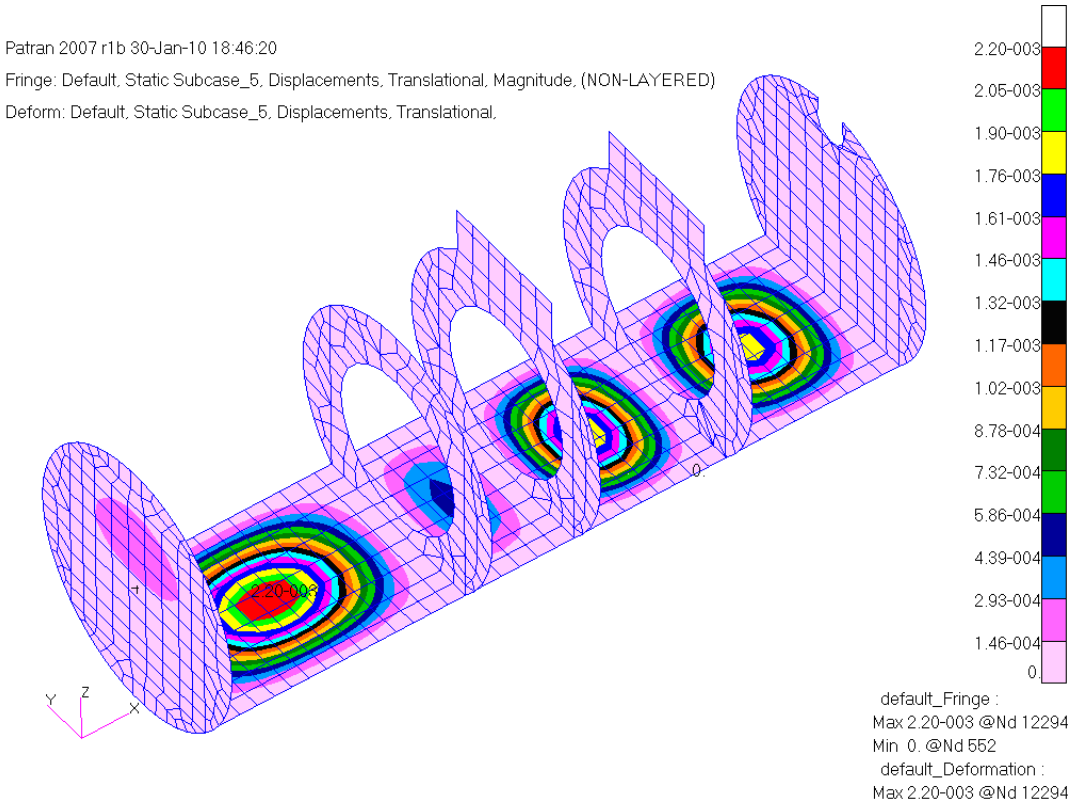

Figure 6.6.4: Displacement Result of the Frames and Equipment Raft [m]

Von Mises stresses are used for the failure analysis and results are presented for the structural parts made of isotropic materials like frames, tail boom and control surfaces (left wing) in Figure 6.6.5 to Figure 6.6.7 respectively.

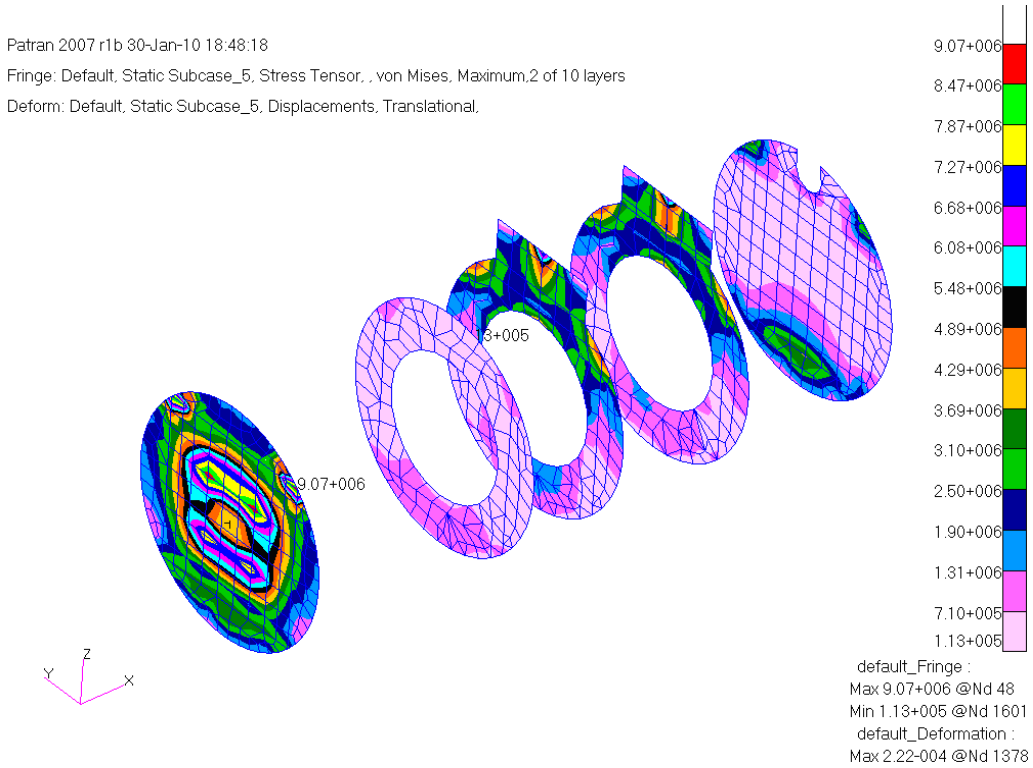

Figure 6.6.5: Stress Distribution on the Frames [Pa]

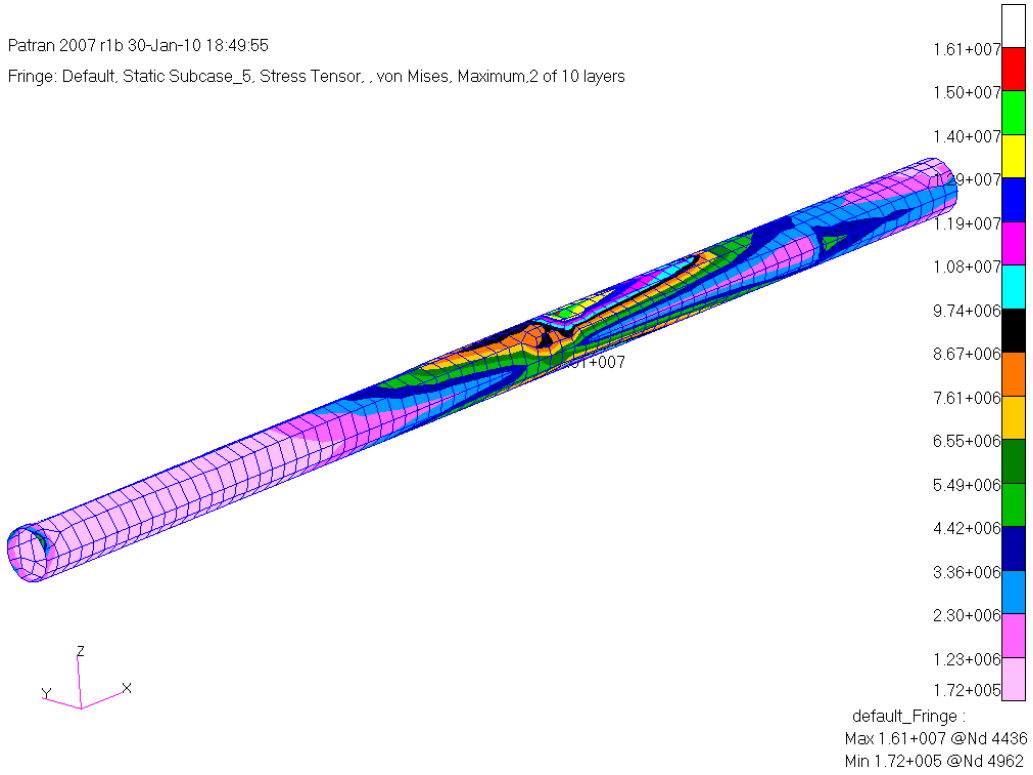

Figure 6.6.6: Stress Distribution on Tail Boom [Pa]

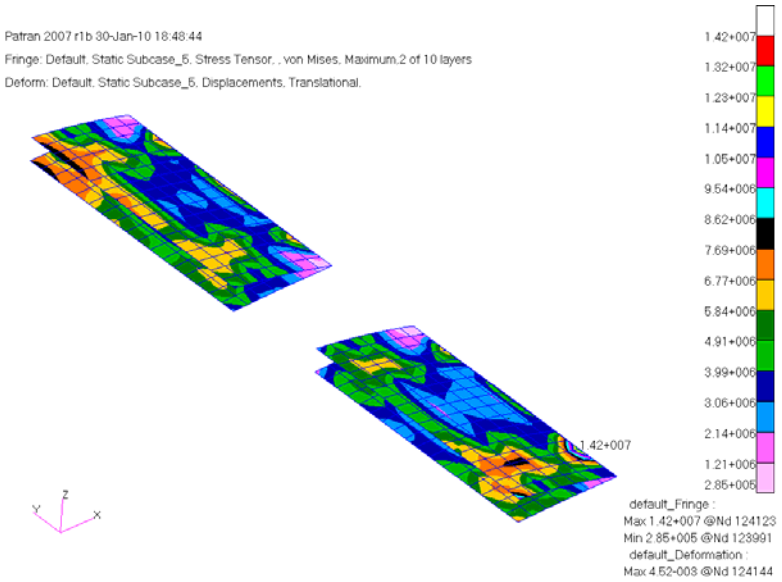

Figure 6.6.7: Stress Distribution Left Wing Control Surfaces [Pa]

By comparing the obtained von Mises stresses with the Yield strength of each structural part made up of isotropic materials, it can be concluded that all structural parts (i.e. frames, tail boom and control surfaces) are safe under the given loading condition. For the longerons which are modeled by using beam elements, the critical stresses are presented in terms of the maximum combined stresses. Distribution of the maximum combined stress distribution on the longerons is given in Figure 6.6.8.

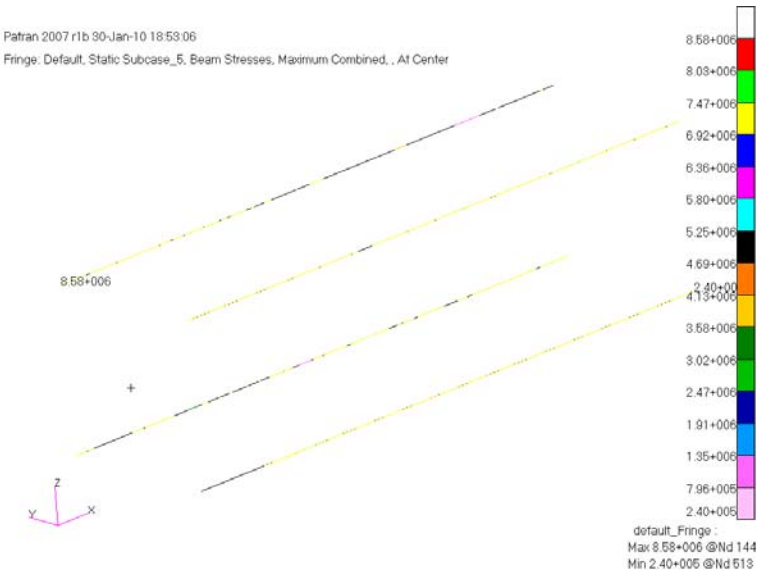

Figure 6.6.8: Stress Distribution on the Longerons [Pa]

As it can be seen in Figure 6.6.8 that maximum combined stresses are well below the Yield strength of the material used in the design of the longerons. Reserve factor (RF) is the ratio of allowable load to the applied load. Table 6.6.2 summarizes the obtained stress values and the reserve factors for the structural parts with their isotropic material properties.

Table 6.6.2: Summary of Stress Results

Structural Part	**Material Name**	**Yield Strength [MPa]**	**Obtained Stress [MPa]**	**RF Value**
Frames	6061-T4	145	9.07	15.99
Tail Boom	6061-T6	276	16.1	17.14
Control Surfaces	2024-T3	385	14.2	27.11
Longerons	7075-T652	503	8.58	58.62

Finally, the constraint forces on the wing to fuselage connection are presented in Figure 6.6.9. Considering the steel fasteners, the tension forces on the fasteners are far below the ultimate values. The forces in the shear plane (i.e. spar web) at the connection are comparably small as well. As a conclusion, connections are safe under the given loading.

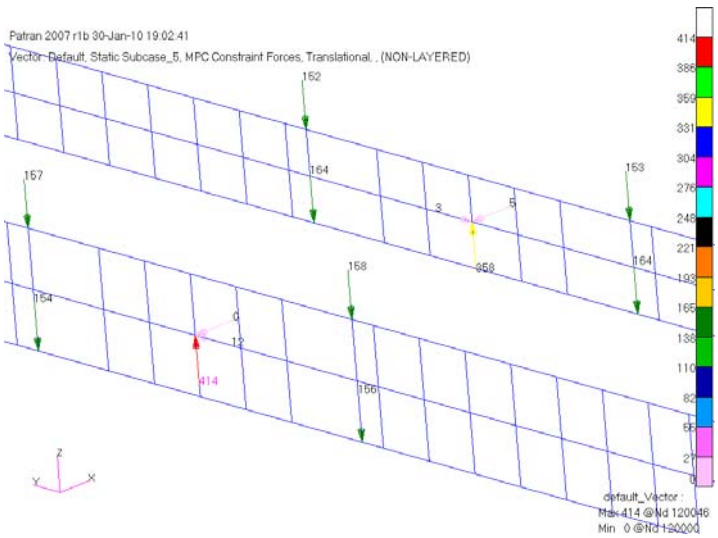

Figure 6.6.9: Constraint Forces on Wing to Fuselage Connection [N]

6.7 Modal Analysis of the UAV

The modal analysis of the UAV is performed with free-free boundary condition and the rigid body modes of the UAV are examined first. Obtained transitional and rotational rigid body modes of the UAV are presented in Figure 6.7.1 to Figure 6.7.6.

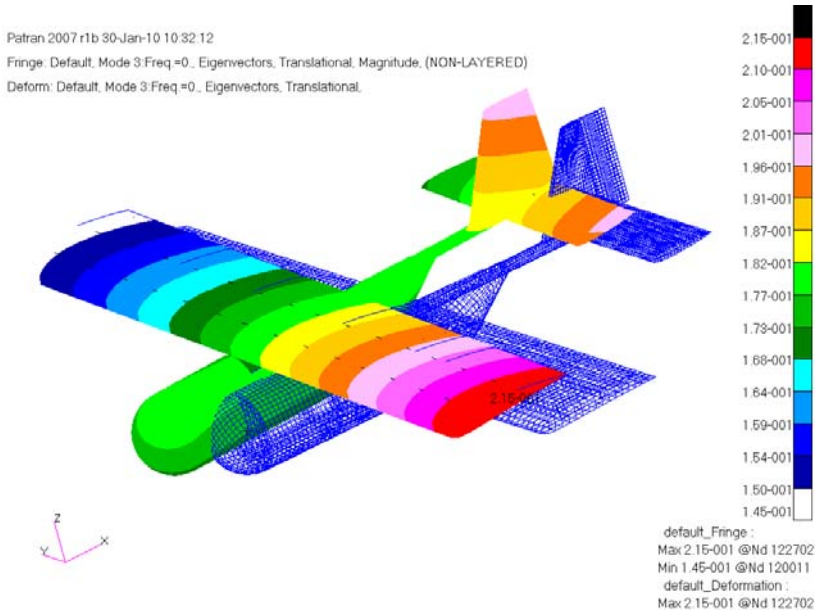

Figure 6.7.1: First Rigid Body Mode of the UAV (Translation in X)

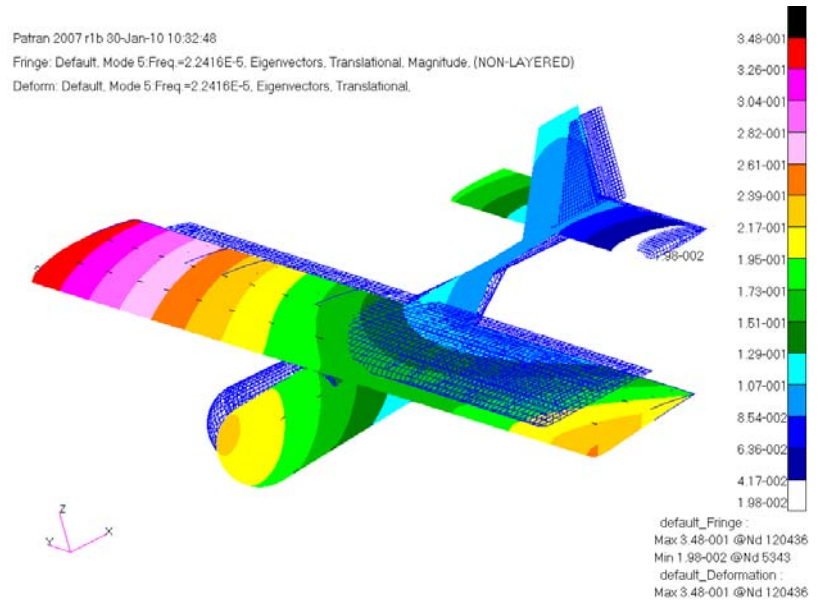

Figure 6.7.2: Second Rigid Body Mode of the UAV (Translation in Y)

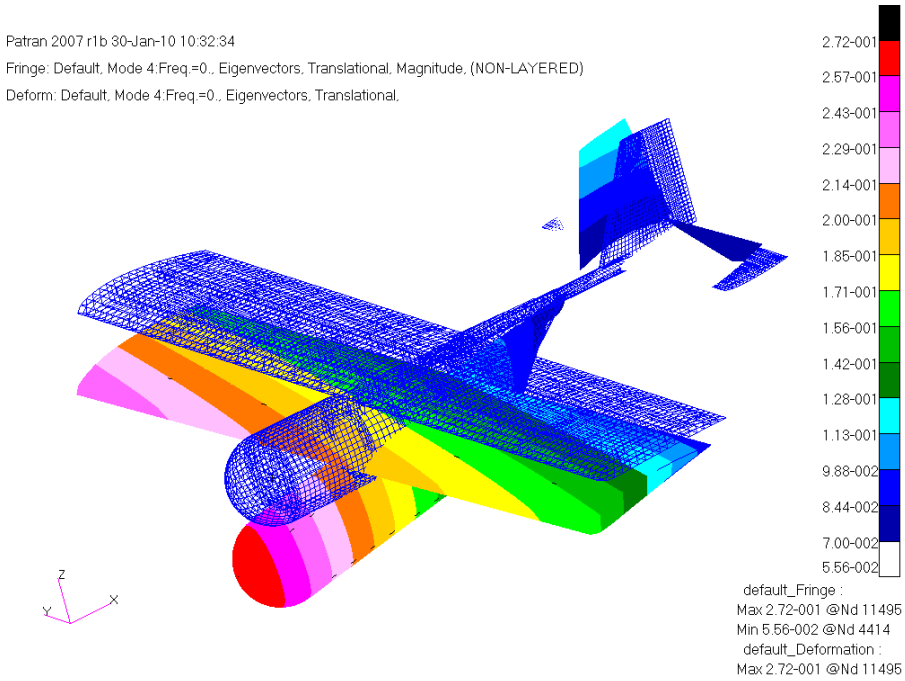

Figure 6.7.3: Third Rigid Body Mode of the UAV (Translation in Z)

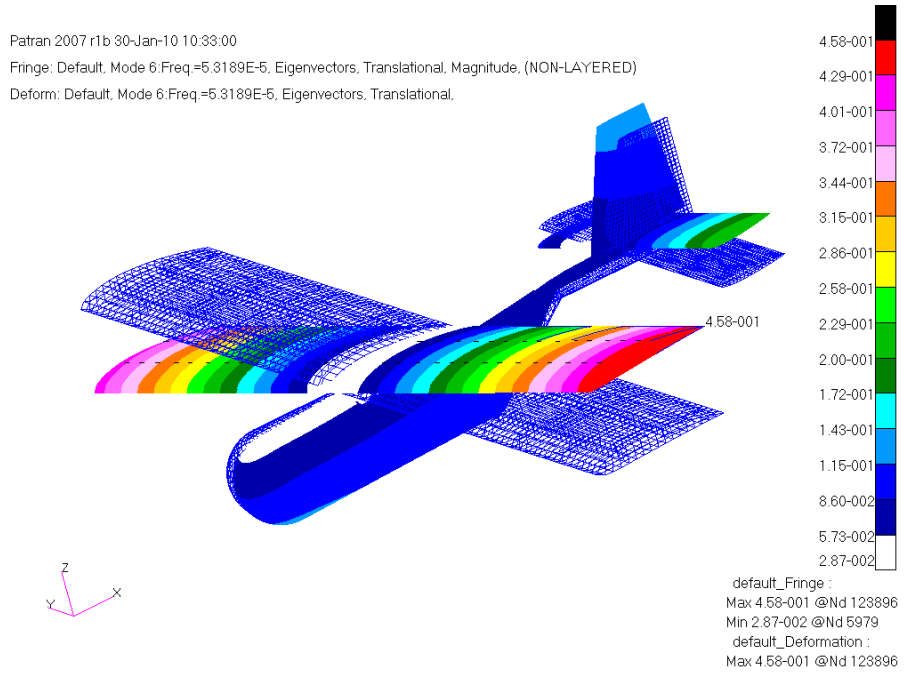

Figure 6.7.4: Fourth rigid body mode of the UAV (Roll)

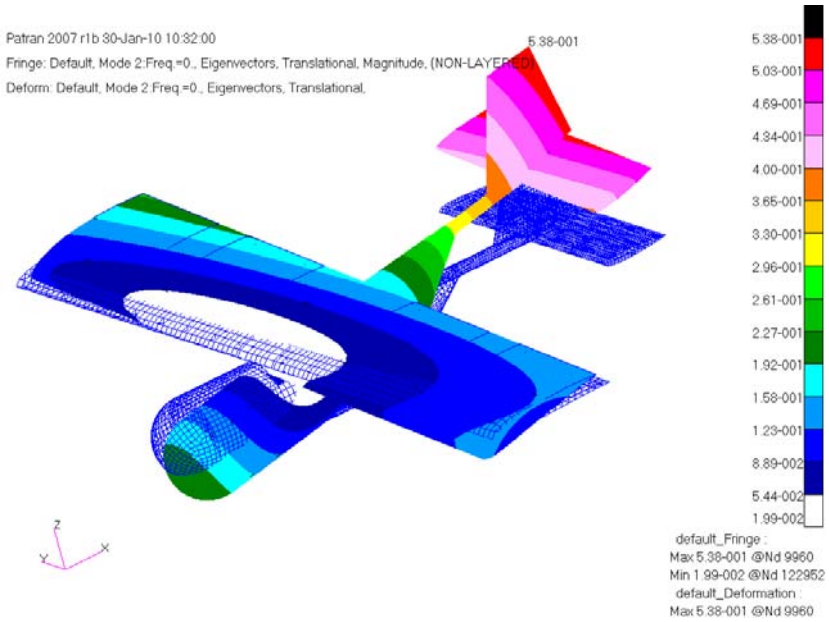

Figure 6.7.5: Fifth Rigid Body Mode of the UAV (Pitch)

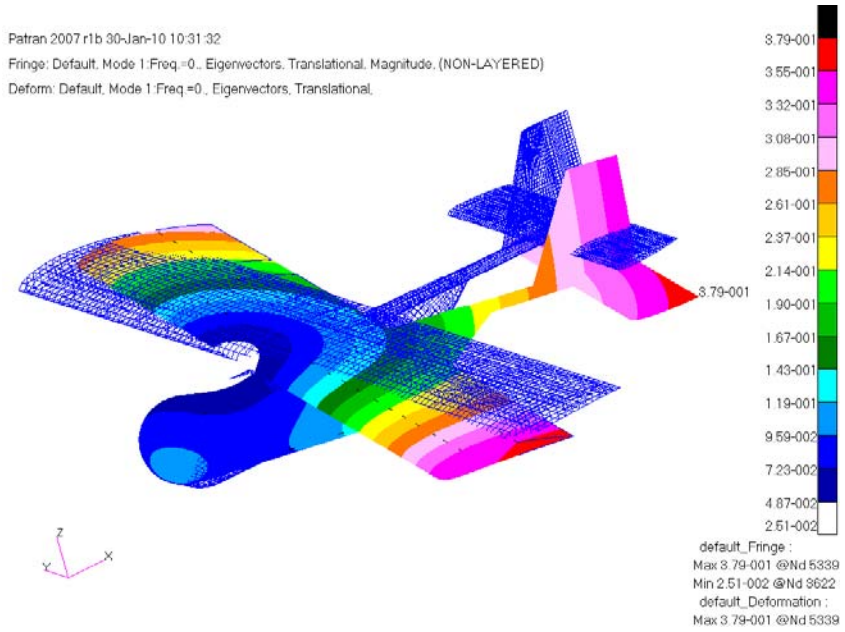

Figure 6.7.6: Sixth Rigid Body Mode of the UAV (Yaw)

In order to compare the first bending frequency of the previously modeled wing, the first out-of-bending mode of the wing on the UAV is also presented in Figure 6.7.7. The previous model without control surfaces (model created in Chapter 5) has first out-of-bending frequency of approximately 14 [Hz]. The difference is due to the change in the boundary conditions together with the mass and the stiffness effects of the added control surfaces.

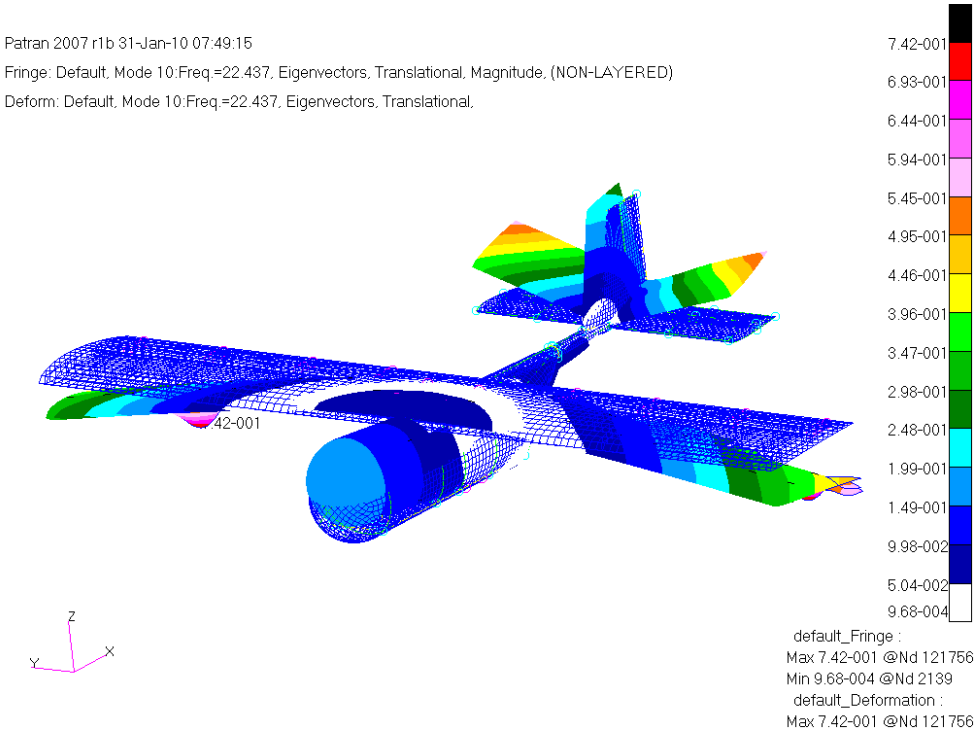

Figure 6.7.7: First Out of Plane Bending Mode of the Wing on the UAV [22.437 Hz]

6.8 Manufacturing of the UAV

The manufacture of the main components forming the fuselage and the empennage are explained and discussed in this section by also providing the final assembly of each component.

The longerons used in the fuselage have L-Section profiles and are manufactured from Aluminum 7075-T652 with a thickness of 1.65 [mm] and flange width of 40 [mm] via metal extrusion method. The longeron flanges will be used as internal connection members for the avionic equipment. All of the frames are manufactured from 2.032 [mm] thick sheet metal Aluminum 6061-T4 by 2D metal cutting method by using Computer Numerical Control (CNC) bench. The manufacturing process of the all laminated composite materials are performed by wet lay-up and the equipment raft can be given as an example of one of those components manufactured with the aforementioned method. The nose of the fuselage is manufactured as modeled. The

exhaust holes and air inlet and outlet for the engine cooling is also generated on the skin of the nose and manufactured accordingly. The manufacturing of the composite skin is performed parallel to the structural model. The fittings enable the connection between the frames and longerons. Longeron fitting connections can be seen in Figure 6.8.1. The frames are connected using two fittings with triple connection for each rivet which are presented in Figure 6.8.2. The manufacture assembly of the internal structure is shown in Figure 6.8.3.

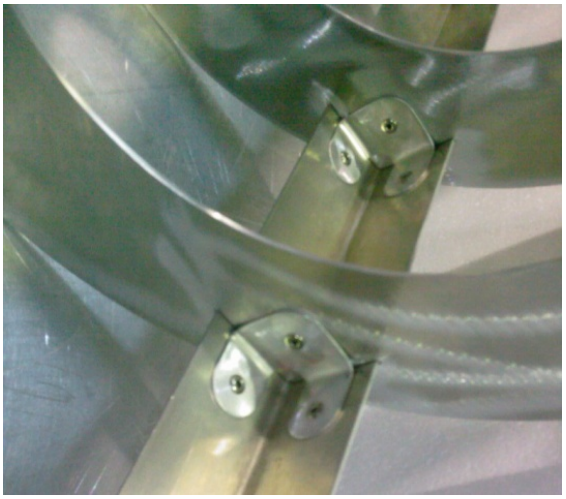

Figure 6.8.1: Fittings, Longeron and Frame Connection View 1

Figure 6.8.2: Fittings, Longeron and Frame View 2

Figure 6.8.3: Manufacture Assembly of the Internal Structure

The assembly of the longerons to the composite skin is done from the corner of the cross-section with the help of rivets. The generated guide holes for the placement of rivets can be seen on the composite skin to longeron connection in Figure 6.8.4.

Figure 6.8.4: Composite Skin Longeron Connection

For the empennage components manufacture and assembly, tail boom has the same property as modeled and is manufactured by metal extrusion. As having a laminated composite material property, the conical segment is produced by using wet lay-up method. Horizontal and vertical tail is also produced as modeled except the control

surfaces of tail (i.e. rudder and elevator). These control surfaces are manufactured and connected to the main parts of tail by hinges. The tail boom is then connected to the vertical and horizontal stabilizers by using polymeric adhesives on the connection surfaces and various pins .The pin holes drilled on the tail boom are presented in Figure 6.8.5 Wooden filler is used in the carved section of the tail boom to fit the surface of the horizontal tail for making the connection surface.

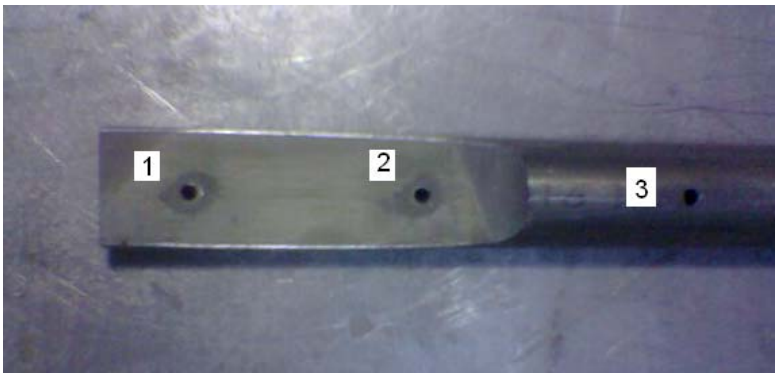

Figure 6.8.5: Connection pin holes on the tail boom

Horizontal tail and two pin holes on the vertical tail and the tail boom are connected through the numbered holes 1 and 2 on the above figure with triple connection by the help of a pin. The vertical tail and the tail boom are connected through the pin hole 3 by double connection. Polymeric adhesives are also used on the connection surfaces. Established assembly of the tail is presented in Figure 6.8.6.

Figure 6.8.6: Connection of Tail

The conical structure and the tail boom are fastened by using polymeric adhesive in the manufacture assembly. Tail boom is connected to the fourth and the fifth frame by using cylindrical fittings. The fitting is used to fix the frames to the tail boom by rivets. The fitting and frame connections for the fourth and the fifth frames are presented in Figure 6.8.7.

Figure 6.8.7: Fitting and Frame Connection for the fourth (left) and the fifth Frame (right)

The conical segment is also attached to the composite skin by using polymeric adhesives. The manufactured connection assembly of conical segment, tail boom, horizontal and vertical tails is presented in Figure 6.8.8.

Figure 6.8.8: Manufacture Connection Assembly of the Tail

In the assembly of the wing to the fuselage, two pins between the spar flanges and the longeron flanges for each spar and one pin between the flange web and spar web for each spar are used and shown in Figure 6.8.9. For demonstration part assembly of the UAV is presented in Figure 6.8.10. The composite skin will be attached after the equipment raft is connected.

Figure 6.8.9: Assembly of Wing to Fuselage Connection

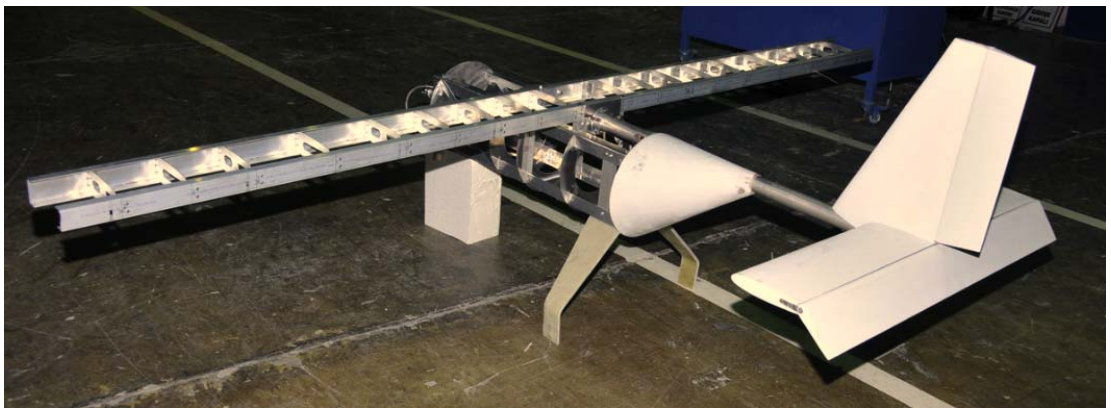

Figure 6.8.10: Assembly of UAV without Fuselage and Wing Skin

6.9 Conclusion

In this chapter, the fuselage and the empennage of the UAV are structurally modeled and connected to the previously modeled wing in order to obtain a complete structural model of the UAV. Static structural and modal analysis of the UAV under the defined given conditions are performed and the results are presented. Having proved the structural integrity of the fuselage and the empennage, the manufacturing of the UAV is finalized with a complete assembly.

CHAPTER 7

DISCUSSION

7.1 Achievements

The first aim of this study is to increase the aerodynamic efficiency of the selected NACA4412 airfoil by changing its camber on a smoothly way. The analyses performed show that the change in aerodynamic coefficients in an effective way can be achieved by performing the introduced camber change methodology. Considering the same L/D values calculated for different cambered airfoils, the study shows that different airfoil cross sections may have the same aerodynamic loading by means of L/D. The selected specific camber changes are applied on the spanwise sections of the generated wing in order to investigate the change in various spanwise pressure distributions. The aeroelastic performance of the generated structural model of the wing is then checked within the flight envelope of the UAV. Additionally, the wing is tested structurally under the pressure load which is generated by a specific sectional camber change. These studies indicate that the modeled wing is safe. Finally, the fuselage and the empennage of the UAV are designed and modeled and the aforementioned mission adaptive wing is then assembled to the UAV. The structural safety of the UAV is check by subjecting it to an extreme loading condition simulated as a gust. The results show that the designed UAV is structurally intact. Having validated the integrity of all parts of the UAV, the manufacturing details are summarized and the assembly of the UAV is finalized.

7.2 Recommendation for the Future Work

One of the most important outcomes of this thesis is that different cambered airfoils may have the same lift to drag ratio. This phenomenon implies that it is possible to sustain aerodynamic loading while changing the structural properties of the wing which can be further analyzed and may lead us to use this concept in the suppression of the aeroelastic instability. Only trailing edge downward deflection cases are considered within the scope of this study but upward deflections of the trailing edge and the deflections of the leading edge can also be further investigated as a future work.

CHAPTER 8

CONCLUSION

In the scope of this thesis, the research aiming to increase the aerodynamic efficiency of the aerial vehicles is examined. Among different alternatives, the methodology of increasing the aerodynamic efficiency is chosen as change in camber. The background of the study is established by performing 2D CFD analyses on differently cambered airfoils generated from the selected NACA4412 airfoil via ANSYS®/FLUENT software.

After examining various cambered airfoils, some of them are selected considering the established camber change methodology and are then used in 3D CFD analyses in order to investigate the aerodynamic effects on the wing surfaces. Having established the aerodynamic efficiency background, the mission adaptive wing is structurally modeled by using finite element modeling and analysis tools (MSC®/PATRAN and MSC®/NASTRAN) following various static, dynamic and aeroelastic analyses performed on the wing. The final part of this study is the structural design and modeling of the fuselage and empennage of the unmanned aerial vehicle by considering flight mechanics approaches. These designed parts and the mission adaptive wing are then assembled to form the complete model of the UAV. Further computational analyses of the unmanned aerial vehicle are performed after assembling of the individual models of fuselage, empennage and the mission adaptive wings. The results obtained from the static and the dynamic analyses performed on this complete UAV model show that the aerial vehicle designed within the scope of this study is both aerodynamically and structurally safe.

REFERENCES

[1] McGowan, A.R. et al., ”Recent Results from NASA’s Morphing Project,” SPIE PaperNo.4698-11,9th International Symposium on Smart Structure and Materials, 2002,SanDiego, California

[2] http://www.pbase.com/ranschols/swift , 1999-2007, PBase.com LLC. , Last visited on March 2008.

[3] Weisshaar,T.,”Aeroelastic Tailoring for Energy Efficient Morphing Aircraft-Finding the Right Stuff,” ICASE Morphing Lecture Series, 2001.

[4] Renken, J. H., “Mission Adaptive Wing Camber Control Systems for Transport Aircraft,” AIAA Paper 85-5006, 1985.

[5] Kudva, J. N., Martin, C. A., Scherer, L. B., Jardine, A. P., McGowan, A. R., Lake, R. C., Sendecky, G. and Sanders, B., “Overview of the DARPA/AFRL/NASA Smart Wing

[6] Marks, P.,”The next 100 years of flight,” NewScientist.com news service, Dec. 2003.

[7] Morphing Airfoil Design for Minimum Aerodynamic Drag and Actuation Energy Including Aerodynamic Work Howoong Namgoong*, William A. Crossley† and Anastasios S. Lyrintzis Purdue University, West Lafayette, Indiana, 47907-2023 AIAA-2006-2041

[8] Monner, H. S., ‘Realization of an Optimized Wing Camber by Using Formvariable Flap Structures’, Aerospace Science and Technology, 5, 445–455, 2001.

[9] Pendelton, E., Bessette, D., Field, P.B., Miller, G.D., Griffin, K.E., 'The Active Aeroelastic Wing (AAW) Flight Research Program', AIAA Paper 98-1972, AIAA/ASME/ASCE/AHS/ASC 39th SDM Conf., April 20-23 Long Beach, USA, 1998.

[10] Raymer, D. P., Aircraft Design: A Conceptual Approach, American Institute of Aeronautics and Astronautics, 2006.

[11] Hilbig H., Wagner H., 'Variable Wing Camber Control for Civil Transport Aircraft', ICAS Procedings, ICAS-84-5.2.1, Toulouse, 107–112, 1984.

[12] Szodruch J., 'The Influence of Camber Variation on the Aerodynamics of Civil Transport Aircraft', AIAA-Paper 85-0353, Reno, November 1985.

[13] Fluent.Inc. 6.3User's guide "http://cdlab2.fluid.tuwien.ac.at/LEHRE/TURB/Fluent.Inc/fluent6.3.26/help/html/ug/main_pre.htm", 2006, Last visited on March 2008

[14] Batina, J. T., 'Unsteady Euler Airfoil Solutions Using Unstructured Dynamic Meshes', AIAA Journal, 28 (8), 1381-1388, 1990.

[15] Spalart, P. R., Allmaras, S. R., 'A One-Equation Turbulence Model for Aerodynamic Flows', AIAA Paper 92-0439, 1992

[16] Bhaskaran, R.,'Fluent Tutorials: Flow over an Airfoil', Cornell University, http://courses.cit.cornell.edu/fluent/airfoil/index.htm, 2002, Last visited on 7 March 2008.

[17] ANSYS®/GAMBIT Version 2.3 Modeling Guide Fluent Inc., March 2006

[18] Seber G., İnsuyu E.T.,Özgen S., Şahin M., Yaman.,"Değişken Kambura Sahip NACA 4412 Kanat Kesitinin 2-Boyutlu Aerodinamik Analizi" UHUK-2008-1035,October 2008

[19] Fluent Inc. 'Tutorials : Modelling Compressible Flow over an Airfoil', 2007

[20] http://www.cfd-online.com/Wiki/Dimensionless_wall_distance_(y_plus), Last visited on March 2008.

[21] Ünlüsoy, L., "Structural Design and Analysis of the Mission Adaptive Wings of an Unmanned Aerial Vehicle", MSc. Thesis, METU, February 2010

[22] MSC®/NASTRAN User's Guide, MSC.Software©, 2001

[23] Sakarya, E.,"Structural Design and Evaluation of an Adaptive Camber Wing", MSc. Thesis, METU, February 2010

[24] MSC®/FlightLoads and Dynamics User's Guide Version 2001 (r1), MSC.Software Corporation, 2001.

[25] Rodden, W. P., Johnson, E. H., User's Guide of MSC®/NASTRAN Aeroelastic Analysis, MSC®/NASTRAN v68, 1994.

[26] Seber G. .,Sakarya E., İnsuyu E.T.,Özgen S., Şahin M., Yaman., "Structural Modeling and Aeroelastic Analysis of Variable Camber Wings" Ankara International Aerospace Paper 2009-1174, August 2009